THE UNIVERSITY OF CHICAGO

EXPERIMENTAL LIMITS ON GRAVITATIONAL WAVES IN THE MHZ FREQUENCY RANGE

A DISSERTATION SUBMITTED TO
THE FACULTY OF THE DIVISION OF THE PHYSICAL SCIENCES
IN CANDIDACY FOR THE DEGREE OF
DOCTOR OF PHILOSOPHY

DEPARTMENT OF PHYSICS

BY
ROBERT K. LANZA, JR.

CHICAGO, ILLINOIS
MARCH 2015

Copyright © 2015 by Robert K. Lanza, Jr.

All Rights Reserved

To Mom and Dad

TABLE OF CONTENTS

LIST OF FIGURES vii

LIST OF TABLES ix

ACKNOWLEDGMENTS x

ABSTRACT xiii

1 INTRODUCTION 1
- 1.1 Gravitational Waves and Radiation 1
- 1.2 MHz Frequency Gravitational Waves 6
  - 1.2.1 Previous Experimental Limits 7

2 POWER RECYCLED MICHELSON INTERFEROMETER 9
- 2.1 Michelson Interferometer 9
- 2.2 Fabry-Pérot Interferometer 11
- 2.3 Power Recycled Michelson Interferometer 13
- 2.4 Surpassing the Shot Noise Sensitivity Limit by Cross-Correlating Two Interferometers 15

3 EXPERIMENTAL SETUP 17
- 3.1 Core Optics 17
- 3.2 Vacuum System 19
- 3.3 Laser Launch 19
  - 3.3.1 Beam Purity 21
  - 3.3.2 Mode Matching to the Cavity 22
  - 3.3.3 Intensity Noise Monitor 24
- 3.4 Transfer Optics 24
- 3.5 Signal Readout Optics 25
- 3.6 End Mirror Transmission Optics 26
- 3.7 Feedback and Control 27
  - 3.7.1 Common Arm (CARM) and Laser Frequency Sensing and Control . . 28
  - 3.7.2 Differential Arm (DARM) Sensing and Control 29
- 3.8 Alignment 31
  - 3.8.1 Injection Alignment 32
  - 3.8.2 Common and Differential Angles 32
- 3.9 Signal Photodetectors 33
- 3.10 Data Acquisition 34
  - 3.10.1 Slow (Control) 34
  - 3.10.2 Fast (Signal) 34

4 NOISE SOURCES AND COUPLINGS . . . 40
4.1 Schnupp Asymmetry . . . 40
4.2 Laser Frequency Noise . . . 41
4.3 Laser Intensity Noise . . . 43
4.4 Sawtooth Noise . . . 43
4.5 Radio Frequency Interference (RFI) . . . 44
4.6 Mechanical and Acoustic Noise . . . 46

5 END-TO-END CALIBRATION . . . 49
5.1 Measurements For the Calibration . . . 52
5.1.1 Measurements in Michelson Mode . . . 52
5.1.1.1 Temporary ASPD for better SNR . . . 54
5.1.1.2 Conditioned DARM Fringe Amplitude . . . 55
5.1.1.3 Calibration Line Magnitude . . . 57
5.1.1.4 DARM loop gain . . . 58
5.1.2 Measurements in Power-Recycled Mode . . . 59
5.1.2.1 Calibration Line Magnitude . . . 60
5.1.2.2 DARM loop gain . . . 60
5.1.3 Transfer of Calibration to Signal Photodetectors . . . 69
5.1.3.1 Agreement with Expected Result . . . 71
5.1.4 Summary of Measurement Results . . . 72
5.2 L Interferometer Calibration . . . 72
5.2.1 Transfer of Calibration Between Measurement Suites . . . 72
5.2.2 Exclusion of 1 Signal Photodetector in L interferometer Data . . . 75
5.3 Comparison with Shot Noise Limited Sensitivity Estimate from Stored Cavity Power . . . 75
5.3.1 Contrast Defect . . . 76

6 ANALYSIS AND RESULTS . . . 79
6.1 Data Acquisition and Methodology . . . 79
6.2 Systematic and Statistical Errors . . . 80
6.3 Test for Correlations . . . 80
6.4 Differential Arm (DARM) Motion Sensitivity . . . 81
6.5 Detector Response to Gravitational Waves . . . 86
6.6 Upper Limits on Gravitational Wave Strain Amplitudes in the 1-11MHz Frequency Range . . . 87

7 CONCLUSIONS AND FUTURE WORK . . . 91

A THE CROSS-SPECTRUM SAMPLING DISTRIBUTION . . . 93
A.1 The General Form . . . 93
A.2 Normalization for Coherence Measurements with Averaged Samples . . . 94
A.3 The Special Case of No Correlation: The Rayleigh Distribution . . . 96
A.4 Verification of the Coherence Sampling Distribution with Simulated Data . . . 98

B STATISTICAL ERRORS IN TRANSFER FUNCTION MEASUREMENTS . . . 104
B.1 General Formulae . . . 104
B.2 Effects of Overlapping and Windowing . . . 104

C SPECIFICATIONS AND PARAMETERS . . . 106

D LASER BEAMS AND INTERFEROMETERS: SUPPLEMENTAL . . . 109
D.1 Gaussian Beams . . . 109
D.2 Pound-Drever-Hall Locking Technique . . . 110
D.3 Finesse, Cavity Pole, & Free Spectral Range . . . 114
D.4 Gouy Phase and Higher Order Modes . . . 116
D.5 Useful Optical Equations . . . 118

E GLOSSARY OF SYMBOLS . . . 119

REFERENCES . . . 120

LIST OF FIGURES

1.1 A sampling of the current state of affairs in the field of gravitational wave physics 2

2.1 Optical configurations for interferometers: Michelson, Fabry-Pérot, and Power-Recycled Michelson . . . 10
2.2 Schematic depiction of electric field propagation in a Michelson interferometer, illustrating the concepts of "dark" and "bright" fringes . . . 12
2.3 Predicted interferometer signals vs. differential arm length difference . . . 15
2.4 Measured interferometer signals vs. differential arm length difference . . . 16

3.1 Core optical layout for a power-recycled Michelson interferometer in the Holometer experiment. . . . 18
3.2 "T" interferometer laser launch. . . . 20
3.3 "L" interferometer laser launch. . . . 21
3.4 Configuration for measurements in Michelson mode. . . . 25
3.5 Control station screens in the tunnel . . . 27
3.6 Low frequency residual power-recycled DARM spectra, calibrated in meters/$\sqrt{\text{Hz}}$ 31
3.7 All 4 signal photodetectors for the 7 data runs in this work . . . 36
3.8 All 4 signal photodetectors, showing 1st Higher Order Mode cavity resonance . . 37
3.9 All 4 signal photodetectors, showing 2nd Higher Order Mode cavity resonance . 38
3.10 All 4 signal photodetectors, showing 3rd Higher Order Mode cavity resonance . 39

4.1 Measured laser frequency noise and modeled CARM loop suppression in power-recycled operation . . . 42
4.2 Measured laser relative intensity noise . . . 44
4.3 Comparison of RFI contamination between the two lasers before and after an extensive campaign to eliminate cross-correlations . . . 46
4.4 Passive seismic isolation for the beasmplitter and power-recycling mirror in the central vacuum service vessel. . . . 47

5.1 Michelson DARM spectrum measured during calibration . . . 55
5.2 Calibration lines measured in the Michelson DARM spectrum . . . 56
5.3 Timeseries output of the tuned conditioning filter stage during a Michelson DARM sweep, used for calibration . . . 57
5.4 Michelson DARM loop transfer function measurement used for the determination of the loop gain $G^{\mathrm{M}}(f_{cal})$ for calibration . . . 59
5.5 Fit to the Michelson DARM loop transfer function data in figure 5.4 for calibration 60
5.6 Michelson TF raw residuals for the fit in figure 5.5 for calibration . . . 61
5.7 Michelson transfer function, error in the fit for calibration . . . 62
5.8 Configuration for measurements in power recycled mode . . . 62
5.9 Superimposed power recycled DARM spectra for the 7 data runs in this work . 63
5.10 Calibration line in the power recycled DARM spectra for the 7 data runs in this work . . . 64

5.11 Power recycled Michelson DARM loop transfer function measurement used for the determination of the loop gain $G^{\mathrm{PR}}(f_{cal})$ for calibration 65
5.12 Fit to the power recycled Michelson DARM loop transfer function data in figure 5.11 to reduce the errors in the measured loop gain magnitude $|G^{\mathrm{PR}}(f_{cal})|$ for calibration 66
5.13 Power recycled Michelson transfer function raw residuals for the fit in figure 5.12 for calibration 67
5.14 Power recycled Michelson error in the transfer function fit for calibration 68
5.15 Relative gain measurement for the two photodetectors $\mathrm{PD_c}$ and $\mathrm{PD_s}$ 69
5.16 Measurement of the 3 calibration lines injected for the L interferometer calibration suite. 73

6.1 The correlation test described in section 6.3, applied to the cross-coherence spectrum between interferometers 82
6.2 Correlation between the signal photodetectors and the loop antenna at 1.35MHz, showing it is electromagnetic in nature 83
6.3 Correlation between the signal photodetectors and the loop antenna at 1.97MHz, showing it is electromagnetic in nature 84
6.4 High frequency residual DARM spectra, with the direct end-to-end calibration results applied to both interferometers, giving units of meters/$\sqrt{\mathrm{Hz}}$ 85
6.5 Normalized gravitational wave transfer function in Equation (6.3). 87
6.6 95% confidence level upper limits on the strain amplitude of gravitational waves incident on the apparatus, in the 1-11MHz frequency range. 90

7.1 The Holometer team pictured over the East Holometer arms 92

A.1 Demonstration of the relatively quick convergence of the Bessel function sum in equation (A.5) 95
A.2 Example of resolving correlated components by averaging samples, using the coherence sampling distribution 99
A.3 Simulated data set #1 used to verify the validity of the coherence sampling distribution in Equation (A.8) 100
A.4 Fits to simulated data set #1 shown in Figure A.3 101
A.5 Simulated data set #2 used to verify the validity of the coherence sampling distribution in Equation (A.8) 102
A.6 Fits to simulated data set #2 shown in Figure A.5 103

D.1 Gaussian laser beam parameters 109

LIST OF TABLES

5.1 Notation for terms in the end-to-end calibration equation 50
5.2 Summary of the calibration measurement scheme. 53
5.3 Summary of end-to-end calibration measurement results for the terms in Equation 5.11 72

C.1 T interferometer operating point parameters during the data runs in this work. . 106
C.2 L interferometer operating point parameters during the data runs in this work. . 106
C.3 Power recycling mirror specifications 107
C.4 Beamsplitter specifications 107
C.5 End mirror specifications 107
C.6 Nominal power-recycling cavity design configuration. 108

D.1 A few useful Fabry-Perot cavity relations. 118

ACKNOWLEDGMENTS

I have been incredibly fortunate to have the opportunity to work with many exceptionally brilliant, talented, and genuinely good-natured people in my graduate career. I have also been lucky to have the loving support of wonderful friends and family. It is impossible to fully and adequately express the depth of my gratitude toward all these people in such a limited space... but I will try.

First and foremost, I want to thank my advisor, Young-Kee Kim, for supporting me at every stage of my graduate career, and for always believing in me. Before I even started at UChicago, she reached out to me and gave me the opportunity to do research with her. She introduced me to the Holometer, setting all of this in motion. She has guided me through my graduate years, and helped me keep the big picture in mind. She has always encouraged me and made my work possible. Thank you!

I want to sincerely thank my co-advisor and mentor on the Holometer, Aaron Chou, for investing his time and energy in me over all these years. Aaron has made important and lasting impressions on the way I think about and approach research and scientific questions. He is always available to flesh out ideas, invent new ones, vet old ones, and even chat about the nuances of fine tequilas - one day my palate will be as sophisticated as yours!

The work in this thesis is by no means just my own; it is the product of hard work by the entire Holometer collaboration: Aaron Chou, Henry Glass, Dick Gustafson, Craig Hogan, Brittany Kamai, Ohkyung Kwon, Lee McCuller, Stephan Meyer, Jonathan Richardson, Chris Stoughton, Ray Tomlin, Jim Volk, Sam Waldman, and Rai Weiss. You have all influenced the way I think and work in so many ways. Years from now I will still be approaching problems in ways that I have learned from all of you. I have been incredibly lucky to work with such a talented group.

Besides the group's invaluable scientific contributions, I'd like to thank the following people individually for their personal contributions and influences on me. Steve Meyer, for

always giving me good advice, for being a signal-processing wizard, for ensuring I had a home at KICP even though I spent most of my time at Fermilab, and for driving for three hours in a snowstorm to transport us between Fermilab and UChicago. Craig Hogan, for his zen master calmness, his relentlessly positive attitude, and his uncanny ability to distill incredibly complicated concepts down to their essence. Rai Weiss, for all I have learned from him in the hours spent working together in the lab, and for the benefit of his vast experience. He is inspiring in his talent, humility, and approachableness. Ray Tomlin, for sharing all of his interesting stories and asking me the right questions. I hope to have a life half as interesting as yours. Dick Gustafson, for being infinitely resourceful and teaching me how to really get things done in an experiment, and for all the interesting conversations. Chris Stoughton, for opening his home to me when Chicago seemed too far away, and for always being there to encourage me. Jim Volk, for letting us set up camp in his trailer for all these years. My fellow graduate students on the Holometer, Lee McCuller, Jonathan Richardson, and Brittany Kamai, for living in the trenches with me. You guys are amazing. I can't believe we made this thing work, and work well!

I want to thank my thesis committee, Young-Kee Kim, Aaron Chou, Craig Hogan, Stephan Meyer, and Zheng-Tian Lu. I sincerely appreciate your hard work to help me reach this point. Lu's philosophy of "diligent thinking" has stuck with me through the years. I also want to thank the entire UChicago Physics Department, especially Nobuko McNeill and Autym Henderson, for helping me navigate graduate school and making the department a friendly place.

My undergraduate physics professors at UC Santa Barbara gave me my first education in physics, encouraged me to go to graduate school, and helped set the direction vector of my academic life. Phil Lubin took me on in his lab at a very early stage in my education. Harry Nelson brought to life the excitement of science in and out of the classroom. He embodied all that one could hope for in an educator, mentor, and all around good human being.

I also want to thank the people in my personal life who have encouraged and supported me. My old roommate and friend, Manual Manard, who stimulated my interest in science at a pivotal point in my life, and was a big part of my decision to go into physics as an undergraduate. Marc Miskin, Jake Ellowitz, Jordan Webster, and Sam Meehan have been amazing friends at UChicago. The humor, creativity, and honest nature of these guys has been inspiring, and I'm thankful to have them as friends.

To my family: Mom, Katy, and Sarah, thank you for putting up with me being so busy these past few years. You have always been there with unwavering and unconditional love and support, and I can never thank you enough. To Dad, even though you are no longer here to see this, you always lovingly encouraged me and supported me in everything I did. To my girlfriend, Jessica, this space is certainly incapable of containing the full extent of my gratitude for all your love and support. I do know, though, that all of this would have been impossible without you.

ABSTRACT

This thesis presents the results of a search for gravitational waves in the 1-11MHz frequency range using dual power-recycled Michelson laser interferometers at Fermi National Accelerator Laboratory. An unprecedented level of sensitivity to gravitational waves in this frequency range has been achieved by cross-correlating the output fluctuations of two identical and co-located 40m long interferometers. This technique produces sensitivities better than two orders of magnitude below the quantum shot-noise limit, within integration times of less than 1 hour. 95% confidence level upper limits are placed on the strain amplitude of MHz frequency gravitational waves at the 10^{-21} $\mathrm{Hz}^{-1/2}$ level, constituting the best direct limits to date at these frequencies. For gravitational wave power distributed over this frequency range, a broadband upper limit of $2.4\times10^{-21}\mathrm{Hz}^{-1/2}$ at 95% confidence level is also obtained.

This thesis covers the detector technology, the commissioning and calibration of the instrument, the statistical data analysis, and the gravitational wave limit results. Particular attention is paid to the end-to-end calibration of the instrument's sensitivity to differential arm length motion, and so to gravitational wave strain. A detailed statistical analysis of the data is presented as well.

CHAPTER 1

INTRODUCTION

Gravitational wave detectors are poised to usher in a new era in cosmology, whereby extremely small deformations in the fabric of spacetime induced by the passage gravitational waves (on the order of 10,000 times smaller than a proton radius!) are detectable with precision laser interferometers. Until now, our picture of the cosmos has been painted by measurements of the electromagnetic field (light). Now, thanks to decades of advances in technology and precision instrumentation, we will begin to open our "eyes" to the gravitational universe, and see the cosmos as it appears in gravitational radiation.

A sampling of the current state of affairs in the field of gravitational wave physics is shown in Figure 1.1. The gravitational wave upper limit results reported in this work add to the picture in Figure 1.1 at the high frequency end, between 1-11MHz, in a previously unexplored region of parameter space. The remaining sections discuss the relevant details for this high frequency search.

1.1 Gravitational Waves and Radiation

Events in space and time are related to each other in terms of the infinitesimal line element ds^2 in general relativity, which describes how these events are separated from each other both in space and time:

$$ds^2 = g_{\mu\nu} dx^\mu dx^\nu \tag{1.1}$$

where $g_{\mu\nu}$ is the metric tensor which encodes information about the geometry and curvature of spacetime. The dynamic interaction between the curvature of spacetime and the matter and energy embedded within it is described by Einstein's field equations, which are a

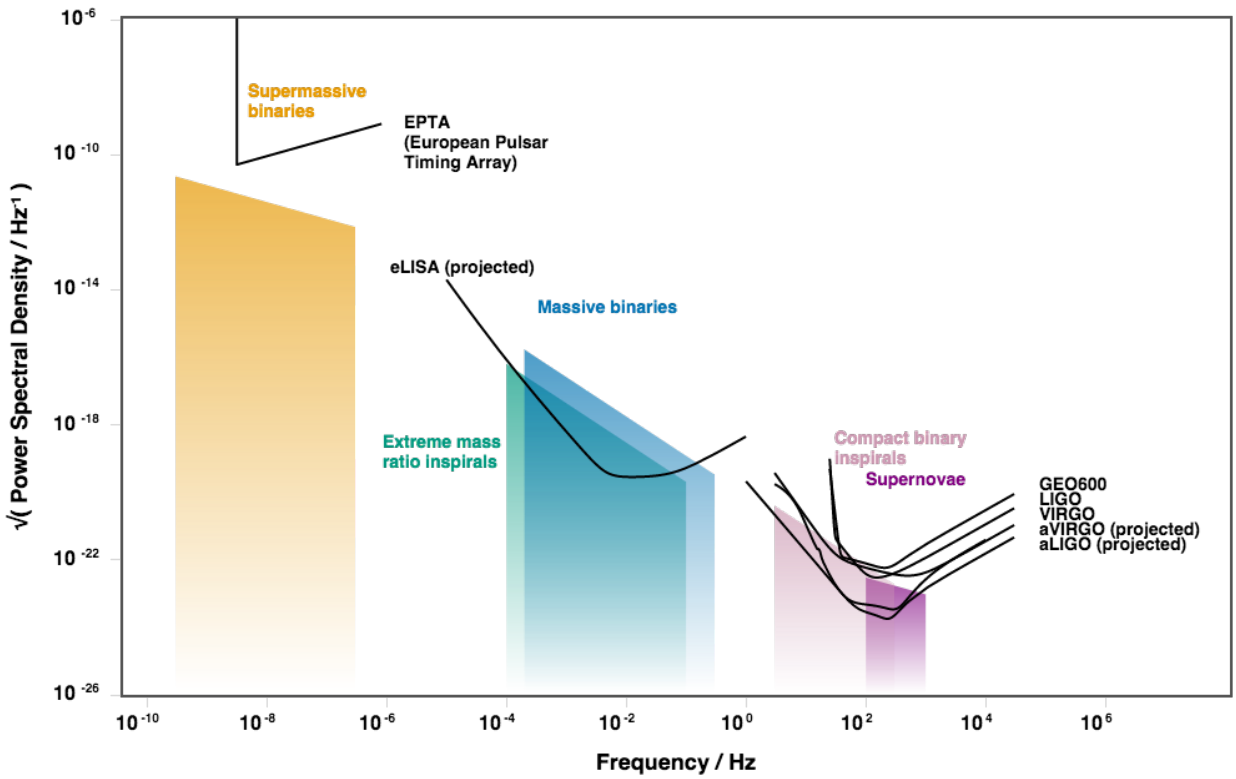

Figure 1.1: A sampling of the current state of affairs in the field of gravitational wave physics. The y-axis units are in amplitude spectral density of strain ($\mathrm{Hz}^{-1/2}$). Sensitivities of various detectors are in black, with projected sensitivities of a few near-term and long-term future experiments included. The detector noise curves all have their resonance spikes removed for clarity. The colored source boxes have a width which gives the range of frequencies sources of that type can have while still being of a detectable amplitude. The Figure was generated with the online utility documented in [18], which contains full details of assumptions and units with calculations.

set of nonlinear equations in terms of $g_{\mu\nu}$. It is this rich and dynamic interplay between geometry and matter/energy which results in interesting modifications to the line element, and consequently to the relationships between events in space and time. General solutions to Einstein's equations can be fairly difficult to find, however it turns out to be very useful to use an approximation of linear perturbations to the metric tensor, in what is called the "weak field limit", where the metric takes the linearized form:

$$g_{\mu\nu} = \eta_{\mu\nu} + h_{\mu\nu} \tag{1.2}$$

where $\eta = diag(-1, 1, 1, 1)$ is the Minkowski (flat) metric, and h describes small deviations from flatness, with $|h_{\mu\nu}| \ll 1$, and the next higher order correction to the weak field approximation being $\mathcal{O}(h^2)$ is negligible.

It turns out [9, 24] that the linear condition on the metric in Equation (1.2) does not uniquely specify the coordinate system in which the perturbation $h_{\mu\nu}$ takes place, and consequently different choices of coordinate system will describe different perturbations $h_{\mu\nu}$– i.e. there is some gauge freedom in choosing a coordinate system which describes $h_{\mu\nu}$.

A very useful and commonly used convention is to choose the "Transverse Traceless" (TT) gauge, which is defined by requiring that $\partial_\mu h^\mu{}_\nu = 0$ and $h_{0\mu} = 0$ (transverse), and $h_\mu{}^\mu = 0$ (traceless). The transverse condition means that metric perturbations only occur in the directions perpendicular to the direction of propagation of the disturbance. Another illuminating and convenient physical interpretation of the TT gauge is that coordinates are defined by freely-falling masses [21]. For these reasons, as we will see, it is fairly intuitive to view gravitational waves in this gauge, because we can clearly see their influence on freely-falling test masses– we will be able to easily interpret deviations in the geodesic trajectories of inertial masses due to h.

In the TT gauge, the weak field limit of Einstein's equations yields a wave equation in h [17, 21]:

$$\left(\nabla^2 - \frac{1}{c^2}\frac{\partial^2}{\partial t^2}\right) h_{\mu\nu} = 0 \tag{1.3}$$

and a plane wave solution for a wave traveling in the z-direction is given by:

$$h_{\mu\nu} = \begin{pmatrix} 0 & 0 & 0 & 0 \\ 0 & h_+ & h_\times & 0 \\ 0 & h_\times & -h_+ & 0 \\ 0 & 0 & 0 & 0 \end{pmatrix} e^{i(kz-\omega t)} \tag{1.4}$$

where the notation h_+ and $h_\times$ is in anticipation of further decomposing the plane wave expression for h into a basis of orthogonal $+$ and $\times$ polarizations:

$$e^+_{\mu\nu} = \begin{pmatrix} 0 & 0 & 0 & 0 \\ 0 & 1 & 0 & 0 \\ 0 & 0 & -1 & 0 \\ 0 & 0 & 0 & 0 \end{pmatrix} \quad , \quad e^\times_{\mu\nu} = \begin{pmatrix} 0 & 0 & 0 & 0 \\ 0 & 0 & 1 & 0 \\ 0 & 1 & 0 & 0 \\ 0 & 0 & 0 & 0 \end{pmatrix} \tag{1.5}$$

with h_+ and $h_\times$ being the amplitude of the waves in either polarization, so that a general plane gravitational wave has the form

$$h_{\mu\nu} = e^+_{\mu\nu} h_+ + e^\times_{\mu\nu} h_\times \tag{1.6}$$

Decomposition of h for a plane wave into a basis of orthogonal $+$ and $\times$ polarizations shows how gravitational waves produce strain in the plane perpendicular to the propagation direction (stretching in one direction, while simultaneously squeezing in the orthogonal direction), which was guaranteed at the outset by the transversality condition of the gauge choice.

As a gravitational wave propagates through a region of space, it modifies the answer we get when we measure the distance between two separated objects, and it does so in a

time dependent way. This is because the passing gravitational wave is in fact stretching and squeezing the underlying fabric of spacetime in which the objects are embedded. As an explicit example, consider the measurement of the distance between two freely-falling (inertial) mirrors separated along the $\hat{x}$-axis, in the presence of a gravitational wave with + polarization which is traveling in the $\hat{z}$-direction. We can measure the distance between the two mirrors by sending a laser beam from one mirror down to the other mirror and back, and then recording the round trip travel time of the light. Let L be the nominal distance between the two mirrors in the absence of a gravitational wave. Using equations (1.1) and (1.2), and the fact that light travels along null geodesics (meaning $ds^2 = 0$), we can solve for the round trip distance traveled by the light between the two mirrors. The line element in this case is:

$$\begin{aligned} ds^2 = 0 &= \left(\eta_{\mu\nu} + h_{\mu\nu}\right) dx^\mu dx^\nu \\ &= -c^2 dt^2 + \left(1 + h_+\right) dx^2 \end{aligned}$$

and integrating along the light's trajectory gives the round trip distance traveled by the light between the two mirrors in terms of the elapsed travel time τ_{rt}:

$$\begin{aligned} L_{rt} \equiv c \int_0^{\tau_{rt}} dt &= 2 \int_0^L \sqrt{1 + h_+} dx \\ &\approx 2L \left(1 + \frac{h_+}{2}\right) \end{aligned} \tag{1.7}$$

where the last line is true when $h_+ \ll 1$. Equation (1.7) shows that the presence of a gravitational wave has *increased* the distance between the two mirrors by an amount $dL \approx Lh_+/2$. If we now do the same measurement, but with the mirrors oriented along the $\hat{y}$-axis

instead, we get a different answer: $L_{rt} = 2L\left(1 - \frac{h_+}{2}\right)$, in which case the distance between the mirrors has been *decreased* by an amount $dL \approx Lh_+/2$. Taking the difference in path lengths between the two directions, and noting that the distance between the mirrors is $L_{rt}/2$, then gives the difference in lengths along the $\hat{x}$- and $\hat{y}$-directions induced by the passing gravitational wave:

$$L_x - L_y = h_+ L \tag{1.8}$$

As will be discussed in Chapter 2, a Michelson laser interferometer is capable of directly measuring the arm length difference $L_x - L_y$ in equation (1.8) by comparing the phases of the laser beams returning from each of the two far mirrors. In this way, a Michelson interferometer can directly measure the amplitude h of a gravitational wave.

1.2 MHz Frequency Gravitational Waves

The thought experiment above revealed that measurements of the gravitational wave strain amplitude h depend on knowing the nominal separation distance between test masses L, or at least being able to keep L relatively constant so that the perturbation h dominates the motions of the test masses. As will become clear in the later technical chapters which treat the experimental apparatus in this work, the largest and most difficult to deal with noise sources which cause fluctuations in L occur at low frequencies, below $\sim$ 1MHz, with rapidly increasing amplitude toward lower frequencies. It is the lower frequency regime ($\sim$ 100Hz) where large-scale (L = 4km) gravitational wave detectors such as LIGO [23] and VIRGO [2] operate, at the expense (technologically and monetarily) of having to tame the enormous low frequency noise sources.

However at higher frequencies, above $\sim$ 1MHz, the fundamental limitation to mea-

surement precision in a Michelson interferometer is more commonly from the quantum-mechanical nature of the laser light itself (photon shot noise), and it is (relatively speaking) fairly easy and inexpensive to achieve sensitivities at this quantum limit[1]. As will become clear later, a shorter length interferometer ends up having better sensitivity at higher frequencies than a longer interferometer (c.f. section 6.5 for the exact relationship). For this reason, we have chosen a length of 40m, which is many orders of magnitude more sensitive to MHz frequency gravitational waves than the larger 4km interferometers.

This thesis discusses a search for gravitational waves in the $1 - 11$MHz frequency range, and the following sections discuss theoretical predictions for possible sources of high frequency gravitational radiation, as well as existing experimental limits on the strain amplitude of such waves.

1.2.1 Previous Experimental Limits

The experiment in [7] used a technology based on two coupled superconducting microwave cavities of length l, in which harmonically driven cavity length changes induce the exchange of energy between two of the resonant microwave cavity modes (an idea originally proposed in [20] for the detection of gravitational waves). The mechanism is particularly sensitive to length changes at frequencies where the applied length modulation equals the difference in frequency between the two cavity modes. They report an achieved sensitivity to fractional length changes of $dl/l = 3.3 \times 10^{-20}\mathrm{Hz}^{-1/2}$ at 1MHz.

The results of a search for a stochastic gravitational wave background (SGWB) in a 2kHz wide bandwidth centered around 100MHz are reported in [3], with a gravitational wave strain sensitivity of $10^{-16}\mathrm{Hz}^{-1/2}$ in each of two 75-cm baseline synchronous recycling interferometers. They then cross-correlated the two interferometer outputs for 1000 seconds to place an upper limit on the energy density spectrum of the SGWB in that band of

1. Section 2.4 describes how in this work we have actually surpassed this quantum limit by more than a factor of $\times 100$.

$h_{100}^2 \Omega_{gw} < 6 \times 10^{25}$ (where the Hubble constant is $H_0 \equiv h_{100} \times 100$km/s/Mpc).

There are also some recently proposed experiments for detecting MHz frequency gravitational waves worth mentioning. A proposed experiment by [13] has not yet actually set a limit, but they have made extrapolated estimates of the strain sensitivities they believe can be reached with the technology they are developing. They propose to cryogenically cool phonon trapping acoustic cavities (Bulk Acoustic Wave resonators), with spectral strain sensitivities as low as $10^{-22}\mathrm{Hz}^{-1/2}$ per resonant mode possible, at discrete narrow band frequencies distributed between a few MHz to around 1GHz or so.

There is also an interesting proposal to use optically trapped and levitated microspheres in a tabletop setup to detect gravitational waves between 50-300kHz by [4]. They predict that sensitivities exceeding laser-based gravitational wave observatories can be achieved in this frequency range, however, it is unclear if the technology can be applied at even higher frequencies.

CHAPTER 2

POWER RECYCLED MICHELSON INTERFEROMETER

The end of section 1.1 began the motivation for why a Michelson laser interferometer is particularly adept at detecting the small variations in strain induced by a passing gravitational wave. This chapter gives an overview of the type of Michelson laser interferometer used in this work, and what level of sensitivity can be achieved. Section 2.1 describes the essential characteristics of a Michelson interferometer and how it measures arm length differences as in Equation 1.8. Sections 2.2 and 2.3 describe how the sensitivity of an ordinary Michelson interferometer can be vastly increased by using a technique called "power recycling." And section 2.4 discusses how two identical power-recycled Michelson interferometers can be used to reach a strain sensitivity that is more than $\times 100$ below the quantum shot noise limit in an individual interferometer.

Also note that much of the supporting theoretical machinery for laser beams and interferometers is included in the appendix section D. This Chapter is a high level overview of the concepts and motivations relevant for the optical configuration used in this experiment.

2.1 Michelson Interferometer

We can start by describing the laser beam itself[1]. It has an electric field with amplitude E, which oscillates at a central frequency ω: $Ee^{i\omega t}$. The laser is then incident on the Michelson interferometer. The optical configuration of a Michelson interferometer is shown in figure (2.1a). It consists of a beam splitter which splits the light equally into two components (each component having half the original electric field amplitude): one component which is reflected, and another component which is transmitted. The two beams travel for a length L down perpendicular paths where they are reflected back to the beamsplitter by mirrors.

1. More complete details are in section D.

The beams are then recombined at the beamsplitter, where their electric fields are summed together, and the total phase accumulated by each beam is proportional to the total path length traveled. The power of the recombined beam which exits the interferometer out the "antisymmetric port" (AS-port) is given by:

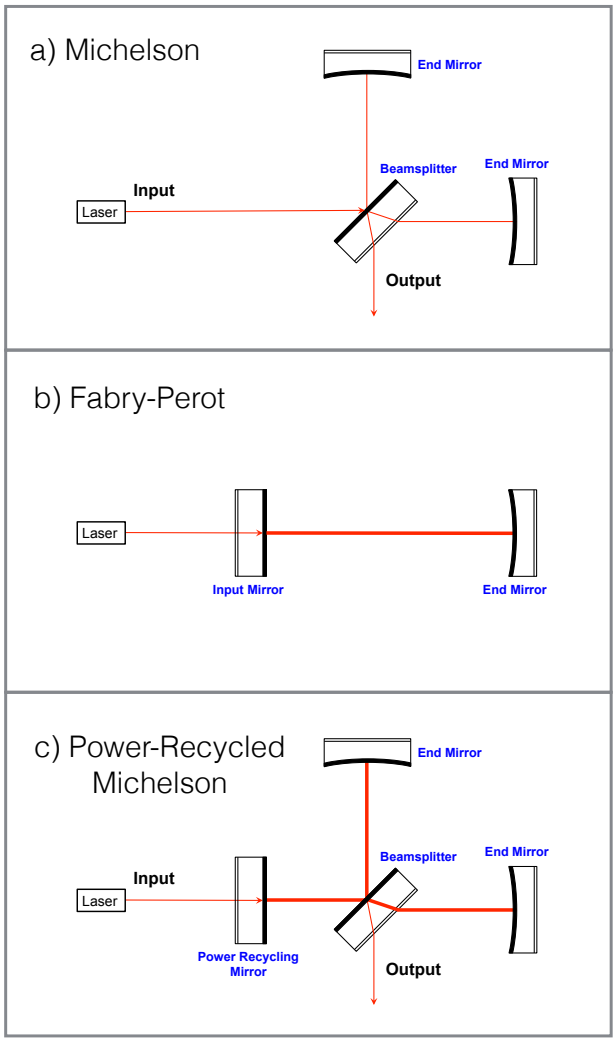

Figure 2.1: Optical configurations for interferometers: a) Michelson, b) Fabry-Pérot, c) Power-Recycled Michelson.

$$P_{out} = E_{out}E^*_{out} = P_{in}\sin^2(k(L_x - L_y)) \tag{2.1}$$

where $k = 2\pi/\lambda$, λ the laser wavelength, and L_x and L_y are the distances between the beamsplitter and the two end mirrors along the $\hat{x}-$ and $\hat{y}-$directions, respectively. Equation 2.1 shows that the power exiting the interferometer's antisymmetric port is given in terms of the net arm length difference $L_x - L_y$, which Equation (1.8) showed was precisely the quantity that is modulated by the presence of a gravitational wave. Figure 2.2 schematically depicts the propagation of the electric fields in a Michelson interferometer, and how they combine to give constructive and/or destructive interference at the output, depending on the difference in arm lengths. The "dark fringe" corresponds to the minimum power exiting the Michelson interferometer according to Equation (2.1), and the "bright fringe" to the maximum.

The top right trace in Figure 2.3 shows the predicted power output of a Michelson interferometer vs. arm length difference, normalized to 1 watt of input power.

2.2 Fabry-Pérot Interferometer

The Fabry-Pérot interferometer is a resonant optical cavity formed by two partially transparent mirrors, in which laser light leaking through the input mirror is reflected back and forth between the mirrors, as shown in figure (2.1b). Resonance is achieved when an integer number of wavelengths of the light fits within a round trip of the light in the cavity:

$$n\lambda = 2L \tag{2.2}$$

When this condition is satisfied, the optical field constructively interferes with itself as it reflects back and forth between the mirrors. In this way, a large amount of optical power can be stored inside the cavity, with only a relatively small amount of incident power.

Table D.1 in the appendix gives some useful relations for the electric fields in various parts

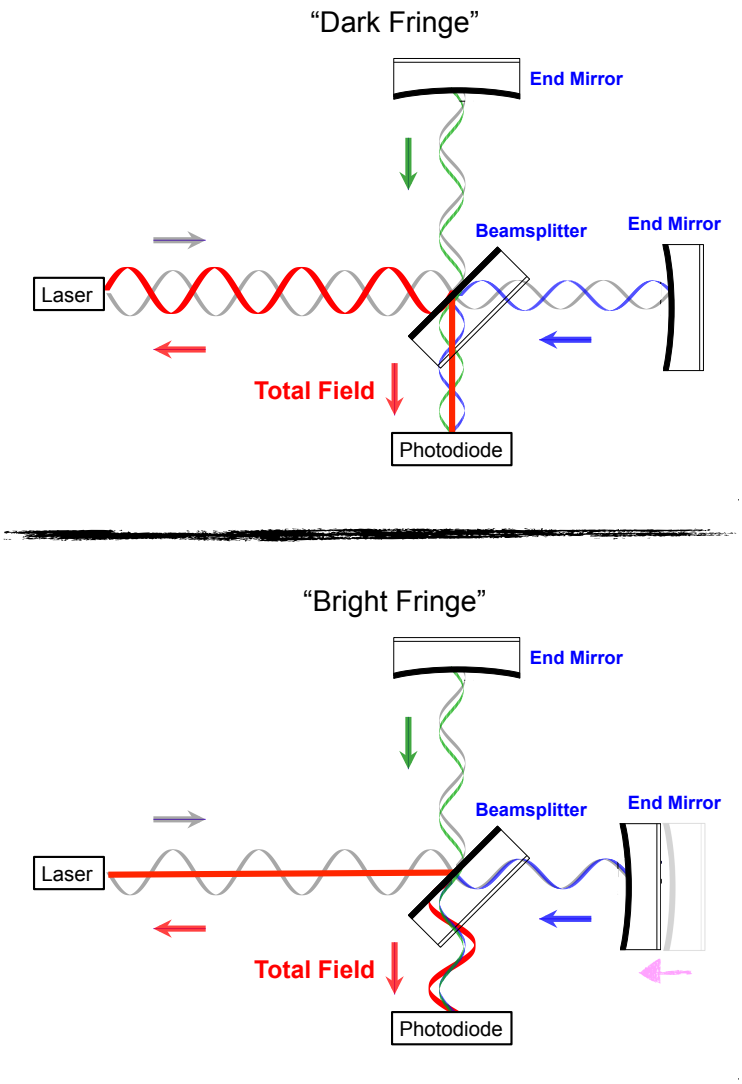

Figure 2.2: Schematic depiction of electric field propagation in a Michelson interferometer, illustrating the concepts of "dark" and "bright" fringes, due to destructive and constructive interference of the beams returning to the beamsplitter, respectively. The Bright fringe corresponds to the maximum power exiting the Michelson interferometer according to Equation (2.1), and the Dark fringe to the minimum. The net sum of all field components is shown in red.

of a Fabry-Pérot interferometer. From them, one can determine the power buildup, reflected power, and transmitted power, in terms of the optical parameters. Each optic is modeled to have *amplitude* reflectivity and transmission coefficients r and t, respectively, which describe how the *electric field* is distributed between reflected and transmitted components after

interacting with an optic[2].

One important quantity for the cavity is the "cavity gain" G_{cav} which is the ratio of circulating power to incident power on resonance:

$$G_{\text{cav}} \equiv \frac{P_{circ}}{P_{in}} = \left(\frac{t_1}{1 - r_1 r_2}\right)^2 \tag{2.3}$$

As will be discussed in later chapters, typical cavity gains achieved in this experiment are on the order ~ 3000, providing very large circulating powers. Section D.3 in the appendix gives an overview of a few other important quantities for a Fabry-Pérot resonator cavity, such as the Finesse, Cavity Pole, and Free Spectral Range.

The next section discusses how the Fabry-Pérot cavity can be combined with the Michelson configuration to drastically improve the sensitivity of a Michelson interferometer to differential arm length motion.

2.3 Power Recycled Michelson Interferometer

The shot-noise limited sensitivity of a single Michelson interferometer to differential arm length motion $\Delta X_{\text{DARM}} \equiv \text{L}_\text{x} - \text{L}_\text{y}$, is given as a function of frequency in amplitude spectral density with units meters/$\sqrt{\text{Hz}}$ by:

$$\Delta X_{\text{DARM, shot}} = \frac{1}{k}\sqrt{\frac{E_\gamma}{P_{\text{BS}}}} = \sqrt{\frac{hc\lambda}{4\pi^2 P_{\text{BS}}}} \tag{2.4}$$

where $k = 2\pi/\lambda$, E_γ is the energy per photon, and P_{BS} is the power incident on the beamsplitter. Equation 2.4 shows that the sensitivity can be increased by using a more powerful

2. In correspondence with the optical power being equal to the square of the electric field ($P = E^2$), the reflected and transmitted *power* from an optic are described by coefficients $R \equiv r^2$ and $T \equiv t^2$, respectively.

laser. For example, using a 1watt laser, a shot noise limited sensitivity of $\Delta X_{\mathrm{DARM,shot}} \sim 7 \times 10^{-17}\mathrm{meters}/\sqrt{\mathrm{Hz}}$ can be achieved, compared to using 1kW of power which would give a sensitivity of $\Delta X_{\mathrm{DARM,shot}} \sim 2 \times 10^{-18}\mathrm{meters}/\sqrt{\mathrm{Hz}}$. In practice, stable continuous wave lasers do not yet exist at the powers necessary for these applications, where we typically strive for powers of a few kilowatts.

In lieu of modifying the laser setup, we can instead combine the Michelson and Fabry-Pérot interferometer configurations to form what is called a power-recycled Michelson interferometer, shown in figure (2.1c). The advantage of using such an optical configuration is that the light exiting the Michelson interferometer at the symmetric port can be reused, and the mirror at the input is called the power-recycling mirror (PRM) for this reason. If the resonant conditions for a Fabry-Pérot cavity are met, then the phase of the beam reflected back toward the beamsplitter from the PRM is the *same* as the phase of the "fresh" laser light just entering the interferometer by passing through the PRM, and the two beams are constructively reinforced, increasing the total power. The increased laser power incident on the beamsplitter is essentially equivalent to simply getting a more powerful laser in the first place, and there are more benefits to be discussed later in that the resonant cavity filters out laser frequency and amplitude noise. The cavity also reinforces the spatial profile of the beam in the transverse direction, which maximizes the ability of the beams in each arm to be able to constructively interfere.

The bottom two traces in Figure 2.3 show the predicted interferometer signals vs. arm length difference for a power-recycled Michelson, normalized to $P_{in} = 1$watt. Figure 2.4 shows actual measurements of these signals in an interferometer.

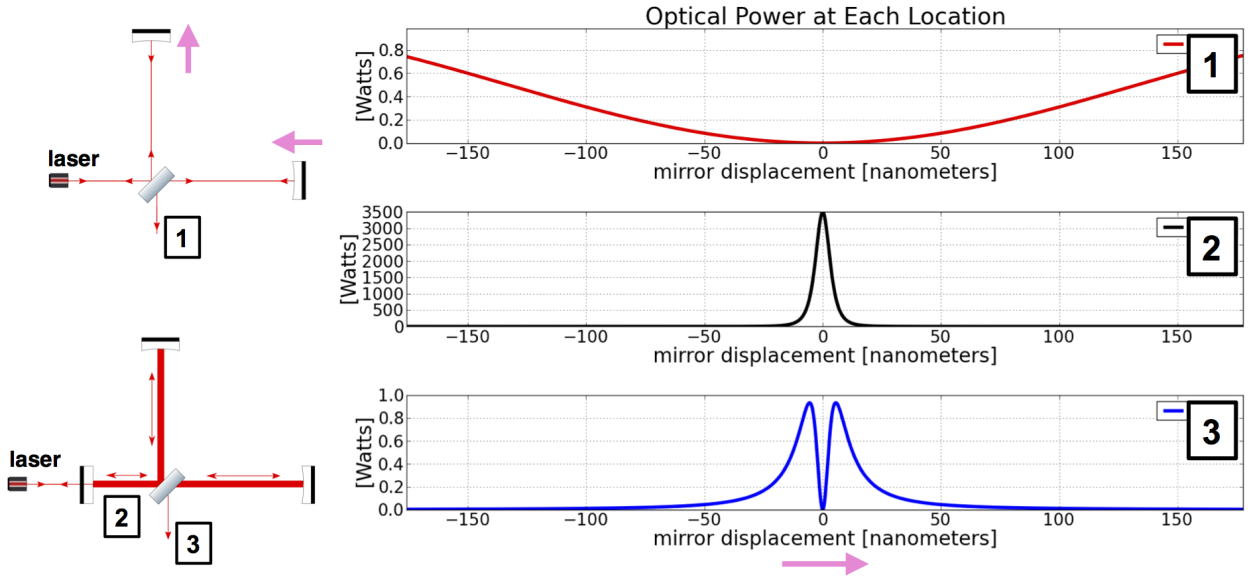

Figure 2.3: Predicted interferometer signals vs. differential arm length difference, normalized to 1 watt of input power. The red trace gives the output power for a Michelson interferometer shown in the upper left. The black and blue traces give the circulating power and output power for a power-recycled Michelson interferometer depicted in the bottom left.

2.4 Surpassing the Shot Noise Sensitivity Limit by Cross-Correlating Two Interferometers

Reaching shot noise limited performance in the first place is a large experimental effort, the details of which are discussed in Chapter 4. However, once the shot noise limit is reached, one can do even better than using a power-recycled Michelson interferometer, by using two identical and co-located power-recycled interferometers, and cross-correlating the outputs of the two. The shot noise (and other noises[3]) in each interferometer will be uncorrelated, so that cross-correlating the outputs allows one to be sensitive to signals well below the shot noise level of a single interferometer.

This technique produces sensitivities better than two orders of magnitude below the quantum shot-noise limit, within integration times of less than 1 hour. Figure 6.4 illustrates

3. For example laser phase and frequency noise. In practice a large campaign was launched to reduce the correlations between the lasers induced by radio frequency interference (RFI) and other contaminating sources. The details of the successful effort to reduce these correlations is discussed in Chapter 4

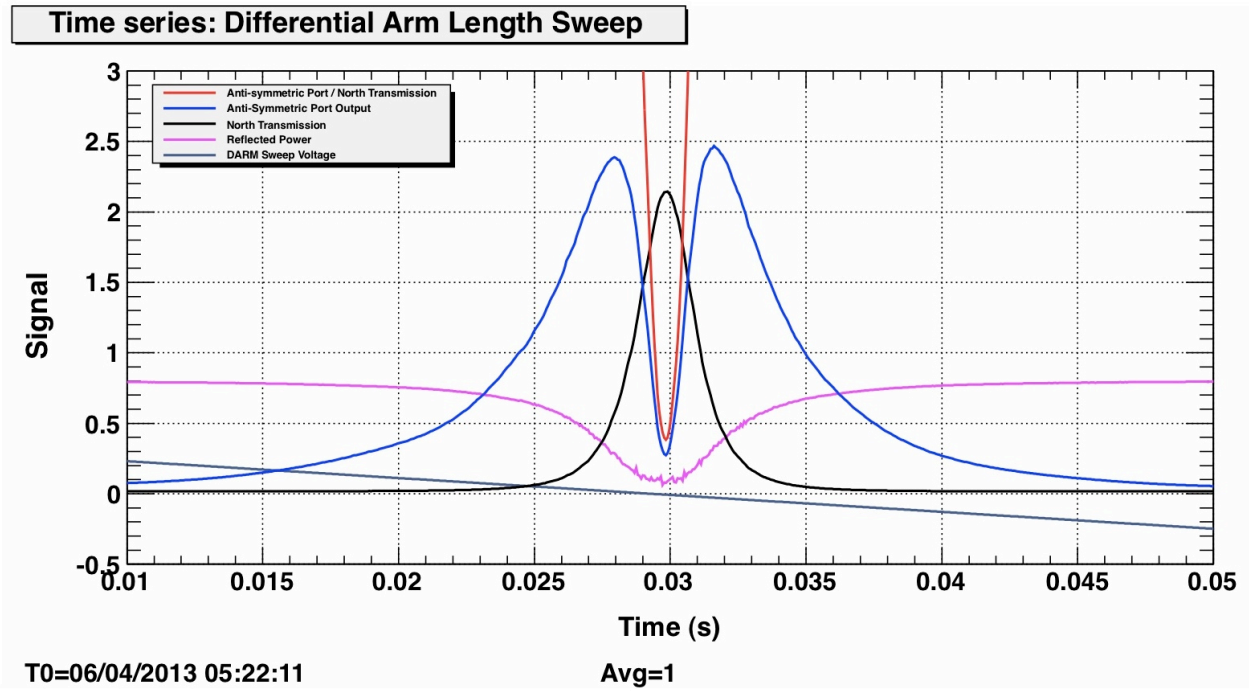

Figure 2.4: Measured interferometer signals vs. differential arm length difference. A sinusoidal sweep was applied to the end mirrors in DARM, while engaging the CARM control loop (c.f. section 3.7.1) with very low gain so that the laser frequency could still track the cavity resonance. The units on the vertical axis are arbitrarily scaled so that the traces all fit on the plot. The black trace labeled "North Transmission" is the signal from a photodetector sensing the small amount of power leaking out one of the end mirrors (it is linearly proportional to the power stored in the cavity). The red trace equals the blue trace divided by the black trace. The pink trace shows the power reflected from the power-recycling mirror back toward the laser.

the benefit of cross-correlating the two interferometers, and even the benefit of splitting a single interferometer's signal onto two separate detectors and cross-correlating them– the shot noise on each of the two photodetectors on a single interferometer is uncorrelated as well, and this turns out to be a very useful way of measuring the frequency and intensity noise on the beam at frequencies where the shot noise dominates the total noise power.

CHAPTER 3

EXPERIMENTAL SETUP

Real world interferometers are considerably more complicated than the idealizations presented in Chapter 2. This Chapter covers the actual experimental implementation of the dual power-recycled Michelson interferometers used in this work. Chapter 4 then details the various types of noise sources that must be thwarted, and how they are subdued.

First, to clear up some notation, the two interferometers in this experiment have been named the "L" and "T" interferometers[1]. An overall diagram of the core optical configuration is shown in Figure 3.1. The physical orientation of the real interferometers is such that North=Up and East=Right in figure 3.1. For this reason, these arms of the interferometers are referred to as the North and East arms.

3.1 Core Optics

The beamsplitter (BS), power recycling mirror (PRM), and two end mirrors (EM) constitute the "core optics" of the interferometer. The BS and EMs are the principle optics involved in the detection of the passage of gravitational waves (they are the "test masses" described in section 1.1), and together with the PRM, they have the most stringent demands on their quality. Tables C.3, C.4, and C.5 in the appendix give an overview of the specifications for the core optics.

As equation 2.4 shows, a principal requirement is to maximize the power buildup in the cavity in order to achieve the highest DARM sensitivity possible. The problem of coupling incident laser power into the power-recycling cavity is analogous to impedance matching in electronics. For optical cavities, the relative transmission of the mirrors dictates if the cavity is undercoupled, impedance matched, or overcoupled. The circulating power can be

1. The naming convention originates from their role in a separate experiment to search for Holographic Noise [10, 15].

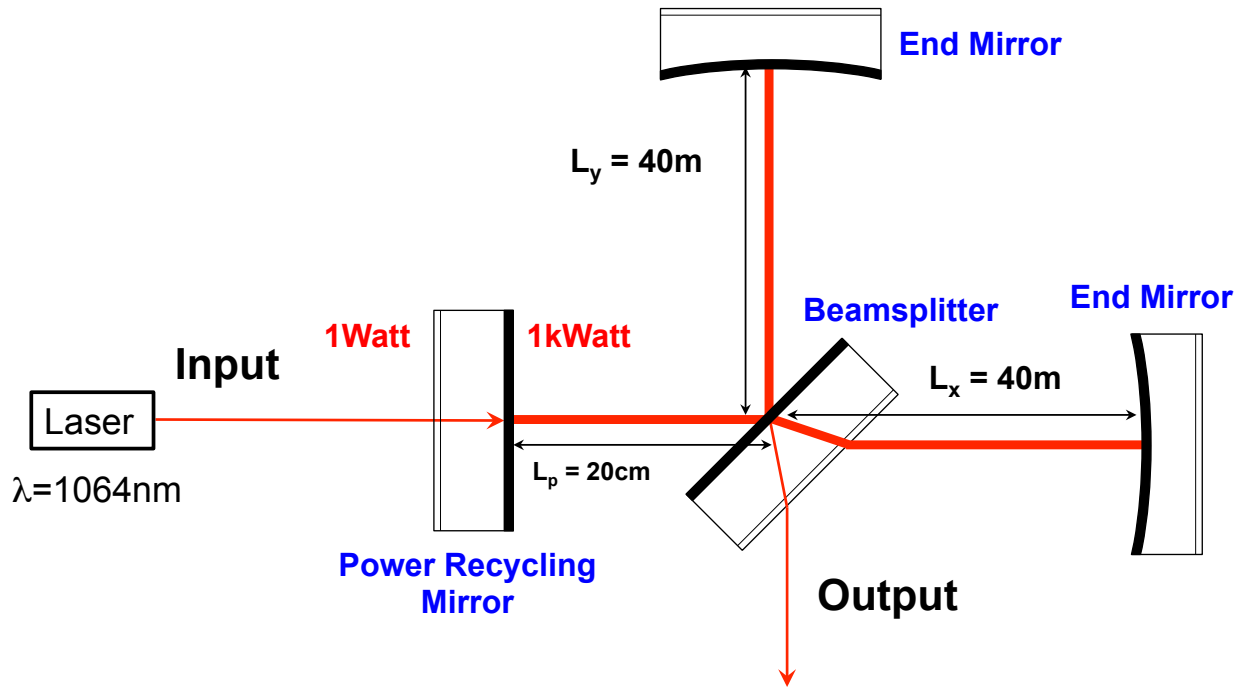

Figure 3.1: Core optical layout for a power-recycled Michelson interferometer in the Holometer experiment.

maximized when the input mirror (PRM) has a larger transmission than the end mirrors, in which case the cavity is overcoupled. Nominal transmission values of $T_{\mathrm{PRM}} = 0.001$ and $T_{\mathrm{EM}} = 10$ppm were chosen[2], which from equation 2.3 gives an expected cavity gain (in the ideal case of no losses) of $G_{\mathrm{cav}} \sim 3900$, with circulating power of ∼3.9kW for 1 watt of incident power. The total scattering and absorption losses of all the core optics must sum up to less than the PRM transmission, in order to maintain an overcoupled cavity. Actual cavity gains typically achieved in this experiment, which include all the real losses, are on the order ~ 3000. The data in this work was recorded with $P_{\mathrm{in}} = 0.56$W and $P_{\mathrm{circ}} = 1.9$kW in the T interferometer, and $P_{\mathrm{in}} = 1.2$W and $P_{\mathrm{circ}} = 2.7$kW in the L interferometer.

As equation D.12 shows, the mirror radius of curvature (ROC) and cavity length dictate

2. In reality we received end mirrors from the manufacturer which we measured to have $T_{\mathrm{EM}} = 0.5$ppm in the T interferometer, and $T_{\mathrm{EM}} = 1.5$ppm in the L interferometer

the resonant frequencies of higher order laser modes in the cavity. These parameters were chosen such that only high order TEM_{nm} modes would satisfy the resonance condition simultaneously with the fundamental TEM_{00} mode. The values $L = 40m$, $R_{\mathrm{PRM}} = \infty$ (flat), and $R_{\mathrm{EM}} = 75m$ were chosen, so that the first HOMs to be nearly co-resonant with the fundamental TEM_{00} mode have $n + m = 4$.

3.2 Vacuum System

The vacuum system houses the core optics, and its purpose is twofold:

1. Reduce the ambient air pressure: air molecules are a scattering centers for photons, and high pressures can induce significant phase noise on the laser beam. The total pressure in the interferometers is kept at an average of $\sim 10^{-8}$ Torr.

2. Shield the core optics from hydrocarbons: The danger of hydrocarbons is that the high-powered circulating beam can bake them onto the optical surfaces, creating scattering centers, extra loss, and phase distortions on the beam. These effects in turn can reduce the Finesse of the cavity, and so the power buildup. The partial pressure of hydrocarbons is kept at the $\sim 10^{-12}$ Torr level to ensure the purity of the optics[3].

3.3 Laser Launch

The laser and optical components for preparing the beam to be injected into the interferometer are all contained on a single large laser table, constituting the "laser launch". The laser launches for the L and T interferometers are shown in Figures 3.3 and 3.2, respectively.

The Holometer lasers are the Mephisto model manufactured by Innolight, which are diode-pumped nonplanar ring oscillator (NPRO) Nd:YAG lasers, with continuous wave (CW)

3. Cavity ringdown experiments at LIGO appear to indicate that this level is more than sufficient to maintain the required Finesse for long periods.

output at 1064nm. Before injection into the interferometers, the laser beams are prepared to ensure they are linearly polarized, and that they have a gaussian transverse profile with minimal phase distortion. There are many advantages to working with a gaussian-shaped laser beams, perhaps most importantly that they are the easiest to understand[4].

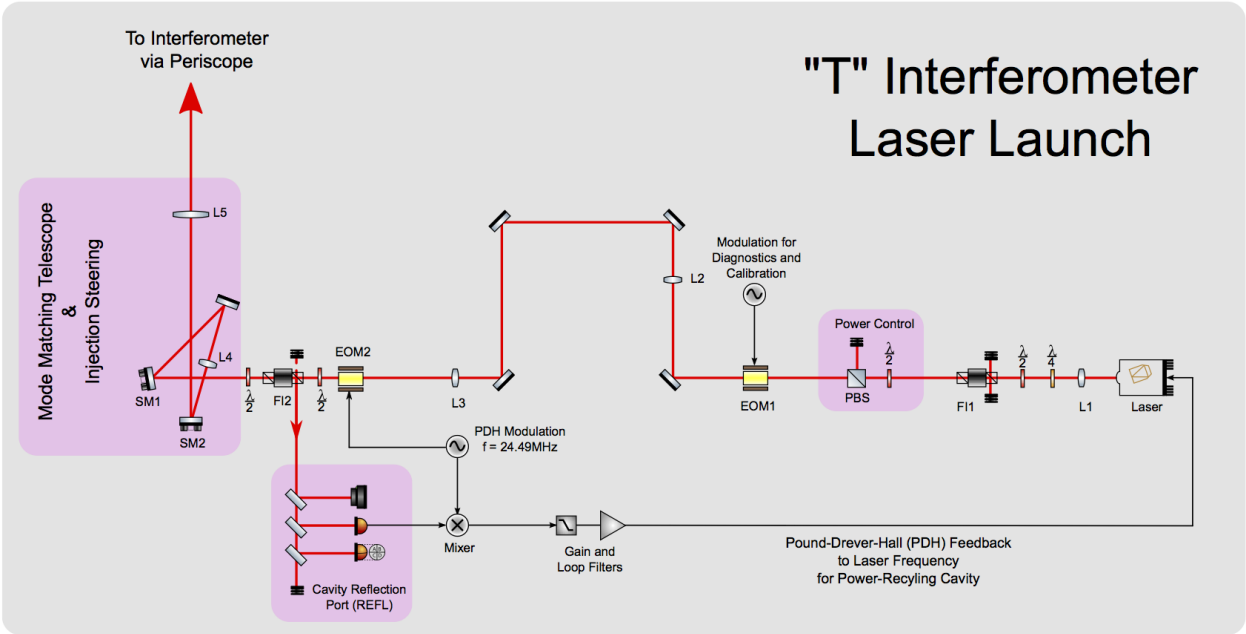

Figure 3.2: "T" interferometer laser launch.

Phase modulation sidebands are generated with the electro-optic modulator "EOM2", for use in the Pound-Drever-Hall locking scheme for the resonant power-recycling cavity described in section 3.7.1, with background theory in appendix D.2. The beam then enters a mode-matching telescope which matches the beam shape to the resonant mode of the power-recycling cavity (c.f. section 3.3.2).

There is also an auxiliary EOM ("EOM1"), which is used for diagnostic and calibration purposes, which is further described in section 5.1.3 of Chapter 5.

4. The interested reader is referred to any of the many thorough resources on gaussian laser beams, e.g. [22]. The theory of gaussian beams is only included here in so much as is necessary to explain the most salient features of the instrument. Those supplementary details are in the appendix section D.

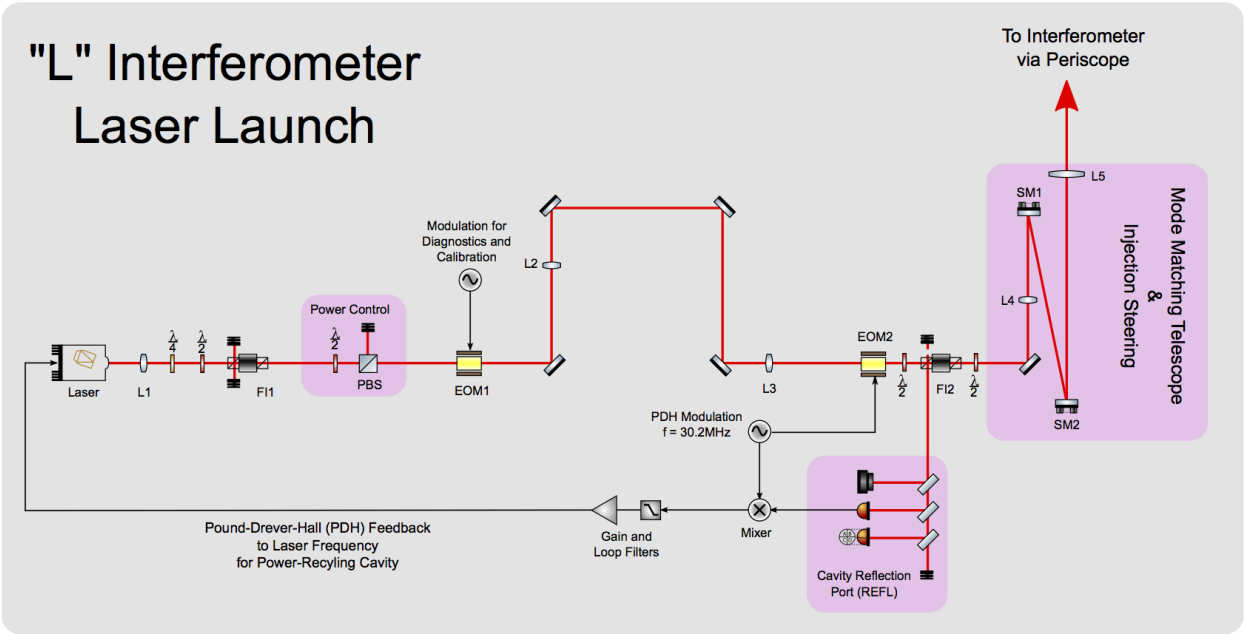

Figure 3.3: "L" interferometer laser launch.

3.3.1 Beam Purity

The original design of the Holometer experiment incorporated a resonant 3-mirror triangular "mode cleaning" cavity before injection into the interferometer [10], in order to filter out any residual higher order TEM_{nm} mode content from the beam, leaving only the fundamental gaussian TEM_{00} component[5]. However, it was later determined that the injected mode purity was sufficient, and that an initial mode cleaning stage was not necessary (the unusual square-like beam path in the middle of figures 3.2 and 3.3 was to accommodate the original mode cleaning cavity, which was later removed from both laser launches).

Our electro-optic modulators are commercial units from the company New Focus. It was noticed that the use of a potassium titanyl phosphate (KTP) crystal (New Focus model 406x) in our electro-optic modulators significantly reduced the wavefront distortion in the beam, compared to a Mg:$\mathrm{LiNbO_3}$ crystal (New Focus model 400x). For this reason, "EOM2" is the KTP type. We were, however, able to operate with "EOM1" being the Mg:$\mathrm{LiNbO_3}$

5. c.f. sections D.1 and D.4 for background material on higher order modes

type because of the power-recycling cavity's ability to significantly filter out higher order modes, as described below.

The power-recycling cavity does a great deal to filter out the higher order mode (HOM) content of the beam, in that the TEM_{00} is held resonant via the Pound-Drever-Hall locking scheme (c.f. section D.2), and the Gouy phase advance of HOMs with respect to the TEM_{00} (c.f. section D.4) then ensures that they do not simultaneously satisfy the cavity boundary conditions for resonance. Consequently, for the most part, the HOM content of the injection beam is promptly reflected from the power-recycling cavity, and does not enter the cavity or the antisymmetric port, which would contaminate the output signal beam.

Given that idealized view, there still does exist some residual HOM content resonating in the power-recycling cavities of both interferometers. This is because noise sidebands on the carrier TEM_{00} mode have some non-zero scattering coefficients to couple into HOMs (e.g. from injection misalignment which couples to odd-ordered TEM_{mn} modes, or end mirror radius of curvature mismatches which couple to even ordered modes). The Gouy phase advance then causes these HOMS to be resonant when their frequency (which is offset from the carrier TEM_{00} mode frequency) and mode numbers satisfy equation D.12 (see section D.4 for explanations).

The first three HOM resonances can be seen in the auto-spectrum traces of the antisymmetric port signal photodetectors in Figures 3.7, 3.8, 3.9, 3.10, where the power in these modes is somewhat larger than the shot noise (flat baseline). Great care was taken to optimize the alignment degrees of freedom, and as discussed above to specify strict tolerances on the optics geometries, in order to minimize the presence of resonating HOMs in the cavity.

3.3.2 Mode Matching to the Cavity

Mode matching is the process of manipulating the input laser beam so that its (complex-valued) electric field maximally overlaps with that of the resonant mode of the optical cavity.

It ensures the maximum amount of laser field is coupled into the cavity, and can be viewed as a form of impedance matching. The amount of mode matching can be quantified by the overlap integral

$$\eta \equiv \frac{\left|\int \mathrm{E}^*_{\mathrm{laser}} \mathrm{E}_{\mathrm{cavity}} \mathrm{d}A\right|^2}{\int |E_{\mathrm{laser}}|^2 \, \mathrm{d}A \int \left|E_{\mathrm{cavity}}\right|^2 \mathrm{d}A} \tag{3.1}$$

where $\mathrm{E}_{\mathrm{laser}}$ is the input laser beam's electric field, $\mathrm{E}_{\mathrm{cavity}}$ is the electric field of the resonant mode supported by the cavity, and the integral is performed in the plane perpendicular to the beam's propagation. If the full complex-valued fields $\mathrm{E}_{\mathrm{laser}}$ and $\mathrm{E}_{\mathrm{cavity}}$ are equal in a particular transverse plane (meaning $\eta = 1$), they will remain so along the beam's propagation.

Mode matching in the L interferometer was performed using a Mach-Zehnder interferometer that interfered the outgoing laser beam (propagating toward the interferometer) with the incoming laser beam (returning to the laser table after having been reflected off of the power recycling mirror). A 99% reflectivity beamsplitter on the laser table placed just before the mode matching telescope (the 99% reflectivity beamsplitter is the mirror icon just before lens "L4" in figure 3.3) provided 1% of the outgoing beam in one of its transmission ports, and 1% of the incoming beam in its other transmission port, so that the 1% samples of the incoming and outgoing beams were propagating at 90 degrees with respect to each other. Two steering mirrors then folded the two beams back onto each other where they were combined on a 50% beamsplitter, completing the Mach-Zehnder interferometer. A phase modulation was applied to the return beam by driving the piezo position actuators on one of the mode matching telescope mirrors ("SM1" in figure 3.3), which drove the Mach-Zehnder through several fringes. The z-position (i.e. along the direction of beam propagation) of the last mode matching lens was then finely tuned using a micrometer stage until the contrast defect (defined in equation 5.6) of the Mach-Zehnder fringes was minimized, which meant

that the overlap of the outgoing and incoming electric fields was maximized, which in turn meant that the beam waist had been properly placed at the power recycling mirror.

This technique resulted in 96% mode matching for the L interferometer (i.e. $\eta = 0.96$ in equation 3.1) as determined by the relative fraction of power reflected from the power-recycled cavity. mode matching for the T interferometer was $\sim 88\%$ at the time the data in this work was recorded (it had not yet been optimized with the above technique), and has since been made comparable to the L interferometer.

3.3.3 Intensity Noise Monitor

The high frequency intensity noise spectrum of the laser beam just before exiting the laser table is monitored with a photodetector placed on the transmission side of the 99% reflectivity beamsplitter on the laser launch (the 99% reflectivity beamsplitter is the mirror icon just before lens "L4" in figure 3.3). The signal from this intensity monitor is recorded in the high frequency DAQ (described in section 3.10.2), where its cross-spectrum is computed with the interferometer signal photodetectors and antennas (the cross-spectrum between the intensity monitors of both interferometers is also computed), providing an important tool to test for correlations between the two laser systems, which could mimic the signal of a gravitational wave.

3.4 Transfer Optics

After exiting the laser table, the beam is routed $\sim$ 20ft to the interferometers using three mirrors anchored to the wall of the tunnel. This transport scheme (called the "periscope") is necessary due to the limited space in the experimental hall (which is a long narrow concrete tunnel originally used to transport beams of mesons at Fermilab). The beam path along the periscope is in air at ambient pressure, but it is enclosed with aluminum pipes to shield from air currents. The noise properties of the periscope are discussed in section 4.6.

3.5 Signal Readout Optics

A diagram of the antisymmetric port optical setup is shown in the bottom left grey box of figure 3.4. Figure 3.4 highlights the setup during the calibration measurements made in the Michelson configuration described in section 5.1.1.

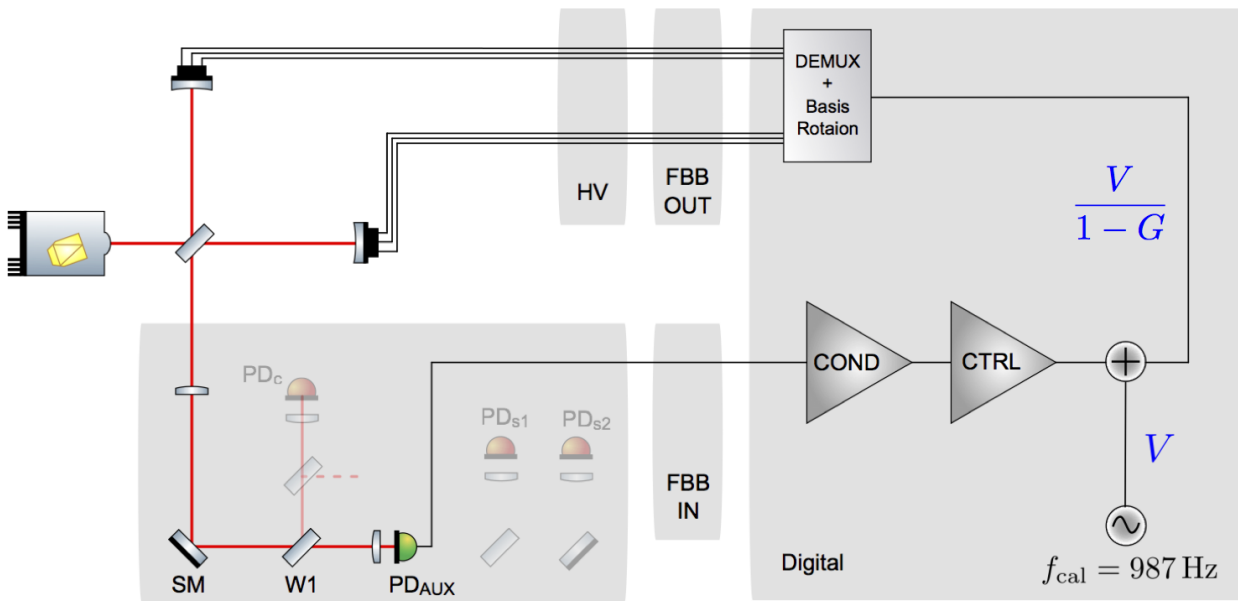

Figure 3.4: Configuration for measurements in Michelson mode. The DARM fringe is sensed with an auxiliary photodetector (green) on the AS-port to maximize SNR. The PD_{AUX} signal is sent to the filter buffer board (FBB), digitized, then conditioned ("COND", c.f. section 5.1.1.2). The calibration line is summed into the DARM loop after the Control ("CTRL") filter stage which applies gain and a loop filter with a single pole at 1Hz. The control signal is then demuxed into the 6 PZT channels (3 for each mirror) and matrix rotations applied to go from the DARM control basis to the PZT actuator basis. Control signals are then converted to analog and high voltage (HV) applied before driving the end mirror PZTs. The calibration line drive amplitude V is kept constant for all measurements, both in Michelson and power recycled configurations. Both the optical and sensing/control topologies change between Michelson and power recycled configurations, however the control path from the calibration line summing junction to the end mirror PZTs is unchanged throughout, and so the loop gain $G(f_{cal})$ must be measured directly in both cases to tranfer the calibration between configurations (c.f. sections 5.1.1.3 and 5.1.2.1). The PD_{AUX} detector is removed in power recycling configuration, and the AS-port optics and detectors used in power recycled mode are shown with partial transparency for reference.

The standard operating configuration in power-recycled mode (e.g. when taking science

data) has the green auxiliary photodetector "PD_{AUX}" removed, and the photodetectors PD_c, PD_{s1}, and PD_{s2}, along with the mirrors and lenses shown with partial transparency, all in use.

PD_c measures low frequency signals ($\leq$ 1MHz, although only 16kHz is usable by the low frequency DAQ described in section 3.10.1), which are sent to the low frequency DAQ in the same manner as depicted for PD_{AUX} in figure 3.4. The high frequency signal photodetectors are PD_{s1} and PD_{s2}, and they are digitized in the fast DAQ described in section 3.10.2. The details of the signal photodetectors are discussed in section 3.9.

1% of the antisymmetric port power is immediately picked off with a beamplitter "W1" to CCD cameras (not shown) and photodetectors for control and diagnostics functions, and the remaining 99% is sent to two signal photodectors by a 50/50 beamsplitter. Details of the signal PDs are in section 3.9.

3.6 End Mirror Transmission Optics

The power leaking out the end mirrors provides a useful measure of the stored cavity power. It is equal to the stored cavity power (shown for example in black in figures 2.3 and 2.4), attenuated by the transmission of the end mirrors (which was measured to be 0.5ppm for the T interferometer, and 1.5ppm for the L interferometer. As discussed in section 3.7.2, the transmitted light is also used in the feedback scheme to control the Differential Arm (DARM) degree of freedom.

The transmission optical setup also contains a CCD camera and iris used to align the interferometer beams and view the beam. Still images from the transmission CCD cameras are visible in the TV screens in figure 3.5.

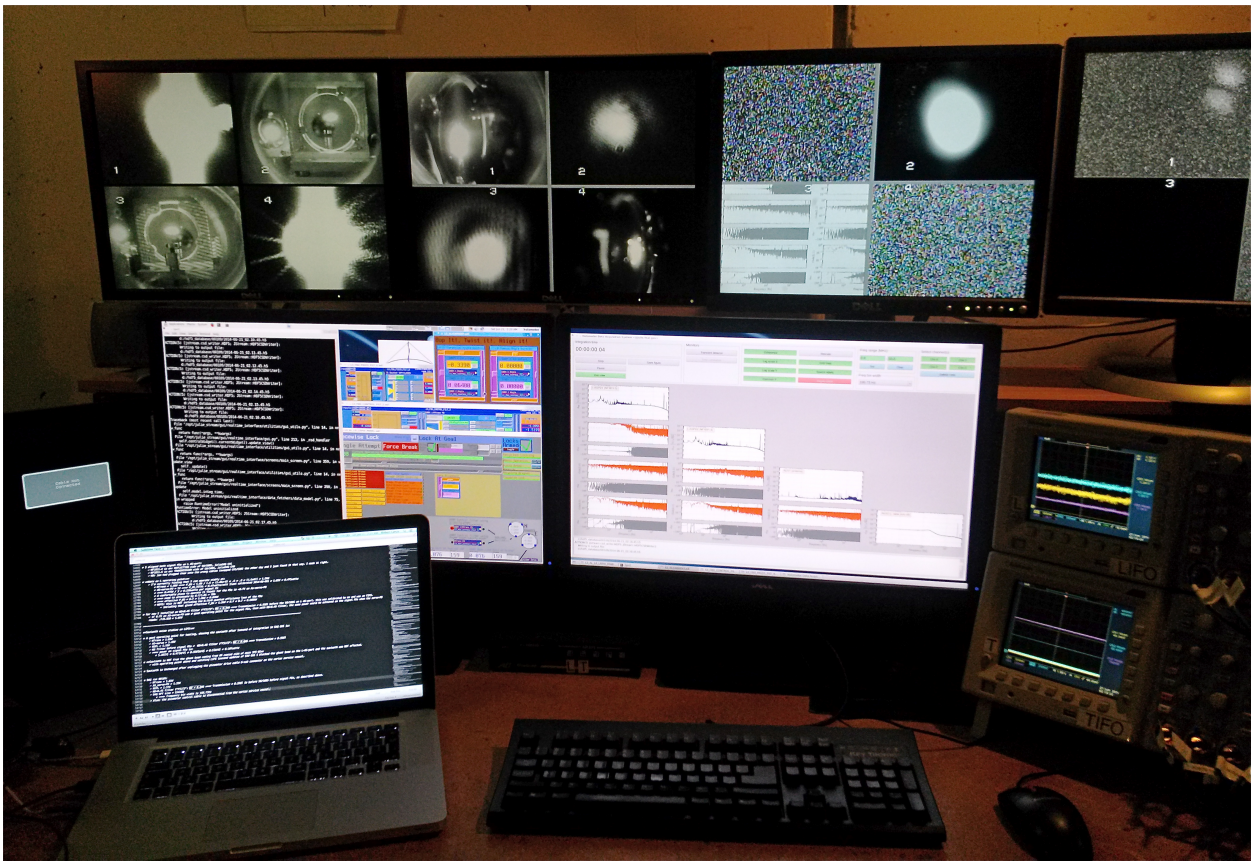

Figure 3.5: Control station screens in the tunnel, where both interferometers were piloted for the data runs in this work.

3.7 Feedback and Control

Equation (1.8) shows that if we hope to measure a gravitational wave strain with amplitude h, we must be able to keep the nominal separation distance between test masses L relatively constant, so that the perturbation h dominates the motions of the test masses. In an ideal world, we could simply plop the interferometer optics down in fixed locations, and they would remain there, unperturbed and with absolute stillness, until the passage of a gravitational induced a measurable length change. Of course the reality is that we are faced with the problem of having to constantly counteract the influence of many external noise sources from jostling the optics from their ideal locations.

Another very important reason to minimize the fluctuations in L can be seen in the

interferometer signals plotted in Figure 2.3. We'd like to keep the fluctuations in L (i.e. fluctuations on the x-axis of the plots) small enough so that the interferometer signals remain sufficiently linear in L. And as we'll also see, we don't want L to cross through zero, otherwise negative feedback will turn into positive feedback. Lastly, as Chapter 5 discusses, a full calibration of the interferometer is only as good as the stability of the operating point. The feedback systems hold the interferometer in a particular configuration corresponding to a specific arm length difference value on the x-axis in figure 2.3, and the calibration applies to that configuration. If the operating point is moved, the sensitivity will change, and so will the calibration, principally because the stored cavity power will also change (c.f. Equation 2.4).

This section outlines the feedback systems implemented in this experiment[6]. The various noise sources which necessitate the use of feedback are discussed in Chapter 4.

3.7.1 Common Arm (CARM) and Laser Frequency Sensing and Control

Until now we have mostly been talking about *differences* in the arm length, and correspondingly motions of the end mirrors in opposite directions (if one mirror moves toward the beamsplitter, then the other moves away). An orthogonal degree of freedom is the common arm (CARM) motion, where both mirrors either move in or out. CARM motion is important for maintaining resonance in the power-recycling cavity. The cavity can be thought of as a Fabry-Pérot cavity with a composite end mirror made up of the Michelson interferometer (BS and two EMs). CARM then controls the length of this cavity, whereas differential arm motion controls the reflectivity of the Michelson "mirror" (the reflectivity and transmission being dictated by equation 2.1). In this way, the problem of maintaining resonance in a power-recycled Michelson interferometer is reduced to arranging for the laser wavelength (or equivalently frequency) to track the motion in CARM (or vice versa).

6. A fairly good technical overview of feedback methods is given in [5].

We use the Pound-Drever-Hall (PDH) technique to hold the laser frequency locked to the CARM degree of freedom. The technical details of the PDH technique relevant for our application are given in the appendix D.2. Here we note that the PDH feedback loop is depicted in Figures 3.3 and 3.2, and the relevant noise properties of the laser (which is the dominant noise source in the CARM feedback loop) are discussed in section 4.2.

3.7.2 Differential Arm (DARM) Sensing and Control

The differential arm (DARM) degree of freedom is controlled using what is called a "DC lock", where motion in DARM is sensed by a photodetector on the transmission side of an end mirror. As the black trace in figure 2.3 shows, the stored cavity power exhibits a resonance around zero DARM offset. However, an appropriate error signal needs to change sign on either side of the desired operating point, and since all of the traces in figure 2.3 have either a minimum or maximum at zero DARM offset, that operating point cannot be used to derive an error signal with only the light intensities shown in the figure[7]. For this reason we subtract a small DC offset from the transmitted power signal, so that the signal does cross zero when DARM is at some small offset value. This type of lock is therefore referred to as a "DC lock", or an "edge lock".

Each end mirror is mounted with 3 piezo actuators which are used to control the mirror's position via the digital control system described in section 3.10.1. The transmitted power is sensed with the photodetector on the North transmission optics breadboard, and then digitized in the slow DAQ. The DC offset is then added and control filters applied to the signal to help suppress the dominant noise sources (as described in section 4.6). The control signal is then demuxed into the 6 PZT channels (3 for each mirror) and matrix rotations

7. There are several methods for generating an appropriate error signal at zero DARM offset by using a dither, which ultimately returns the derivative of the traces here and so they do cross zero (e.g. LIGO originally operated this way), however they require significantly more work to calibrate and extract meaningful scientific results from, and importantly they typically involve high frequency dither signals in the MHz range, which could ultimately contaminate our signal band.

applied to go from the DARM control basis to the PZT actuator basis. Control signals are then converted to analog and high voltage (HV) applied before driving the end mirror PZTs.

An important question is how stable we need to keep DARM motions in order to hold the interferometer in a reasonably linear region of the response according to the traces in figure 2.3. From the blue trace, we can see that differential motions of the end mirrors by more than just a few nanometers will change the operating point from being "inside" the volcano-like response curve, to operating on the "outside" (left or right of the peaks). If we were to lock DARM to the antisymmetric port power, the fluctuation in operating point to the outside of the volcano would change the sign of the DARM loop error signal, creating positive feedback, which would drive the interferometer even further from the desired operating point. This is the reason for locking to the transmitted cavity power, which does not experience a sign change at the volcano peaks.

It is also very important to note from the cavity power (black trace) that large changes in cavity power can occur as well for small DARM motions, resulting in large changes in sensitivity as per Equation 2.4. For these reasons we lock the DARM degree of freedom to have a total RMS motion of far less than a few nanometers.

Figure 3.6 shows low frequency spectra of the antisymmetric port signals in each interferometer (corresponding to the blue trace in figure 2.3) with the interferometers locked as described above, during the data taking runs in this work. The spectra were calibrated in units of meters/$\sqrt{\text{Hz}}$ of DARM motion using the method described in Chapter 5[8]. These plots show that the DARM control loop in each interferometer has suppressed the differential motion of the end mirrors to a **total RMS motion of less than 1 Angstrom**. This very small level of total RMS motion allows for the interferometers to be held at an operating point very close to the dark fringe (consequently maximizing the stored cavity power, and therefore maximizing the sensitivity), while still maintaining a sufficiently linear

8. The low frequency signals are calibrated in the same way as described in Chapter 5, however the extra steps of transferring the calibration to higher frequency and to the signal photodetectors is not needed

output response to fluctuations in DARM. Maintaining a linear output response to DARM motion means there is no nonlinear harmonic generation or distortion products which could significantly cloud the interpretation of the DARM spectrum in the signal band, in addition to generating instabilities in the feedback loops.

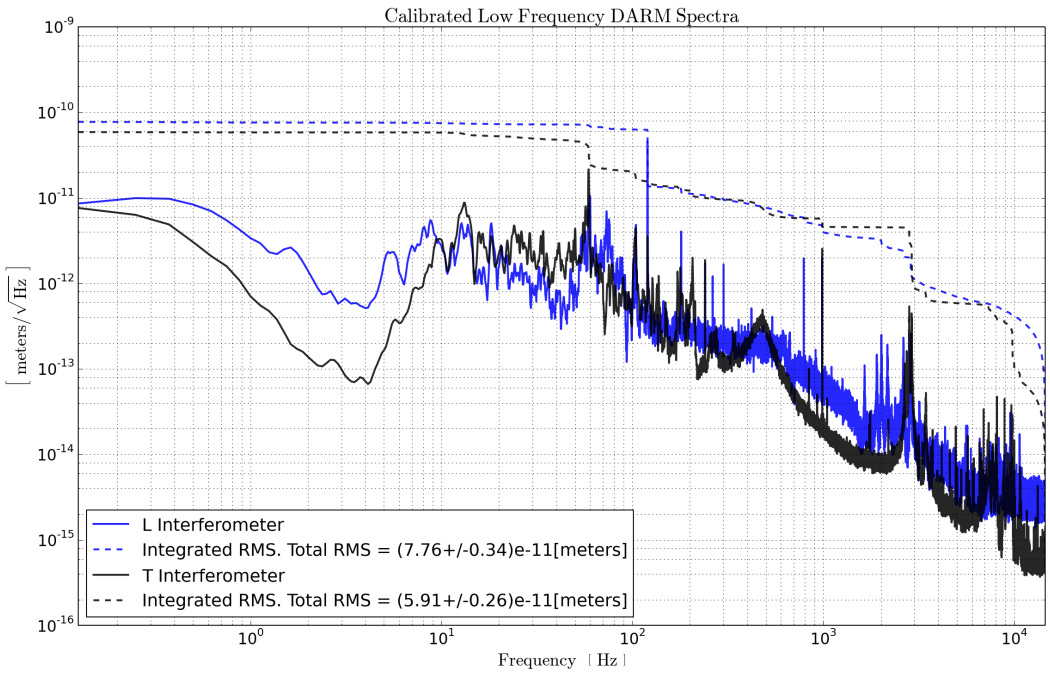

Figure 3.6: Low frequency residual power-recycled DARM spectra, calibrated in meters/$\sqrt{\text{Hz}}$. This is the residual DARM motion in power recycled operation. Of particular note is the total RMS differential arm motion (DC limit of dashed lines) for each interferometer, which is below 1 Angstrom, allowing for stable high power operation.

3.8 Alignment

In addition to the two longitudinal degrees of freedom DARM and CARM, the mirrors can move in angle as well. In practice, as is mentioned in section 4.6, we were able to suppress all angular motions of the optics with passive isolation methods, and so active feedback from not necessary. This section briefly outlines the relevant alignment issues.

3.8.1 Injection Alignment

The two steering mirrors "SM1" and "SM2" in the mode matching telescope in figures 3.2 and 3.3 together with the last of the three periscope mirrors provide all the dynamic range necessary for keeping the injection beam aligned with the power-recycling cavity. "SM1" and "SM2" are equipped with piezo actuated steering knobs, but in practice it is only necessary to optimize the injection alignment every once in a while by hand. The last periscope mirror is placed a few feet from the PRM, and it is seated in a picomotor-actuated mount to help in the event that gross (re)alignments are needed.

3.8.2 Common and Differential Angles

The 3 piezo actuators mounted on each end mirror are capable of controlling the longitudinal position of the mirror, as well as angular motions. A quadrant photodetector placed on the anti-symmetric port while driving the mirrors in piston mode is used to orthogonalize the piezo drive in the 3 directions. The relative gain for the drive in each piezo is stored in the digital control system. As mentioned above and in section 4.6, the core optics (BS, PRM, EMs) are all mounted on top of a passive seismic isolation system consisting of viton ball springs and heavy steel plates, which damp seismic vibrations above $\sim 10Hz$. the vacuum system in which the isolation stages sit is bolted directly to the concrete floor of the tunnel. No elaborate suspension systems are needed to isolate the optics, because our signal band is in the MHz frequency range, where seismic and other vibrational noise sources are negligible. We only require enough vibration isolation to hold the interferometer at a stable lock point, as described in section 3.7.2. This is one great simplifying feature that our smaller / higher frequency system has compared to the larger interferometers such as LIGO and VIRGO.

As with the last periscope mirror, the BS and PRM are also equipped with picomotor actuated mounts for gross alignment needs, but these degrees of freedom are not actively controlled while the experiment is running.

3.9 Signal Photodetectors

The two main requirements for our signal photodectors are that they have response in the MHz frequency range, and that they can operate linearly with very high incident optical power, on the order $\sim$ 150mW (in practice we operate them with $\leq$ 100mW to have a safe margin). The reason for the latter requirements is what is called the contrast defect of the interferometer (defined in equation (5.6))– If the electric fields of the laser beams recombining at the BS are not perfectly matched in shape, meaning their decomposition in terms of Hermite-Gauss polynomials in equation D.1 are not the same, then there will be regions of the electric fields which cannot constructively or destructively interfere, and so the two beams simply travel independently of each other, with 50% of the non-interfering part traveling to the antisymmetric port. We term this extra light "junk light", because it carries no useful information about the DARM (or CARM) positions of the end mirrors, and so no scientific information about possible gravitational waves. The junk light simply adds more noise to the signal readout.

The net effect of the contrast defect is to fill in the red trace in Figure 2.3, so that even when DARM truly is at zero offset, there is still light exiting the antisymmetric port (all junk light in this case).

The signal photodetectors we use are commercially available New Focus model 1811 detectors, which have been extensively modified to handle these very high power levels, while still retaining very low noise performance and exceptional RFI shielding (c.f. section 4.5).

In order to avoid saturating the photodetector's transimpedance amplifier with the very large DC photocurrent and the large low frequency intensity modulations induced by seismic noise, the photocurrent is high-pass filtered at 200kHz. The exclusion of the low frequency signal by the high-pass filtering stage does, however, result in a more complicated calibration scheme for the interferometer sensitivity (c.f. section 5), where the low frequency modulation

signal used to calibrate the interferometer must be sensed with a separate low frequency photodetector and then transferred to the high frequency output of the signal detector.

3.10 Data Acquisition

There are two main data acquisition systems in the experiment. One operating at 16kHz Nyquist frequency used to control of the DARM degree of freedom as well as monitoring low frequency interferometers and seismometer channels ("slow DAQ"), and another operating at 50MHz Nyquist, which processes all of the high frequency data for the interferometer signal photodetectors, auxiliary detectors, and antennas.

3.10.1 Slow (Control)

The slow DAQ for each interferometer consists of 16 analog inputs channels and 16 analog outputs. The analog signals are passed though a custom signal filtering and buffer board (FBB) unit and the inputs are digitized at 32kHz. Digital control filters (poles, zeros, mixers, dividers) are then implemented in the time domain via digital biquad filters in an FPGA, which has on the order of 1K programmable filters. The high level interface uses a combination of "MEDM: Motif Editor and Display Manager", control software inherited from LIGO, and custom software[9].

3.10.2 Fast (Signal)

The high frequency DAQ consists of 4 National Instruments crates, each with a single 2-channel ADC + GPS phase lock for synchronization, which altogether digitize a total of 8 analog channels directly in the tunnel, in close proximity to the signal photodetectors. The 8 analog channels are sampled at 100MHz, giving a 50MHz of usable bandwidth. The digitized

9. The slow control system will be part of the thesis of another graduate student Lee McCuller.

timeseries data is then sent via fiber optic cables several yards away to our operations center for processing, and the optical link ensures minimal cross-talk between channels (crucial for reducing correlations between interferometer signals). Each 1 second long data segment from all 8 channels is Fourier transformed and cross-spectra are then computed between all 8 channels on a 32-core machine in real time. The final cross-spectrum data and supporting metadata is saved in HDF5 format for later processing offline. More details concerning the data analysis are given in section 6.1.

In addition to the 4 signal photodetectors, the DAQ is fed the intensity monitors from each laser launch, as well as two loop antennas placed in the tunnel in order to veto electromagnetic correlations also detected in the ambient RF environment (c.f. section 6.3 where this was used in the data analysis).

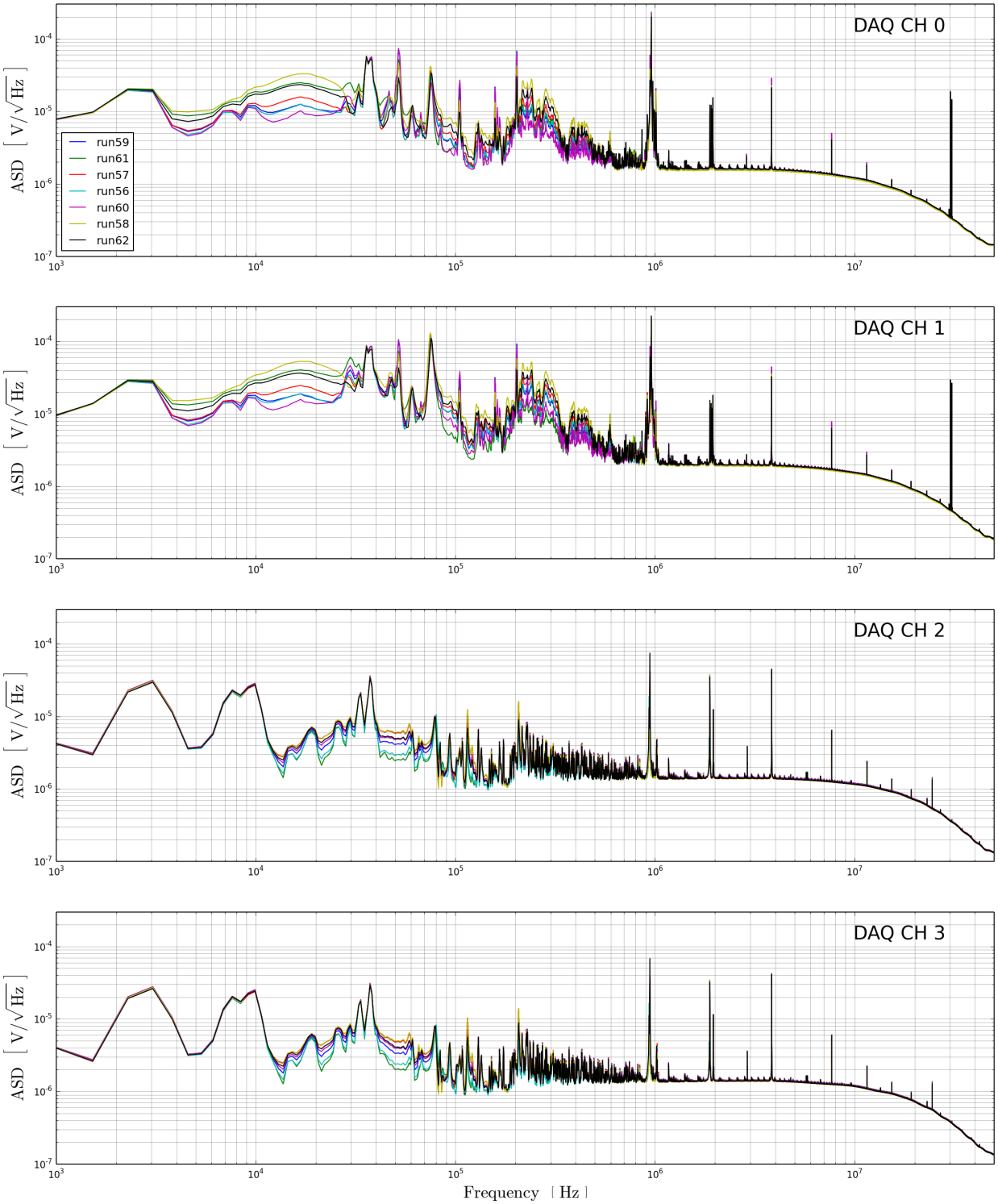

Figure 3.7: All 4 signal photodetectors for the 7 data runs in this work (DAQ Runs 00156-00162, labeled here "run59"-"run62"), plotted over the full 0-50MHz range of the DAQ. CH0 and CH1 are the L interferometer, CH2 and CH3 are the T.

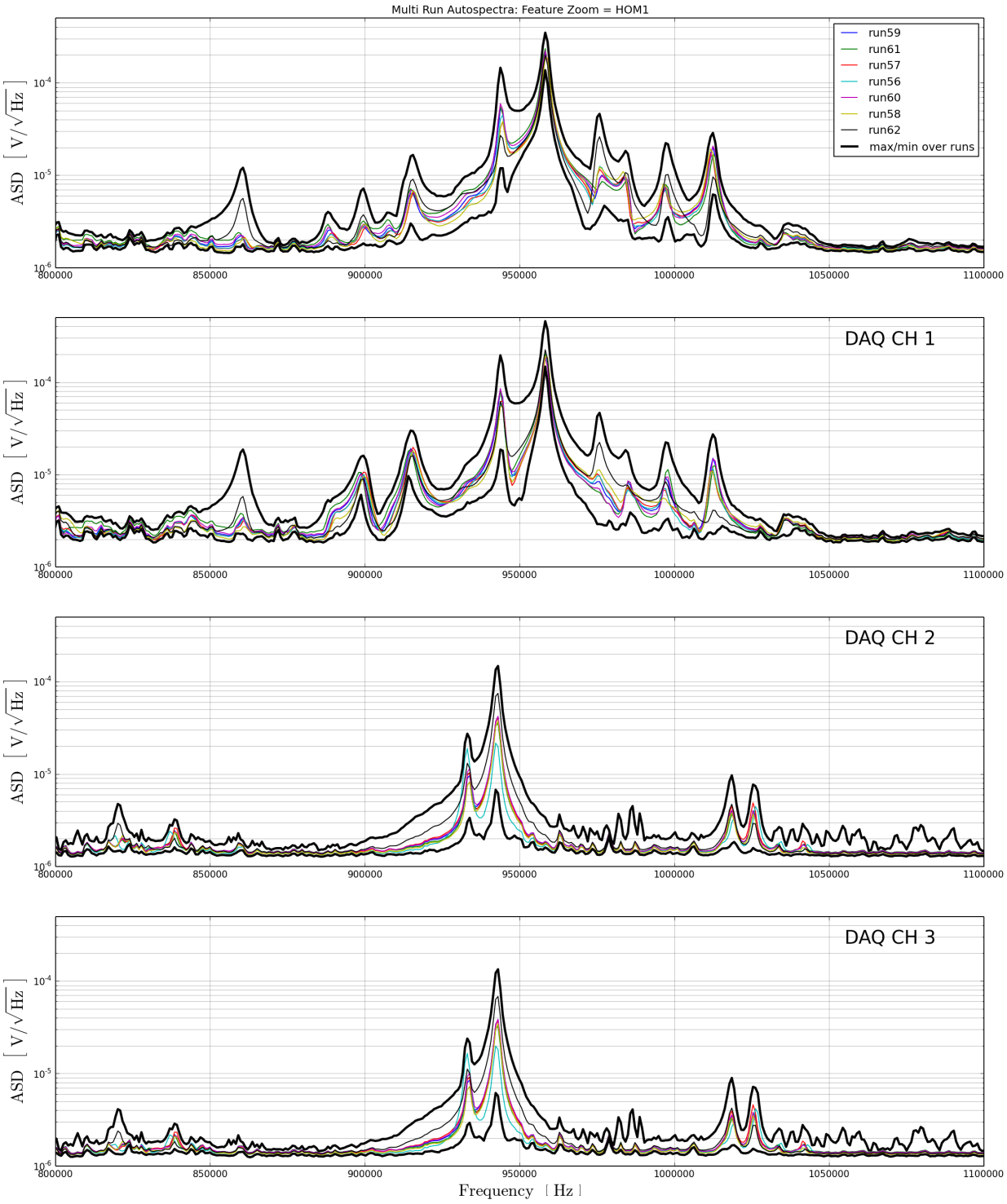

Figure 3.8: DAQ Runs 00156-00162 All 4 signal photodetectors: 1st Higher Order Mode, which is excited by laser noise coupling into it. CH0 (top) and CH1 are the L interferometer, CH2 and CH3 are the T. The thick black traces are the max and min values in each frequency bin over the entire 1 hour of data, over all 7 data runs. The colored traces are the mean values for each data run.

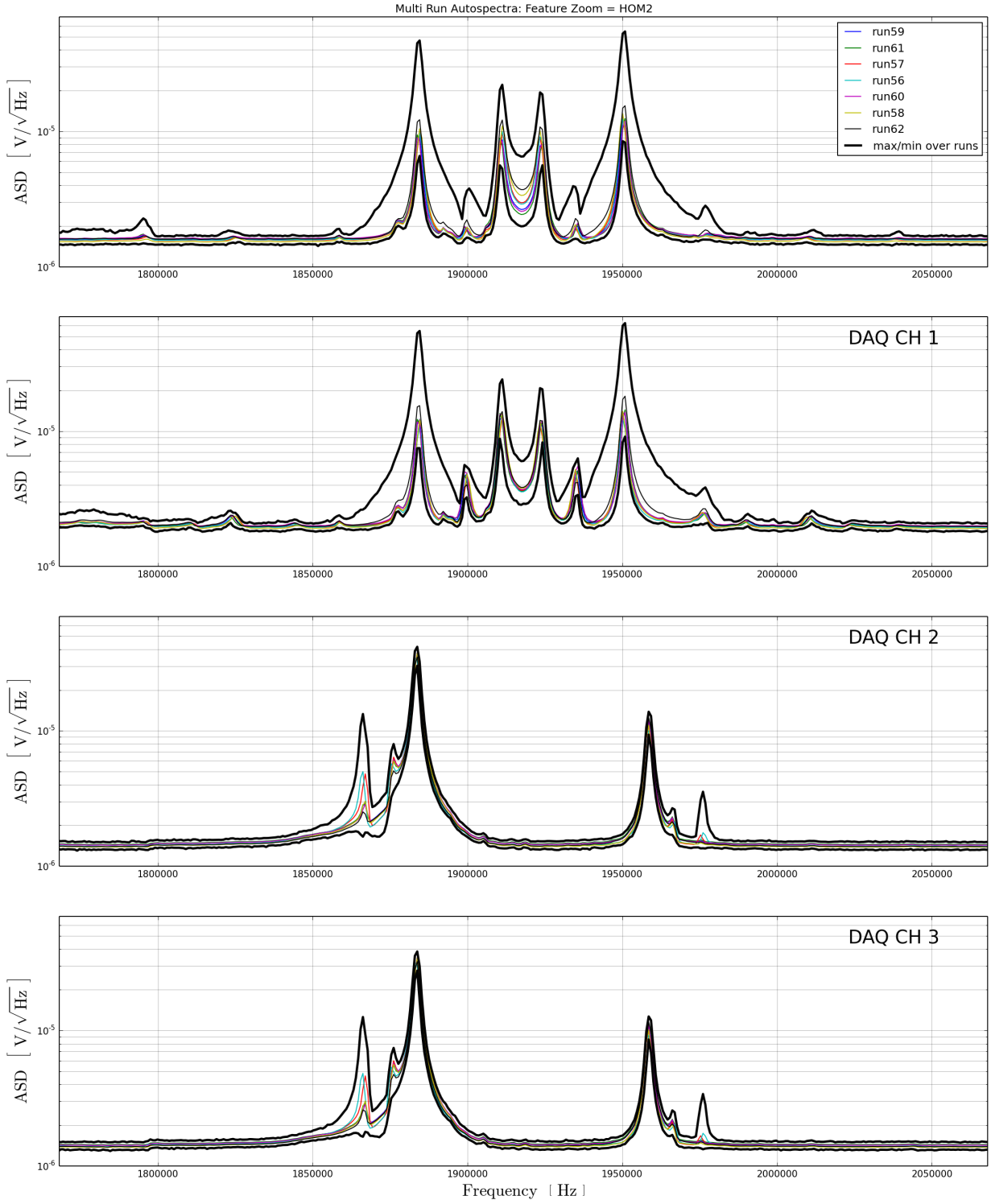

Figure 3.9: DAQ Runs 00156-00162 All 4 signal photodetectors: 2nd Higher Order Mode, which is excited by laser noise coupling into it. CH0 (top) and CH1 are the L interferometer, CH2 and CH3 are the T. The thick black traces are the max and min values in each frequency bin over the entire 1 hour of data, over all 7 data runs. The colored traces are the mean values for each data run.

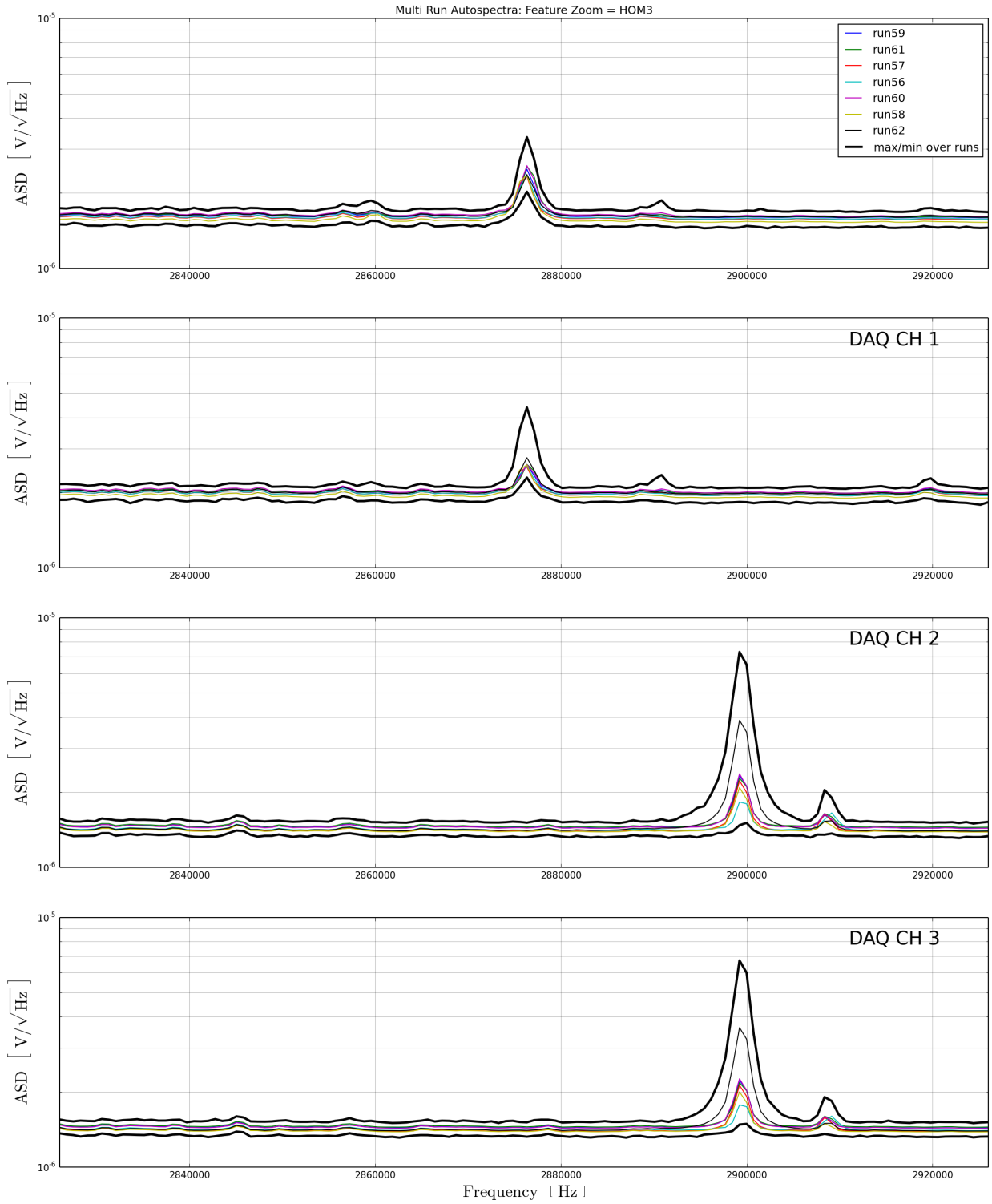

Figure 3.10: DAQ Runs 00156-00162 All 4 signal photodetectors: 3rd Higher Order Mode, which is excited by laser noise coupling into it. CH0 (top) and CH1 are the L interferometer, CH2 and CH3 are the T. The thick black traces are the max and min values in each frequency bin over the entire 1 hour of data, over all 7 data runs. The colored traces are the mean values for each data run.

CHAPTER 4

NOISE SOURCES AND COUPLINGS

Noise sources can be divided into two categories based on their frequency range:

- Low Frequency: $\lesssim$ 100kHz – Relevant to control system and operating stability
- High Frequency: $\gtrsim$ 500kHz – Relevant for science data

The key results of this Chapter and the vigilant experimental campaign to tame these noise sources is summarized here:

- **Low Frequency Noise:** Figure 3.6 shows that the sum of all noise sources in the DARM degree of freedom after the application of control loop and passive isolation suppression techniques has been reduced to less than 1 Angstrom total RMS, which meets the requirement for stable high power operation close to the dark fringe (c.f. section 3.7.2).
- **High Frequency Noise:** The two gray traces in Figure 6.4 are the cross-spectra between signal photodetectors in a single interferometer, and they show that the sum of all high frequency noises on the laser beam in each interferometer is at or below the shot noise level (which is the flat / white noise). Also, and most importantly, the cross-correlation between the two interferometers (blue trace) shows negligible contamination after 1 hour of integration, which allows for clear statements to be made about MHz frequency gravitational waves.

4.1 Schnupp Asymmetry

The net arm length difference ΔL between the two interferometer arms is called the Schnupp asymmetry, and it facilitates the conversion of injected frequency noise at the interferometer

input, to intensity noise at the AS-port (which mimics a DARM signal), in a manner linearly proportional to the imbalance ΔL. The apparent DARM motion $\mathrm{ASD}_{\Delta X,\mathrm{apparent}}$ at the antisymmetric port (in units of meters/$\sqrt{\mathrm{Hz}}$) is related to the injected frequency noise $\mathrm{ASD}_{\mathrm{freq}}$ (in units of Hz/$\sqrt{\mathrm{Hz}}$) by:

$$\mathrm{ASD}_{\Delta X,\mathrm{apparent}} = \frac{2\Delta L\lambda}{c} \cdot \mathrm{ASD}_{\mathrm{freq}} \tag{4.1}$$

where $\lambda = 1064$nm is the laser wavelength. The Schnupp asymmetry was measured in each interferometer by locking the Michelson at half fringe (no power recycling), modulating the laser frequency, and measuring the transfer function to the AS-port. Knowing the Michelson DARM calibration (see Chapter 5) and the magnitude of the laser frequency modulation, Equation (4.1) then gives the Schupp asymmetry. The measured values in each interferometer were: $\Delta L_{\mathrm{T}} = 1 \pm 1$[cm], $\Delta L_{\mathrm{L}} = 5 \pm 1$[cm].

4.2 Laser Frequency Noise

There are two main requirements for the laser frequency noise:

1. The residual RMS frequency noise (with the CARM control loop engaged) must be much less than the PR cavity resonance width, to enable stable common mode locks.

2. The frequency noise appearing at the AS-port as intensity noise due to the Schnupp asymmetry (c.f. section 4.1) must be below the shot noise in our signal band. (This is not a strict requirement for gravitational wave searches, however, it is for the Holographic Noise search [10]).

The frequency noise around the 280THz carrier of both Holometer lasers was measured by optically heterodyning the two lasers onto a fast RF photodiode, and using the resulting

beat note to phase-lock the two lasers at a fixed relative frequency offset. The spectrum of noise around the beat note is then the quadrature sum of the frequency noise from each laser individually, converted to intensity noise by the optical mixing.

Figure 4.1 shows the measured laser frequency noise, together with a modeled estimate of the CARM loop suppression of frequency noise while power recycling. The total RMS of the free running ("Out-of-Loop") laser frequency noise was measured to be $\sim 260\text{Hz}_{\text{rms}}$ (in good agreement with previous measurements of the same model lasers [16]). The CARM loop typically has a unity gain frequency (UGF) of $\sim$ 20kHz, which results in a suppression of the RMS frequency noise to $\sim 30\text{Hz}_{\text{rms}}$ or so. This is less than 1/10th of the half width at half maximum of the power recycling cavity resonance (also called the "cavity pole"), which allows for stable power-recycled locks.

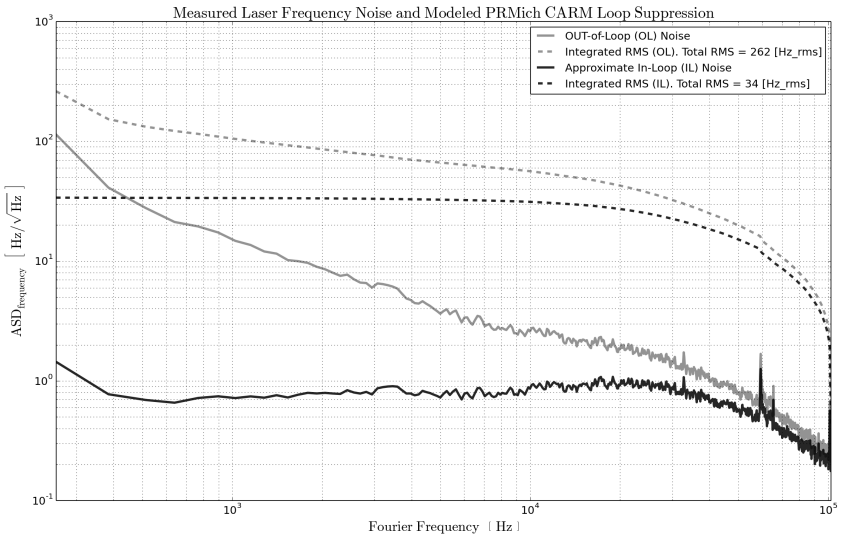

Figure 4.1: Measured laser frequency noise and modeled CARM loop suppression in power-recycled operation. The grey trace is the measured free-running (no control loops) frequency noise of the Holometer lasers (it is an average of the noise in both Holometer lasers). The black trace is an estimate of the residual laser frequency noise with the CARM control loop engaged. The salient feature is that the estimated in-loop residual frequency noise has a total RMS of $\sim$ 34Hz, which is less than 1/10th of the half width at half maximum of the power recycling cavity resonance, allowing for stable power-recycled locks.

4.3 Laser Intensity Noise

Laser intensity noise is characterized by the normalized intensity fluctuations, referred to as Relative Intensity Noise (RIN):

$$RIN \equiv \frac{\Delta P}{P} \tag{4.2}$$

where P is the DC optical power, and ΔP is the AC spectral density of power fluctuations. As with the laser frequency noise, it is desirable for the magnitude of the intensity noise to be smaller than the shot noise in the signal band. The intensity noise of the laser at 1MHz is dominated by the relaxation oscillations in the laser, and the Mephisto laser unit itself has an internal feedback loop which senses the excess noise and controls the pump diodes to compensate (this feedback loop is called the "noise eater"), resulting in a large suppression of the relaxation oscillation peak. Figure 4.2 shows the relative intensity noise of one of our lasers, as measured by the manufacturer (which is typical for both of the Holometer lasers). Before injection into the interferometer, the relative intensity noise is still larger than the shot noise up to a few MHz, however the cavity pole of the interferometer acts as a 1/f low pass filter for intensity noise. The cavity pole during the data runs in this work was $\sim$ 330Hz in the T interferometer, and $\sim$ 400Hz in the L interferometer, resulting in a larger than $\times$2000 suppression of intensity the noise at 1MHz, so that the relative intensity noise is below the shot noise.

4.4 Sawtooth Noise

The "Sawtooth noise" is a spectral feature which appears on both interferometers individually, with nearly identical morphology, however it does not correlate between the two interferometers. It can be seen as the gray traces in figure 6.4, which are the cross-spectra

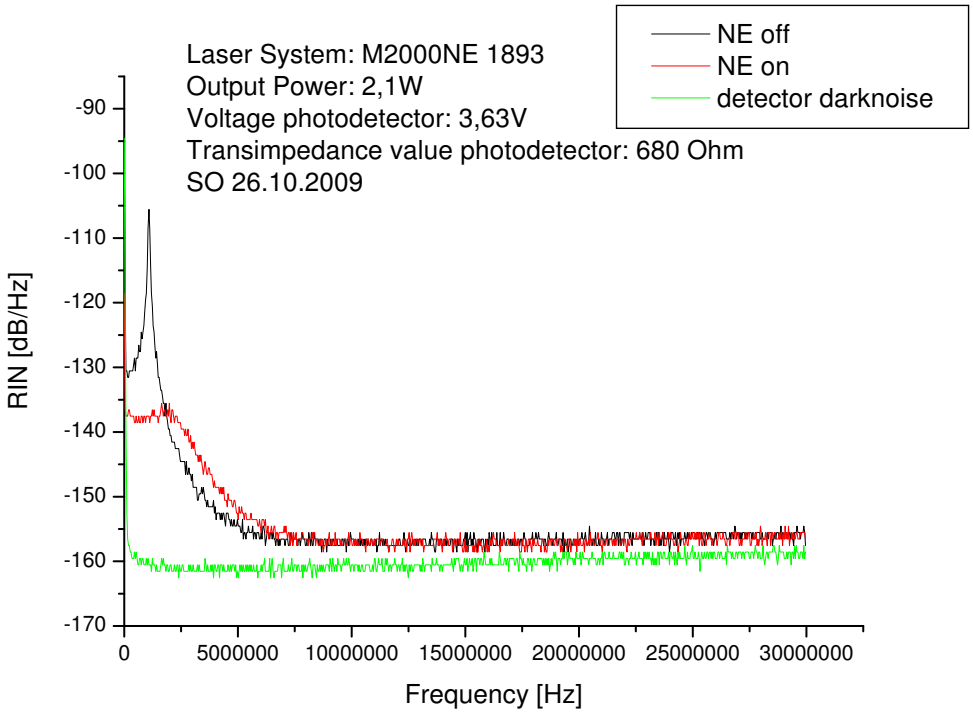

Figure 4.2: Measured relative intensity noise of one of the Innolight Mephisto laser for the Holometer (typical for both lasers). "NE" stands for "noise eater", which is the internal intensity noise suppression feedback loop in the laser.

of the signal photodetectors on a single interferometer (i.e. each trace only measures the noise in a single interferometer). It is mentioned here for completeness, although to this date its origin is unexplained. One current suspicion as of this writing is that this noise may possibly be due to the vibrational eigenmodes of the fused silica substrates for the core optics (beamsplitter, end mirrors, and power-recycling mirror), however this remains to be proven. The important fact is that it is NOT correlated between the two interferometers, and so it cannot be mistaken for a real gravitational wave signal.

4.5 Radio Frequency Interference (RFI)

A large experimental campaign was launched to mitigate contaminating noise sources in the MHz frequency range, as this is the primary signal band. At these frequencies, seismic and

mechanical noise sources are not so much a problem, as it is rather difficult to couple much mechanical energy into massive objects at MHz frequencies. Rather, the primary sources of noise in the MHz frequency range are electromagnetic in nature, for example local radio stations, electrical cross-talk, and ground loops.

The largest challenges were in shielding the signal photodetectors from ambient radio frequency interference (RFI), as well as electrically isolating the two lasers from each other in order to minimize spurious correlations between the two interferometer systems. Initially, it was found that there was a significant amount of RFI correlating between the signal photodetectors as well as between the lasers, which could be traced to the power source in the tunnel which was coupling common mode noise between nearly all of the electrical subsystems. This was in fact somewhat fortunate that most of the noise had a similar common mode nature, because a significant amount of reduction in RFI was achieved using toroidal ferrite common mode chokes, heliax coax cables, and similar techniques. Some amount of experimentation was done to find ferrite materials which absorbed RF energy in the MHz range very well, and it was a fairly tedious and incremental process to sequentially isolate each and every subsystem, requiring great care to ensure that the electrical topologies of all the subsystems were in fact isolated.

The process was ultimately very successful. Figure 4.3 shows a before and after comparison of RFI contamination between the two lasers. The beams from each laser were sent directly to a photodector which was digitized and cross-correlated, and after 12 hours of integration nearly all of the cross-correlation between the two lasers is eliminated. Similar results were obtained for the signal photodetectors and all the way through the DAQ signal chain.

Another important point is that the clocks in the separate digitizers are phase locked to GPS, with synchronization better than 10ns and relative phase drift of $< 90^\circ$ at 25MHz, meaning that the DAQ is indeed stable enough to measure correlated power at MHz fre-

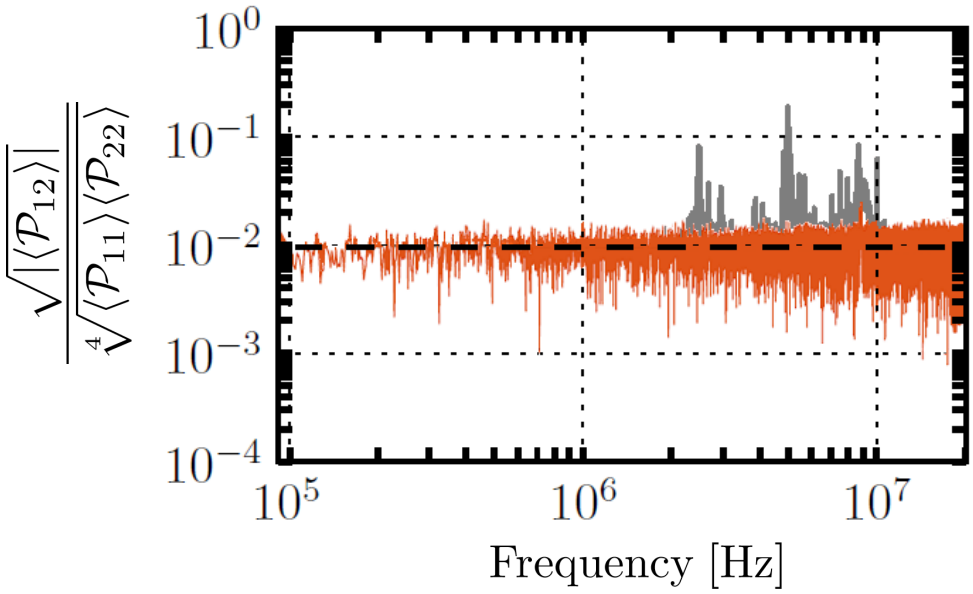

Figure 4.3: Comparison of RFI contamination between the two lasers before and after an extensive campaign to eliminate cross-correlations. After 12 hours of integration, nearly all of the cross-correlation between the two lasers is eliminated (red), compared to before (grey). The y-axis is in units of amplitude coherence, which is the amplitude spectral density of the cross-correlation normalized by each auto-spectrum, meaning that a value of 1 is interpreted as perfect correlation between the two lasers. Figure generated by J. Richardson.

quencies. An example of observing highly-correlated noise lines was shown by the grey trace in Figure 4.3, for the lasers prior to RFI shielding.

4.6 Mechanical and Acoustic Noise

Mechanical and acoustic noise sources are relevant to interferometer control up to frequencies as high as ∼100kHz or so, where the opportunity exists for causing instabilities in the DARM ($\lesssim$ 1kHz) and CARM ($\lesssim$ 100kHz) control loops. These low frequency mechanical noise sources are the largest and most difficult to deal with noise sources which cause fluctuations in L below $\sim$ 1MHz, and they have rapidly increasing amplitude toward lower frequencies.

Isolating the core optics (BS, PRM, EMs) from seismic and vibrational disturbances is the most critical. The core optics are all mounted on top of a passive seismic isolation

system consisting of viton ball springs and heavy steel plates, which damp seismic vibrations above $\sim 10Hz$, pictured in figure 4.4. The end mirrors in the North are mounted on similar isolation stages. The end mirrors in the East were not mounted on isolation stages, as it was empirically determined that isolation at the vertex and North was sufficient. The vacuum system in which the isolation stages sit is bolted directly to the concrete floor of the tunnel. No elaborate suspension systems are needed to isolate the optics, because our signal band is in the MHz frequency range, where seismic and other vibrational noise sources are negligible. We only require enough vibration isolation to hold the interferometer at a stable lock point, as described in section 3.7.2. This is one great advantage that this smaller / higher frequency system has over the larger interferometers such as LIGO and VIRGO.

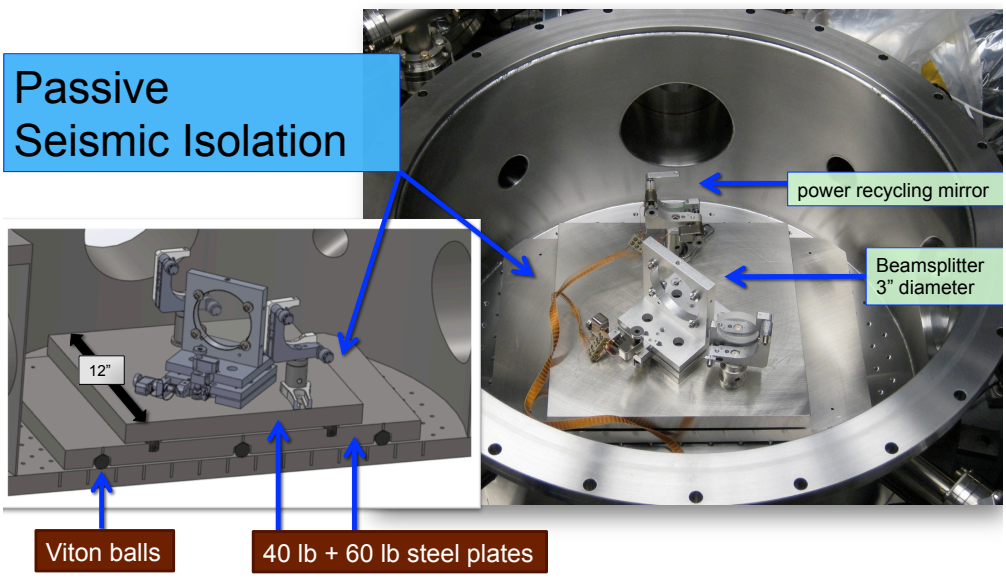

Figure 4.4: Passive seismic isolation for the beasmplitter and power-recycling mirror in the central vacuum service vessel.

Early studies showed that the vibrational noise of the wall on which the periscope mirrors are mounted is sufficiently small as to not induce too much alignment jitter on the beam, and it has since been found during operations that the wall and periscope mount mechanical vibrations are of negligible magnitude.

The beam path along the periscope is in air at ambient pressure, but it is enclosed with

aluminum pipe to shield from air currents, which can induce phase noise on the beam, as well as modulations to the alignment of the beam with respect to the interferometer. Although not ideal, this scheme has proven to be sufficient for high quality operations. A possible future upgrade could be to evacuate the air in the periscope pipe, however this would only be a convenience for the times when injection alignment is particularly non-stationary. It has been found, though, that we can indeed operate with this setup, and produce high quality science data.

CHAPTER 5

END-TO-END CALIBRATION

The direct end-to-end calibration of the power recycled interferometer described here starts with the output voltage spectrum on the AS-port signal photodetectors in $\mathrm{V}/\sqrt{\mathrm{Hz}}$ as digitized in the high frequency DAQ, and converts that to units of DARM sensitivity in $\mathrm{m}/\sqrt{\mathrm{Hz}}$. This is done by directly driving the end mirror PZTs in DARM at a known magnitude at low frequency ($\sim$1kHz), so that the line is visible on the AS-port control photodetector, and then propagating that signal to high frequency on the signal photodetectors.

As mentioned in section 3.9, the photocurrent of the signal photodetectors is high-pass filtered at 200kHz in order to avoid saturating the transimpedance amplifier with the very large DC photocurrent and the large low frequency intensity modulations induced by seismic noise. The exclusion of the low frequency signal by the high-pass filtering stage then significantly complicates the interferometer calibration procedure, where the low frequency calibration signal must be sensed with a separate low frequency photodetector and then transferred to the high frequency output of the signal detector. The calibration line is present during power recycled operation, and it's absolute magnitude in units of meters of DARM motion is precisely measured in the Michelson configuration before and/or after a data run. A separate amplitude modulated signal is used to measure the relative gain between control and signal photodetectors, in order to transfer the calibration to the signal band in the MHz frequency range.

The DARM degree of freedom is defined as the difference in length of the two interferometer arms:

$$\Delta X_{\mathrm{DARM}} \equiv \mathrm{L_x} - \mathrm{L_y} \tag{5.1}$$

At high frequencies, above the influence of the control loops and the cavity pole, the frequency response from DARM motion of the end mirrors to intensity out the AS-port is flat, except at integer multiples of the FSR where the response has very narrow nulls with half width at half maximum (HWHM) given by the cavity pole. This differs from the frequency response of beamsplitter motion to AS-port intensity, which has a series of much broader nulls at integer multiples of *half* the FSR [10]. In this way, the calibration here is directly applicable to the strain sensitivity to gravitational waves.

In the following discussion each term of the calibration equation carries with it subscripts and superscripts denoting the measurement configuration pertaining to that term, with notation defined in Table 5.1.

sub/super script	Description
c, s	AS-port photodetector used: **c**ontrol or **s**ignal
PR, M	interferometer configuration: Power Recycled or Michelson
closed, open	DARM control loop state: locked or not locked
HF, LF	frequency range: High (∼1MHz) or Low (∼1kHz)
X,V	quantity: DARM displacement (meters) or signal (Volts)

Table 5.1: Notation for terms in the end-to-end calibration equation

The calibration involves the determination of the Volts/meter conversion term $\mathrm{dV}^{\mathrm{s,PR,HF}}_{\mathrm{closed}}/dX$ in the relation

$$\mathrm{ASD}^{\mathrm{s,PR,HF}}_{\mathrm{m}/\sqrt{\mathrm{Hz}}} = \mathrm{ASD}^{\mathrm{s,PR,HF}}_{V/\sqrt{\mathrm{Hz}}} \cdot \frac{1}{\mathrm{dV}^{\mathrm{s,PR,HF}}_{\mathrm{closed}}/dX} \tag{5.2}$$

where the left hand side is the high frequency [HF ∼1MHz] power recycled [PR] closed loop [closed] DARM sensitivity in $\mathrm{m}/\sqrt{\mathrm{Hz}}$ of a signal photodetector [s]. Repeated application of the chain rule allows the conversion term $\mathrm{dV}^{\mathrm{s,PR,HF}}_{\mathrm{closed}}/dX$ to be expanded into a product of 7 terms which can be measured individually:

$$\frac{dV^{\mathrm{s,PR,HF}}_{\mathrm{closed}}}{dX} = \underbrace{\overset{\mathrm{s\to c}}{\frac{dV^{\mathrm{s,PR,HF}}_{\mathrm{closed}}}{dV^{\mathrm{c,PR,HF}}_{\mathrm{closed}}}}}_{\frac{dV^s}{dV^c}} \cdot \underbrace{\overset{\mathrm{closed\to open}}{\frac{dV^{\mathrm{c,PR,HF}}_{\mathrm{closed}}}{dV^{\mathrm{c,PR,HF}}_{\mathrm{open}}}}}_{\frac{1}{|1-G^{\mathrm{PR}}(f_{\mathrm{HF}})|}} \cdot \underbrace{\overset{\mathrm{HF\to LF}}{\frac{dV^{\mathrm{c,PR,HF}}_{\mathrm{open}}}{dV^{\mathrm{c,PR,LF}}_{\mathrm{open}}}}}_{\substack{\text{Control PD}\\ \text{gain linearity}\\ \text{from High Freq}\\ \text{to Low Freq}}} \cdot \underbrace{\overset{\mathrm{open\to closed}}{\frac{dV^{\mathrm{c,PR,LF}}_{\mathrm{open}}}{dV^{\mathrm{c,PR,LF}}_{\mathrm{closed}}}}}_{|1-G^{\mathrm{PR}}|} \cdot$$

$$\cdot \underbrace{\overset{\mathrm{PR\to M}}{\frac{dV^{\mathrm{c,PR,LF}}_{\mathrm{closed}}}{dV^{\mathrm{c,M,LF}}_{\mathrm{closed}}}}}_{\frac{V^{\mathrm{c,PR}}_{\mathrm{cal}}}{V^{\mathrm{c,M}}_{\mathrm{cal}}}} \cdot \underbrace{\overset{\mathrm{closed\to open}}{\frac{dV^{\mathrm{c,M,LF}}_{\mathrm{closed}}}{dV^{\mathrm{c,M,LF}}_{\mathrm{open}}}}}_{\frac{1}{|1-G^{\mathrm{M}}|}} \cdot \underbrace{\overset{\mathrm{V\to X}}{\frac{\mathrm{dV}^{\mathrm{c,M,LF}}_{\mathrm{open}}}{\mathrm{dX}}}}_{A_{\mathrm{fringe}}\frac{2\pi}{\lambda}} \tag{5.3}$$

The blue expressions under each term in equation 5.3 indicate the experimentally measured quantities. The red expressions above are short hand indicating the quantities that change between numerator and denominator, with arrows following the logical flow of the calibration scheme. The last term in equation 5.3 shows that the calibration is ultimately referenced to the laser's wavelength λ measured in the Michelson configuration.

We also note that derivative terms involving the open and closed DARM control loop state are measures of the complex-valued loop gain $G(f) = |G(f)|e^{i\theta(f)}$

$$\frac{dV_{\mathrm{closed}}}{dV_{\mathrm{open}}} = \frac{1}{|1 - G(f)|}. \tag{5.4}$$

There are two immediate simplifications of Equation 5.3: first, the power recycled DARM loop gain magnitude at high frequency, $|G^{\mathrm{PR}}(f_{\mathrm{HF}})|$, is effectively zero because the unity gain frequency (UGF) is typically only ∼450Hz, and above the UGF the loop gain falls off roughly as $1/f$. Consequently, at high frequency (∼ 600kHz, where the calibration is transferred to the signal photodetector), Equation 5.4 shows that the calibration term $\frac{dV^{\mathrm{c,PR,HF}}_{\mathrm{closed}}}{dV^{\mathrm{c,PR,HF}}_{\mathrm{open}}} = 1$ to within 0.1%.

Second, the gain of the control photodetector from ∼1kHz to ∼600kHz (where the cali-

bration is transferred to the signal PD) is assumed in this work to be constant (discussion / justification in section 5.1.3).

Combining equations 5.2, 5.3 then gives an expression to plug the measurement results into for the final calibration:

$$\mathrm{ASD}^{\mathrm{s,PR,HF}}_{\mathrm{m}/\sqrt{\mathrm{Hz}}} = \mathrm{ASD}^{\mathrm{s,PR,HF}}_{V/\sqrt{\mathrm{Hz}}} \cdot \frac{dV^c}{dV^s} \cdot \frac{V^{\mathrm{c,M}}_{\mathrm{cal,\ closed}} \left|1 - G^{\mathrm{M}}(f_{\mathrm{cal}})\right|}{V^{\mathrm{c,PR}}_{\mathrm{cal,\ closed}} \left|1 - G^{\mathrm{PR}}(f_{\mathrm{cal}})\right|} \cdot \frac{\lambda}{2\pi A_{\mathrm{fringe}}} \tag{5.5}$$

Section 5.1 discusses the detailed measurements of each of the terms in equation 5.5 for the T interferometer, with the final results summarized in section 5.1.4. Calibration of the L interferometer followed the same scheme but with an extra step of performing a full set of calibration measurements after the science data was recorded, and transferring the calibration to the science data set. In that process for the L interferometer, two additional calibration lines were added to test systematics and reliability. The details of the L interferometer calibration are discussed further in section 5.2.

5.1 Measurements For the Calibration

A brief summary of the scheme used to measure the individual terms in equation 5.5 is given in Table 5.2.

5.1.1 Measurements in Michelson Mode

The Michelson configuration was used to precisely measure the absolute magnitude of the calibration line in meters of DARM motion. Once this is known, the magnitude of the same line appearing in the control photodetector in power-recycled mode can be inferred using the DARM loop gain of the power recycled lock.

The voltage output of the AS-port control photodetector is proportional to the optical

Configuration	Quantity Measured	Measurement Type	Measurement Instrument
Michelson	$\mathrm{V}^{\mathrm{c,M}}_{\mathrm{cal,closed}}$ $G^{\mathrm{M}}(f_{\mathrm{cal}})$ A_{fringe}	Spectrum DARM loop TF Timeseries	Slow DAQ
PR Mich (during data run)	$\mathrm{V}^{\mathrm{c,PR}}_{\mathrm{cal,closed}}$ $G^{\mathrm{PR}}(f_{\mathrm{cal}})$ $\mathrm{ASD}^{\mathrm{s,PR,HF}}_{V/\sqrt{\mathrm{Hz}}}$	Spectrum DARM loop TF Spectrum	Slow DAQ Slow DAQ Fast DAQ
PR Mich (anytime)	$\frac{dV^c}{dV^s}$	TF	HP4396A Analyzer

Table 5.2: Summary of the calibration measurement scheme.

power out the AS-port, and in the Michelson can be expressed in terms of DARM motion X as:

$$\mathrm{V}^{\mathrm{c,M}}_{\mathrm{open}} = A_{\mathrm{fringe}} \sin^2(kX) + \delta_{\mathrm{CD}} \tag{5.6}$$

where $k = 2\pi/\lambda$, δ_{CD} is the contrast defect for the Michelson, and the subscript 'open' emphasizes this is the open loop response.

The Michelson was locked at "half fringe", meaning the argument of the sine in equation 5.6 was locked at $kX = \pi/4$. The slope of $\mathrm{V}^{\mathrm{c,M}}_{\mathrm{open}}$ at the lock point then gives the conversion from Volts to meters:

$$\left.\frac{\mathrm{dV}^{\mathrm{c,M}}_{\mathrm{open}}}{\mathrm{d}X}\right|_{kX=\frac{\pi}{4}} = 2A_{\mathrm{fringe}} k \sin(kX)\cos(kX)\big|_{kX=\frac{\pi}{4}} = A_{\mathrm{fringe}} \frac{2\pi}{\lambda} \left[\frac{\mathrm{Volts}}{\mathrm{meter}}\right] \tag{5.7}$$

The remaining sections describe the details of the measurements in Michelson mode. A complete set of measurements in Michelson mode was performed twice (re-aligning and locking the interferometer before each measurement) to assess the repeatability, and they agreed to 1%.

5.1.1.1 Temporary ASPD for better SNR

For the Holometer interferometers, operating in Michelson mode means the power recycling mirror (PRM) is misaligned so that beams returning from the end mirrors and reflecting off the PRM are dumped into the baffles of the arms so that no resonant cavity is formed. Consequently, the operating power of the Michelson is reduced by the PRM's transmissivity of 10^{-3}, and there is very little light incident on the control photodetector on the AS-port ($\sim 10^{-6}$W at half fringe).

A useful interpretation of equation 5.5 is that the three Michelson terms

$$V^{\mathrm{c,M}}_{\mathrm{cal,\ closed}} \cdot \left|1 - G^{\mathrm{M}}(f_{\mathrm{cal}})\right| \cdot \frac{\lambda}{2\pi A_{\mathrm{fringe}}} \tag{5.8}$$

together give the open loop magnitude of the calibration line in meters of DARM motion. In other words, this number is independent of the DARM control loop used, and importantly, independent of the photodetector used to make the measurement. Exploiting this to optimize the SNR of the measurement, a temporary photodetector was installed on the AS-port in a location with $\sim 200\times$ more optical gain. The measurement setup is shown in figure 3.4.

An auxiliary photodetector ("$\mathrm{PD_{AUX}}$" in Figure 3.4) placed directly before the shutter to signal detectors was chosen for the measurement because of its increased gain and better SNR compared to the DC channel of the NF1811 signal detectors which are on the same optical path. An f=38.1mm lens before the $\mathrm{PD_{AUX}}$ focused the beam on the diode.

The full DARM spectrum during the measurements is shown in figure 5.1. Figure 5.2 shows the SNR of the calibration line above background noise was 26 dB.

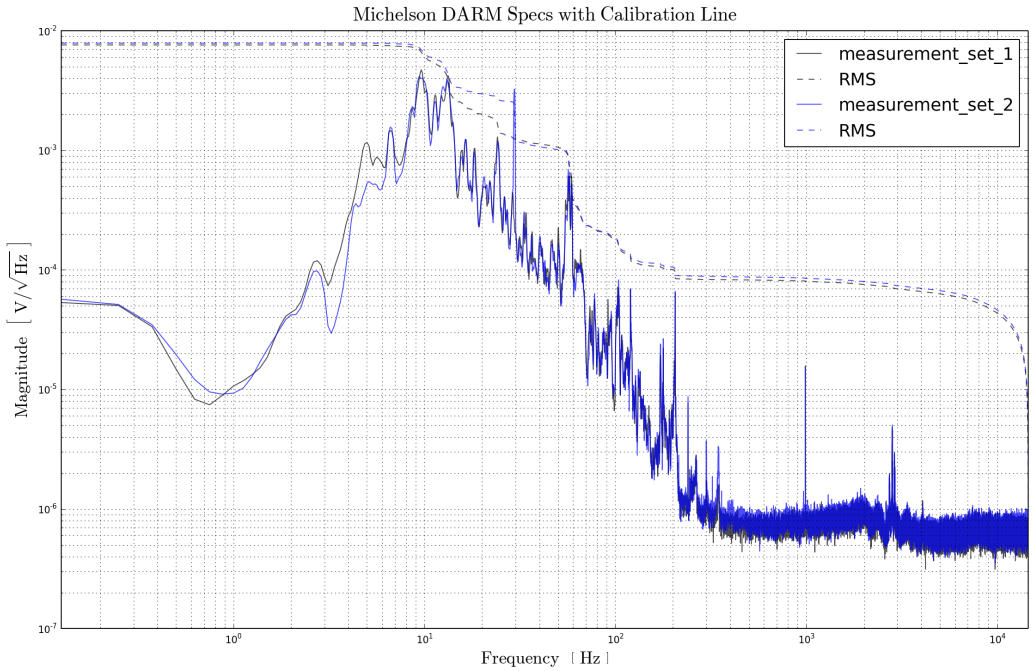

Figure 5.1: Michelson DARM spectrum measured on the conditioning filter output with calibration line visible for the two measurement sets performed. Details of the $f_{cal} = 987$Hz calibration line are in figure 5.2. Some minor differences in the low frequency spectrum are visible where seismic noise dominates the RMS– eg a line at 29Hz from a pump on site is known to come and go– however the calibration peak is comfortably above the dominant seismic contributions to DARM noise, and it is constant to 1% between the two measurement sets (c.f. figure 5.2).

.

5.1.1.2 Conditioned DARM Fringe Amplitude

For convenience, the control photodetector signals were measured after digitization and after the "COND" (for Conditioning) filter module in the digital control software, which had a DC offset that subtracted the term δ_{CD} in Equation 5.6 and gain such that the unlocked Michelson fringes go between 0V at the dark fringe and 1V at the bright fringe. This has the effect of setting $A_{\mathrm{fringe}} \sim 1$ in Equation 5.5. Tuning the gain and DC offset of the conditioning filter stage was done by applying a 2Hz sine wave drive to the DARM degree of freedom of the end mirrors, and adjusting the gain and offsets while observing the timeseries

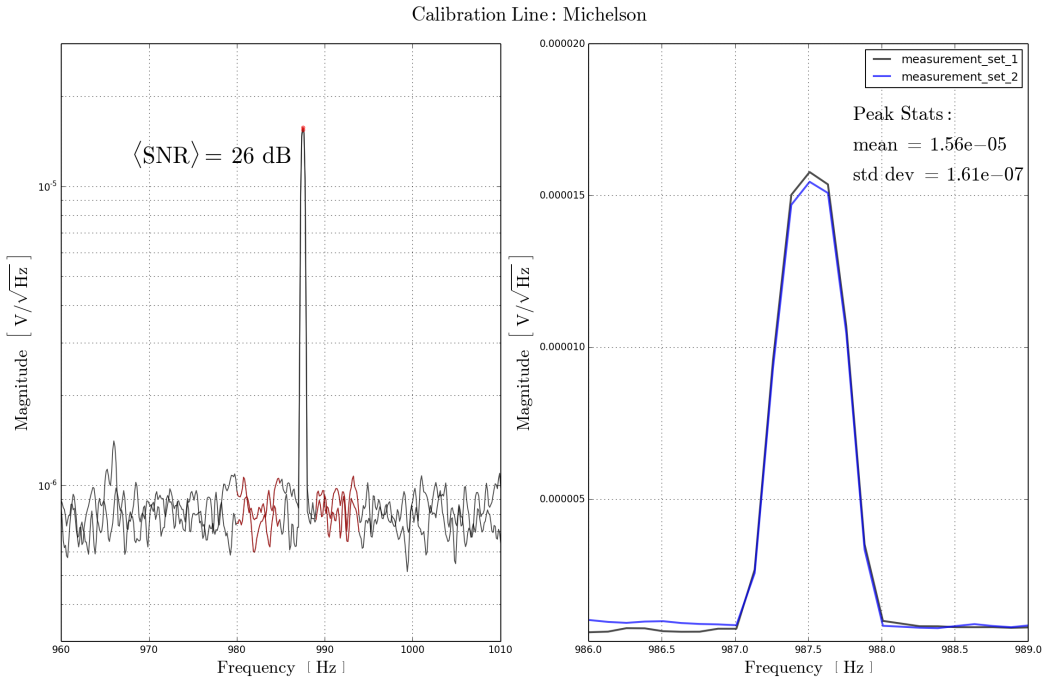

Figure 5.2: Calibration lines in the Michelson DARM spectrum measured on the conditioning filter output for the two measurement sets performed. Left panel: the mean SNR of the peak above the mean background noise level for the two measurements was 26 dB. The red dots are the peak values and the red lines are the regions of the background noise used to compute the SNR as well as the contribution of the background noise to the standard deviation of the measured peak values. The background contributed less than 0.1% to the total standard deviation of the measured peak and so is ignored. Right panel: the peak values in the two measurement sets agreed to 1%, showing excellent reproducibility. The full DARM spectrum during the measurements is shown in figure 5.1

of the conditioned output. The result of the tuning is shown in figure 5.3, which shows the error associated with $A_{\text{fringe}} \sim 1$ is less than 0.5%.

$\mathrm{V}^{\mathrm{c,M}}$ could be renamed to $\mathrm{V}^{\mathrm{COND,M}}$, but this has no bearing on the results so the former is used for simplicity.

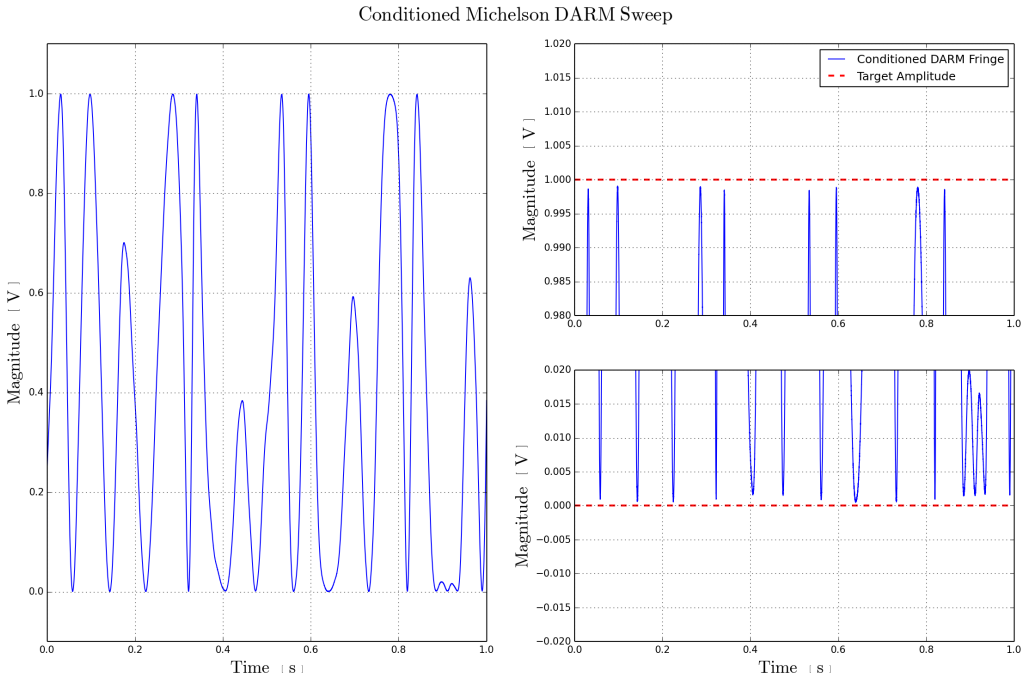

Figure 5.3: Timeseries output of the tuned conditioning filter stage during a Michelson DARM sweep, showing the error associated with $A_{\text{fringe}} \sim 1$ in Equation 5.5 is less than 0.5%. A 2Hz sine wave drive was applied to the end mirror PZTs with amplitude large enough to sweep DARM through several fringes within one drive period. The tuning proceeds in two steps: first the interferometer alignment is optimized by minimizing the dark fringe amplitude (which simultaneously maximizes the bright fringe), ensuring maximum overlap of the electric fields returning from each arm when they interfere at the beamsplitter. second the conditioning filter stage DC offset and gain are adjusted to make the fringe min and max go between 0-1V, respectively. The two right panels are zoomed into the fringe extrema.

5.1.1.3 Calibration Line Magnitude

With the Michelson locked at half fringe, the loop-suppressed (ie closed loop) magnitude $\mathrm{V}^{\mathrm{c,M}}_{\mathrm{cal,closed}}$ of the $f_{\mathrm{cal}} = 987\mathrm{Hz}$ calibration line was measured by recording the amplitude spectral density ASD (in $\mathrm{V}/\sqrt{\mathrm{Hz}}$ units) of the conditioned signal and converting to Vrms units by integrating over the width of the calibration line with the equivalent noise bandwidth (ENBW):

$$\mathrm{V}^{\mathrm{c,M}}_{\mathrm{cal,closed}} = \sqrt{\int_{f_1}^{f_2} |\mathrm{ASD}|^2 \cdot \mathrm{ENBW}} \tag{5.9}$$

The measured peak values in the two measurement sets agreed to 1%. Results are shown in figures 5.1 and 5.2, giving $\mathrm{V}^{\mathrm{c,M}}_{\mathrm{cal,closed}} = (1.07 \pm 0.01) \times 10^{-5}\mathrm{V}_{\mathrm{rms}}$. Figure 5.16 in section 5.2.1 shows the results for all 3 calibration lines used in the L interferometer calibration while power recycling (c.f. section 5.2).

5.1.1.4 DARM loop gain

The DARM open loop gain in single-pass Michelson operation $G^M(f)$ was measured by summing in a broadband white noise excitation with the digital control system. The out-of-loop (ie open loop) magnitude of the calibration line $\mathrm{V}^{\mathrm{c,M}}_{\mathrm{cal,open}}$ was then computed using the measurement of the loop gain at the calibration line frequency $G^{\mathrm{M}}(f_{\mathrm{cal}})$:

$$\mathrm{V}^{\mathrm{c,M}}_{\mathrm{cal,}\mathbf{open}} = V^{\mathrm{c,M}}_{\mathrm{cal,}\ \mathbf{closed}} \left|1 - G^{\mathrm{M}}(f_{\mathrm{cal}})\right| \tag{5.10}$$

where the right-hand side is the numerator in the term 2nd from the right in equation 5.5. Measurements and analysis with descriptions are in figures 5.4, 5.5, 5.6. The results for the magnitude and phase of the loop gain at f_{cal} are $|G^{\mathrm{M}}(f_{\mathrm{cal}})| = 0.33510 \pm (5 \times 10^{-5})$ [V/V], and $\theta^M(f_{\mathrm{cal}}) = 57 \pm 1$[degrees].

The coherence in the Michelson TF at f_{cal} (and for most of the measurement bandwidth) was very nearly 1, and so the random error (c.f. equation B.1) was already less than 1%, basically good enough. However the fitting analysis used in the power recycling case (section 5.1.2.2) was applied in the Michelson case because the tools were already in place– see the power recycled TF measurement for details and a better example of the benefit of the fit

analysis.

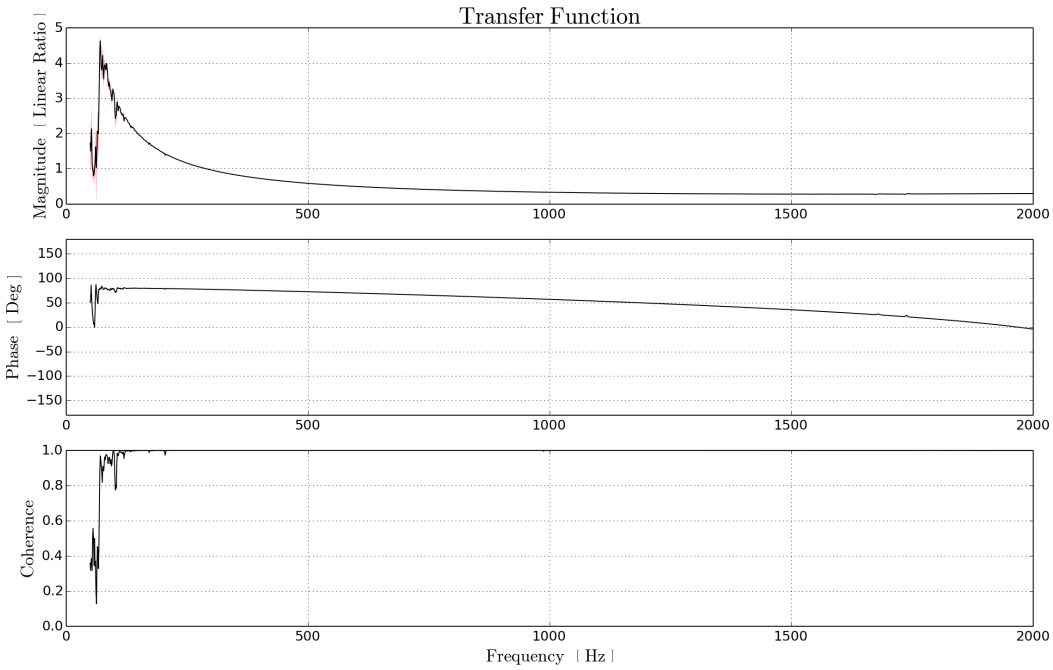

Figure 5.4: Michelson DARM loop transfer function measurement used for the determination of the loop gain $G^{\mathrm{M}}(f_{cal})$. See figure 5.11 for a more detailed description in the case of power recycling.

5.1.2 Measurements in Power-Recycled Mode

As with the Michelson measurements, the closed loop magnitude of the calibration line in power recycled mode was measured in the control photodetector by injecting the line during data runs, using the same amplitude drive summed into the end mirror PZTs at the same point in the DARM loop as the Michelson measurements. The power recycled DARM loop gain was also measured for the calibration. The configuration for power recycled operation is shown in Figure 5.8

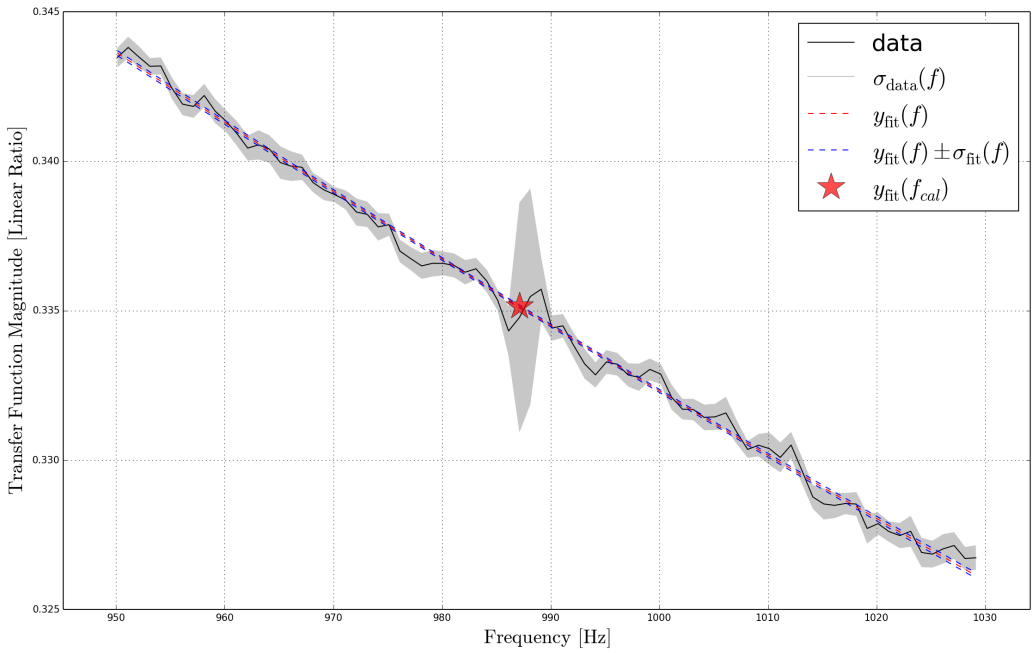

Figure 5.5: Fit to the Michelson DARM loop transfer function data in figure 5.4. see figure 5.12 for a more detailed description in the case of power recycling, and also for a better example of the benefit of the fitting method.

5.1.2.1 Calibration Line Magnitude

The same methods as section 5.1.1.3 were used in power recycled mode. Results are shown in figures 5.9 and 5.10.

The right panel in figure 5.10 shows that the power recycled operating point was reproducible and stable to 4% across the 7 data runs (labeled: DAQ runs 00156 through 00162).

The peak magnitude used for the calibration is the average of the 7 data runs: $\mathrm{V}^{\mathrm{c,PR}}_{\mathrm{cal,closed}} = (4.36 \pm 0.18) \times 10^{-3}\mathrm{V}_{\mathrm{rms}}$.

5.1.2.2 DARM loop gain

The same methods as section 5.1.1.4 were used in power recycled mode. Measurements and analysis with descriptions are in figures 5.11, 5.12, 5.13, and 5.14.

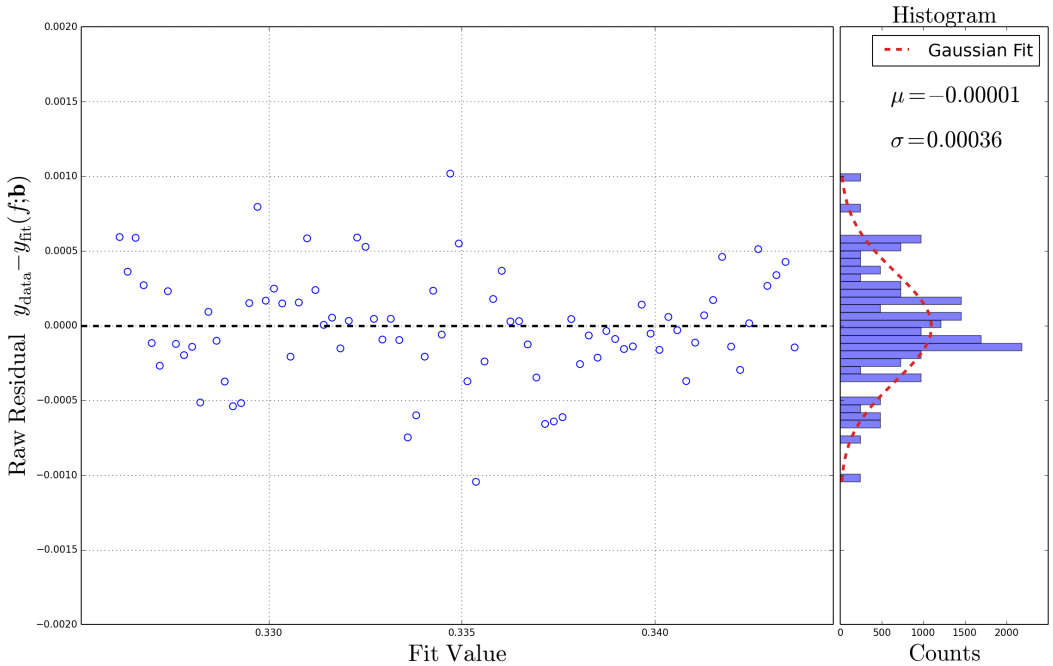

Figure 5.6: Michelson TF raw residuals for the fit in figure 5.5. See figure 5.13 for a detailed description in the case of power recycling, and also for a better example of the benefit of the fitting method.

The result for the magnitude of the loop gain at f_{cal} is $|G^{PR}(f_{\text{cal}})| = 0.3007 \pm 0.0018$. The transfer function phase at the calibration line frequency was measured to be $\theta^{PR}(f_{cal}) = -24 \pm 12$[degrees], where the standard deviation in phase is given by Equation (9.91) in [6]. The phase error contributed less than 1% to the total calibration error, so an additional fit analysis was not performed.

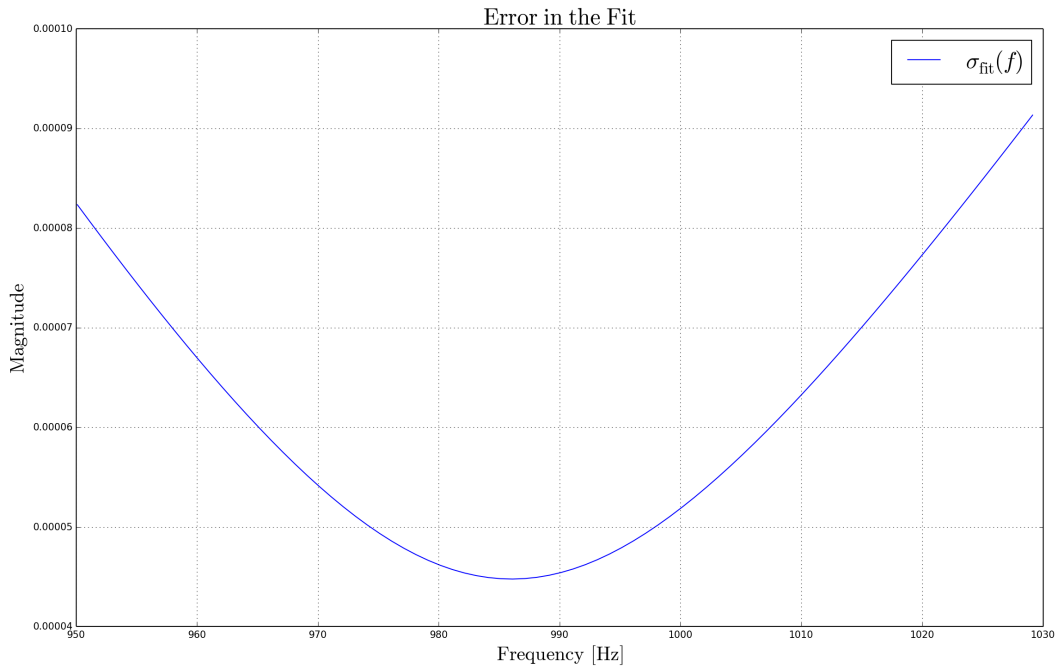

Figure 5.7: Michelson transfer function, error in the fit. See 5.14 for details.

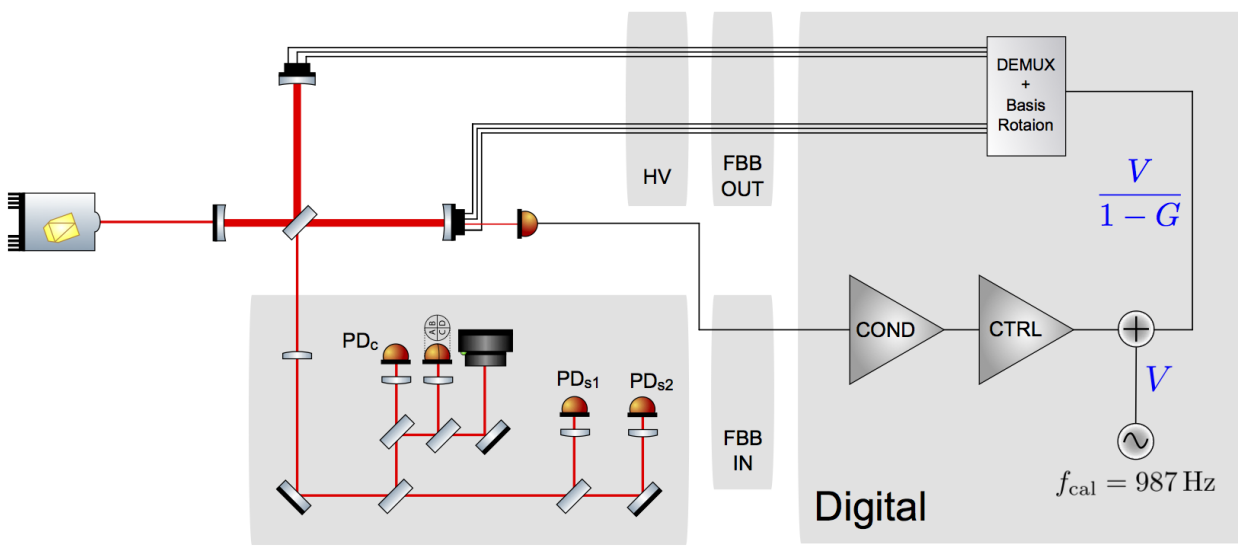

Figure 5.8: Configuration for measurements in power recycled mode. The calibration line is summed into the same junction as in single-pass Michelson mode in Figure 3.4. A quadrant photodetector for alignment and CCD camera are on the AS-port down stream of $\mathrm{PD_c}$.

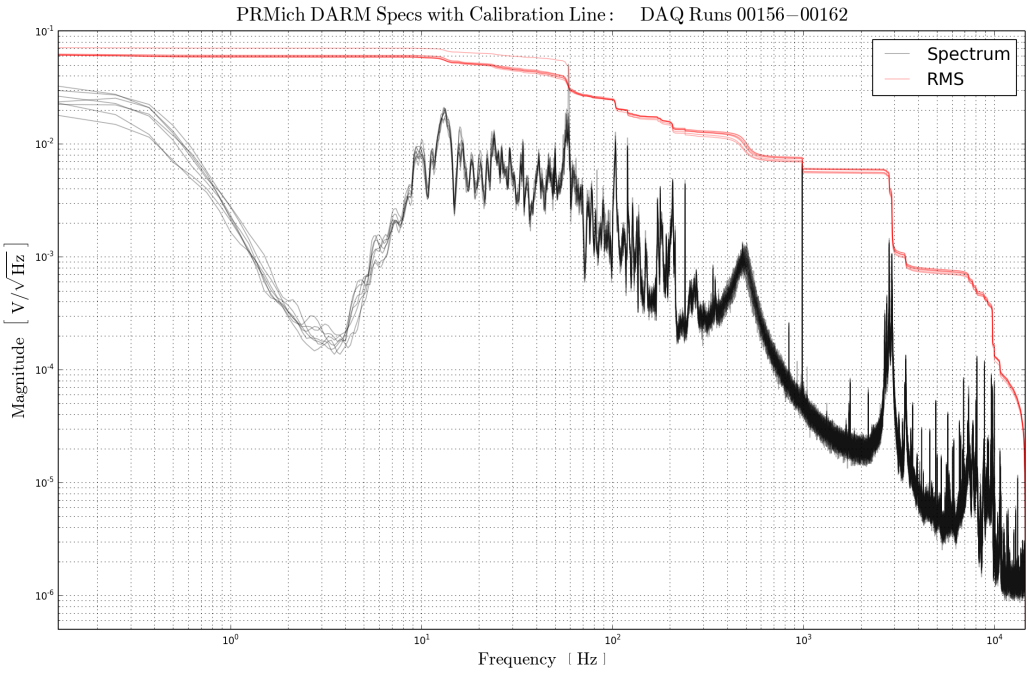

Figure 5.9: Superimposed power recycled DARM spectra for the 7 data runs (DAQ runs 00156-00162), measured at the control photodetector output immediately after digitization. Details of the f_{cal} = 987Hz calibration line are in figure 5.10, which also shows that the operating point was reproducible and stable to within 4% across the runs. The peaks just below 2kHz are end mirror piezo resonances. They had been acting up at this time, but extra finely tuned notch filters tamed them to this manageable level, and they did not interfere with the calibration results.

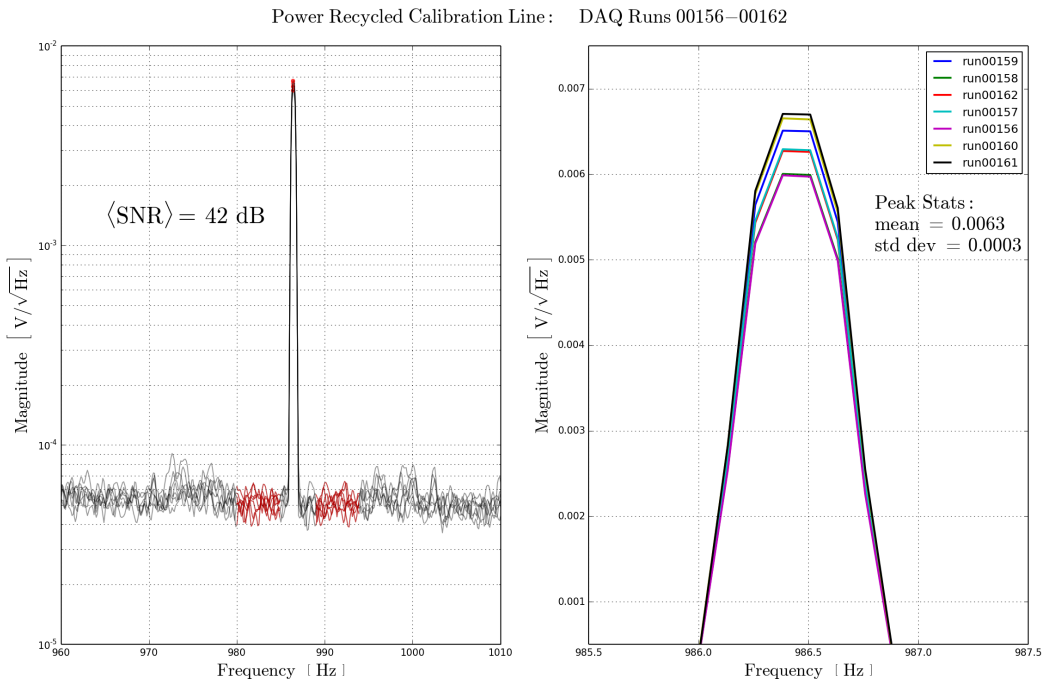

Figure 5.10: Calibration line in the power recycled DARM spectra for DAQ runs 00156-00162, measured at the control photodetector output immediately after digitization. Left panel: the 7 data sets superimposed, showing the mean SNR of the peak above the mean background noise level was 42 dB. The red dots are the peak values and the red lines are the regions of the background noise used to compute the SNR as well as the contribution of the background noise to the standard deviation of the measured peak values. The background contributed less than 0.1% to the total standard deviation of the measured peak and so is ignored. Right panel: shows that the power recycled operating point was reproducible and stable to within 4% across DAQ runs 00156-00162. The full low frequency DARM spectrum for all data runs is in figure 5.9.

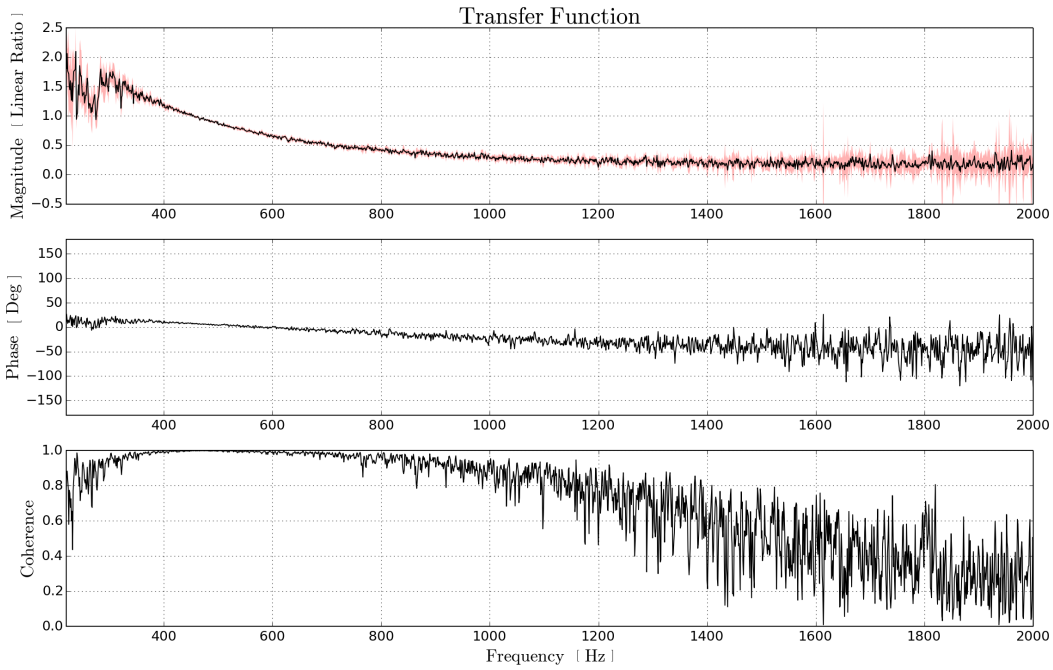

Figure 5.11: Power recycled Michelson DARM loop transfer function measurement used for the determination of the loop gain $G^{\mathrm{PR}}(f_{cal})$. The red shaded region encloses the measured magnitude (black) $\pm\,\sigma_{\mathrm{r}}(f)$, where $\sigma_{\mathrm{r}}(f)$ is the standard deviation from random error due to non-perfect coherence and limited number of averages. The functional form of $\sigma_{\mathrm{r}}(f)$ is given in equation B.1. Figures 5.12 and 5.13 show a fit and analysis to further reduce the error in the magnitude $|G^{\mathrm{PR}}(f_{cal})|$ below that given by $\sigma_{\mathrm{r}}(f_{cal})$ in the single frequency bin for f_{cal}. $n_{\mathrm{avg}} = 5$ averages were used. This TF was measured immediately following DAQ data runs 00156-00162 with the same operating point.

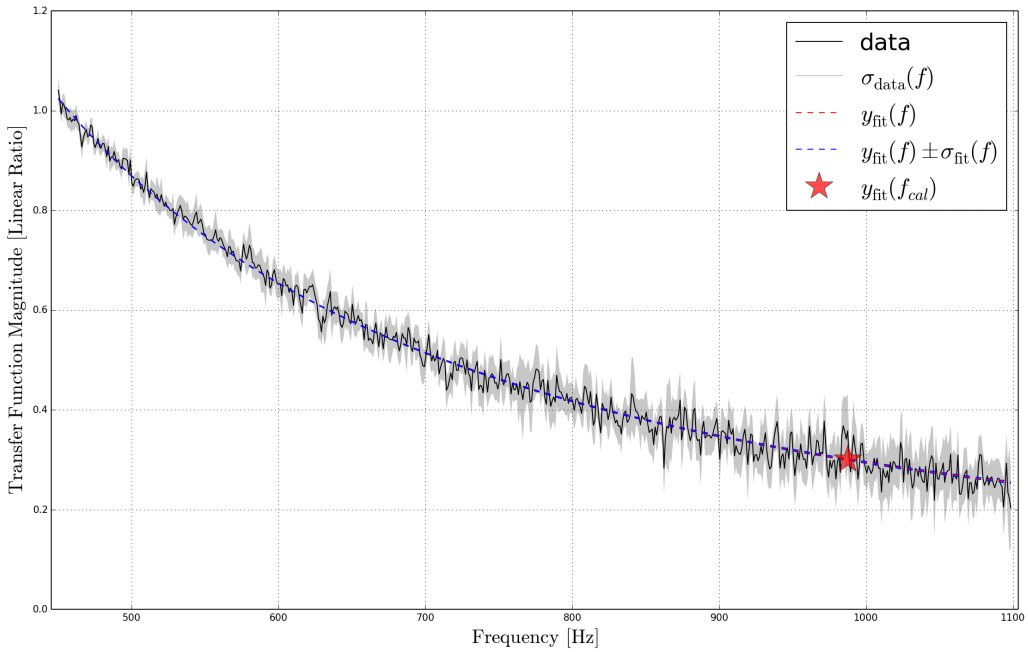

Figure 5.12: Fit to the power recycled Michelson DARM loop transfer function data in figure 5.11 to reduce the errors in the measured loop gain magnitude $|G^{\rm PR}(f_{cal})|$. The grey shaded region encloses the measured magnitude (black) $\pm\sigma_{\rm data}(f) \equiv \sigma_{\rm r}(f)$, where $\sigma_{\rm r}(f)$ is the standard deviation from random error due to non-perfect coherence and limited number of averages. The functional form of $\sigma_{\rm r}(f)$ is given in equation B.1. $n_{\rm avg} = 5$ averages were used. The motivation for the fit was to further reduce the error in the magnitude $|G^{\rm PR}(f_{cal})|$ below that given by $\sigma_{\rm r}(f_{cal})$ in the single frequency bin for f_{cal}. The standard error (σ/μ) was reduced from 20% without the fit (ie using $\sigma_{\rm data}(f_{cal})$) to 0.6% using the fit, by leveraging the extra information contained in the rest of the data, where $|G(f)|$ is expected to be a simple function of frequency. Note: the error was reduced by a factor of *roughly* $1/\sqrt{N}$ for $N = 650$ data points used in the fit. A non-linear least squares fit to the function $y_{\rm fit}(f) = b_1 f^{b_2}$ was used, with best fit parameters $b_1 = 1.41 \times 10^4$, $b_2 = -1.56$. The fit residuals are in figure 5.13. A linear fit to the log of the data produced similar results.

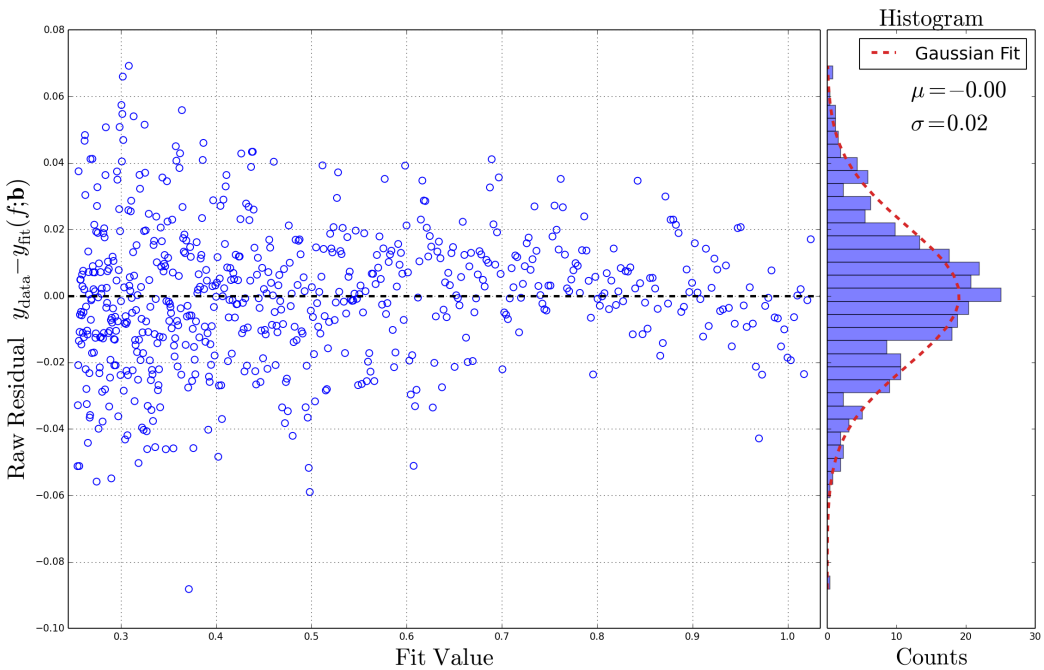

Figure 5.13: Power recycled Michelson transfer function raw residuals for the fit in figure 5.12. The heteroscedasticity (variable errors) in the raw residuals plot, seen as an increased deviation from 0 at data points corresponding to higher frequencies (left of the plot), is largely due to the drop in coherence at higher frequencies, which produces an increase in random errors of the transfer function estimate at higher frequencies [c.f. equation B.1]. The Studentized Residuals are one way of correcting for this by normalizing the residuals with an appropriate function of the variance of residuals and the diagonals of the hat matrix, providing a means to interpret the residuals for different data points on more equal footing, and to check for outliers that significantly effect the fit. However, the effect here is small, and visual inspection of the data shows there do not appear to be any significant outliers, so this is not expected to contribute significantly to the final fit result. In other words this is taken to be a sufficient measure for the goodness of fit.

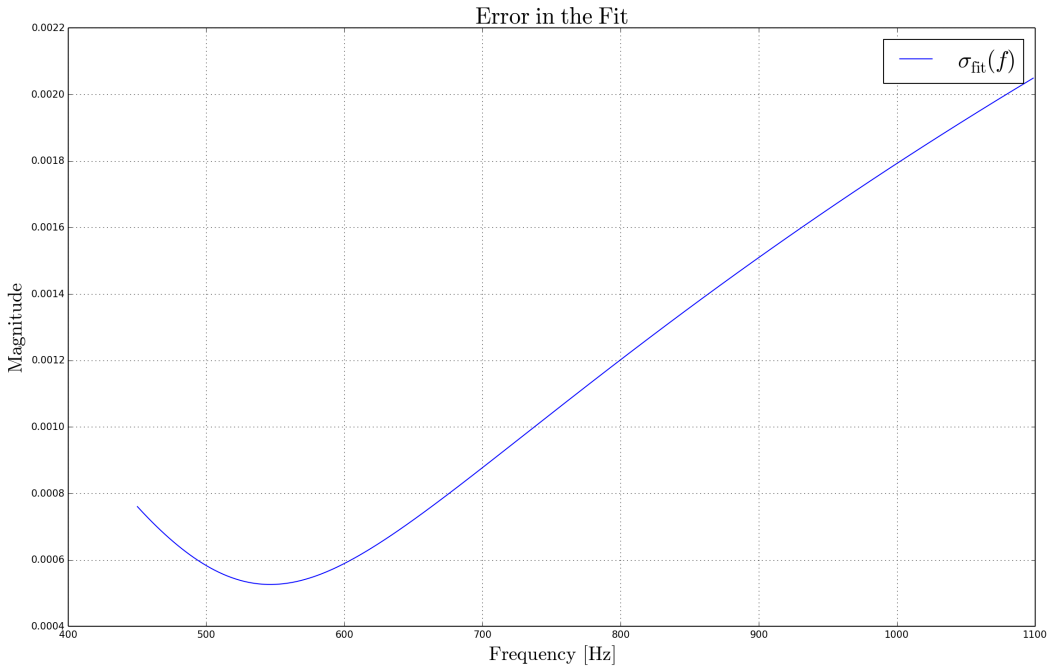

Figure 5.14: Power recycled Michelson error in the transfer function fit. The error in the fit is quadratic, and one can optimize where the minimum error occurs by choosing the frequency bandwidth for the analysis. The single-pass Michelson case was not in need of this. However in the power recycled case, an effectively two parameter optimization was used, in that the lower frequency range already had small errors due to higher coherence, and so including those data points reduced the overall error (at the expense of moving the minimum of the error parabola away from the 987Hz calibration line frequency). This is a generally useful technique for optimizing where the errors are minimized in a fit.

5.1.3 Transfer of Calibration to Signal Photodetectors

The configuration of the control ("PD_c") and signal ("PD_s") photodetectors on the AS-port is in Figure 5.8. The relative gain of these detectors was measured so that the calibration could be transferred to the high frequency DARM spectrum in the fast DAQ data. Measurement results are in Figure 5.15.

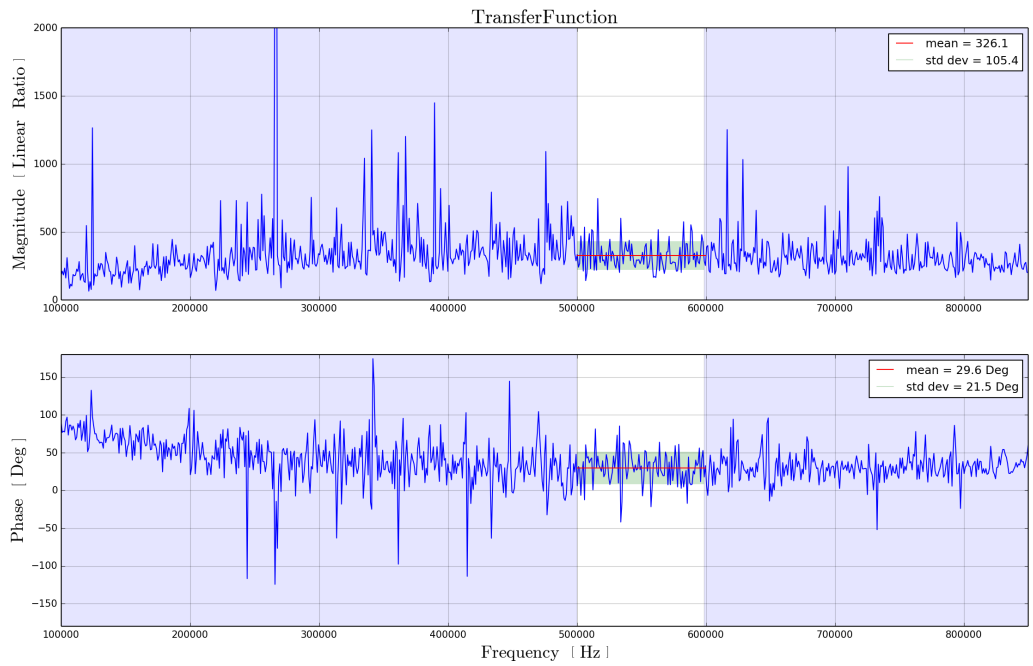

Figure 5.15: Relative gain measurement for the two photodetectors PD_c and PD_s, in linear units. Blue shaded regions are ignored for the measurement. The mean is 326, sample standard deviation (highlighted in green) is 105.4, and the standard error of the mean is $105.4/\sqrt{N} = 10.2$ for $N = 106$ frequency bins used. NOTE: this is with PD_c measured into 50 ohms, and this measurement is of the ratio PD_s/PD_c, so this result must be divided by 2 for the factor used in the calibration equation. Also note that the analysis bandwidth was chosen somewhat arbitrarily by eye, however, increasing this range to, e.g., 700kHz has negligible effect on the result.

Any amplitude modulated 1064nm source originating from a point on the AS-port optical path *before* the beam splits to the PD_c and PD_s detectors would suffice for the measurement, provided there are negligible losses along either optical path to the detectors (which would

bias the result), and there is sufficient SNR of the AM peak in each detector.

The power recycled Michelson was locked at moderate power (outside the volcano-shaped response in the blue trace of Figure 2.3, for optimal stability), and the AM line at the AS-port used for the TF measurement was generated by driving the auxiliary EOM (phase modulator) on the laser table ("EOM1" in Figures 3.2 and 3.3), and the Schnupp asymmetry converted the phase modulation sidebands (PM) to amplitude modulation (AM) sidebands at the AS-port. The HP4396A analyzer then mixed down the PD signals at the drive frequency to measure the relative TF. The advantage of this method is that it uses the existing in-situ setup and is very quick to measure before or after a data run. It is worth noting, however, that one must take care to avoid measurements at frequencies where higher order modes are resonant in the optical cavity, because optical mixing of the carrier with the higher order modes can result in extra amplitude modulation on the photodetectors, significantly skewing the transfer function results.

The transfer function was directly measured over a $\sim$ 100kHz bandwidth between 500kHz-600kHz (a larger BW was actually measured, but 100kHz was used for analysis). Below this band, down to the 987Hz calibration line frequency, it is assumed that the gain of PD_c is flat, and this appears to be a reasonable assumption. The measured TF agreed very well with the expected result based on the optics and photodetector properties, where the PD_c specs (Thorlabs PDA20CS) state a -3dB bandwidth of 4MHz, and a gain of 4.75×10^3V/A$\pm$2%. Also, the photocurrent from the diode is directly fed into the transimpedance amplifier, with no intervening capacitors or filtering components. In addition, the overall DARM sensitivity calibration reported in this work agreed with the shot noise limited sensitivity expectation based on the measured power on the beamsplitter to within 5% (see Section 5.3).

A direct measurement of the gain linearity of PD_c from $\sim$1kHz-1MHz was attempted using shot noise from an incandescent bulb, however the required DC light level to see the shot noise above detector noise at high frequency saturated the output. This is because the

(dark) noise floor of the PDA20CS rises by $\sim \times 10$ at high frequency, to the point where the SNR becomes <1. A TF between PD_c and an unmodified NF1811 (which has response to lower frequency than the modified versions) using an AM modulated laser source is probably a sufficient method to gauge the gain linearity of PD_c, given that the NF1811 gain linearity is known to be fairly flat, and so is a good reference.

The 500kHz-600kHz bandwidth for the measurement was chosen because the TF magnitude was fairly flat over this range, and this band is free from higher order mode cavity resonances. Below this range the measured TF magnitude decreased toward lower frequencies, as expected from the 200kHz high-pass response of the NF1811's AC channel. At ∼1MHz (which is a relative frequency offset from the resonant TEM_{00} carrier) the Gouy phase advance of the first order transverse mode makes up for the frequency offset and the mode becomes resonant in the cavity. The small (but non-negligible) coupling from the TEM_{00} EOM-generated phase sidebands into the first order spatial mode saturated the HP4396A analyzer inputs. Above ∼1MHz the noise floor of the PDA20CS is rather large and so the SNR of the measurement was too poor.

The quantity measured and plotted in figure 5.15 is $\frac{dV^s}{dV^c}$ measured into 50 ohms by the HP4396A analyzer, and the result there is 326±10[V/V]. The value reported in table 5.3 for $\frac{dV^s}{dV^c}$ for the full DARM calibration, which is the value entered into equation 5.5, is this divided by 2 because the PD_c DARM spectrum is measured into a high impedance.

5.1.3.1 Agreement with Expected Result

The expected result for the TF measured into the 50 ohm inputs of the HP4396A analyzer (the quantity plotted in figure 5.15), given the reflectivity and gain specs for the optics and photodetectors, respectively, is 333[V/V]. This is in excellent agreement with the measured value of 326±10 [V/V].

Quantity	$\mu \pm \sigma$	σ/μ
$\mathrm{V}^{\mathrm{c,M}}_{\mathrm{cal,closed}}$	$(1.07 \pm 0.01) \times 10^{-5}[\mathrm{V_{rms}}]$	1%
$\lvert G^{\mathrm{M}}(f_{\mathrm{cal}})\rvert$	$0.33510 \pm (5 \times 10^{-5})$ [V/V]	0.01%
$\theta^{\mathrm{M}}(f_{\mathrm{cal}})$	57 ± 1[degrees]	–
A_{fringe}	$1.000 \pm < 0.005$	$< 0.5\%$
$\mathrm{V}^{\mathrm{c,PR}}_{\mathrm{cal,closed}}$	$(4.36 \pm 0.18) \times 10^{-3}[\mathrm{V_{rms}}]$	4.1%
$\lvert G^{\mathrm{PR}}(f_{\mathrm{cal}})\rvert$	0.3007 ± 0.0018 [V/V]	0.6%
$\theta^{\mathrm{PR}}(f_{\mathrm{cal}})$	-24 ± 12[degrees]	–
$\frac{dV^{\mathrm{s}}}{dV^{\mathrm{c}}}$	163 ± 5 [V/V]	3.1%

Table 5.3: Summary of measurement results for the terms in Equation 5.11. Although the phase error in the power recycled Michelson transfer function is 12 degrees, it contributes $\sim 0.1\%$ to the total calibration error. Note that the standard error σ/μ is not a useful quantify for phase.

5.1.4 Summary of Measurement Results

Table 5.3 gives a summary of the calibration measurements with errors. The final result for the [meters/Volt] conversion term in the calibration equation 5.2 using the results in table 5.3 is:

$$\begin{aligned}\frac{1}{\mathrm{dV}^{\mathrm{s,PR,HF}}_{\mathrm{closed}}/dX} &= \frac{dV^c}{dV^s} \cdot \frac{V^{\mathrm{c,M}}_{\mathrm{cal,\ closed}}\left|1 - G^{\mathrm{M}}(f_{\mathrm{cal}})\right|}{V^{\mathrm{c,PR}}_{\mathrm{cal,\ closed}}\left|1 - G^{\mathrm{PR}}(f_{\mathrm{cal}})\right|} \cdot \frac{\lambda}{2\pi A_{\mathrm{fringe}}}\ [\mathrm{m/V}] \\ &= (3.01 \pm 0.21) \times 10^{-12}\,[\mathrm{m/V}] \end{aligned} \tag{5.11}$$

which is $\pm 7\%$ for the T interferometer.

5.2 L Interferometer Calibration

5.2.1 Transfer of Calibration Between Measurement Suites

Calibration of the L interferometer followed the same scheme as the T interferometer outlined in the previous sections, but with an extra step of performing a full set of calibration measurements after the science data was recorded, and transferring the calibration to the

science data. In that process for the L interferometer, two additional calibration lines were added to test systematics and reliability, as shown in Figure 5.16. This section details the L interferometer calibration.

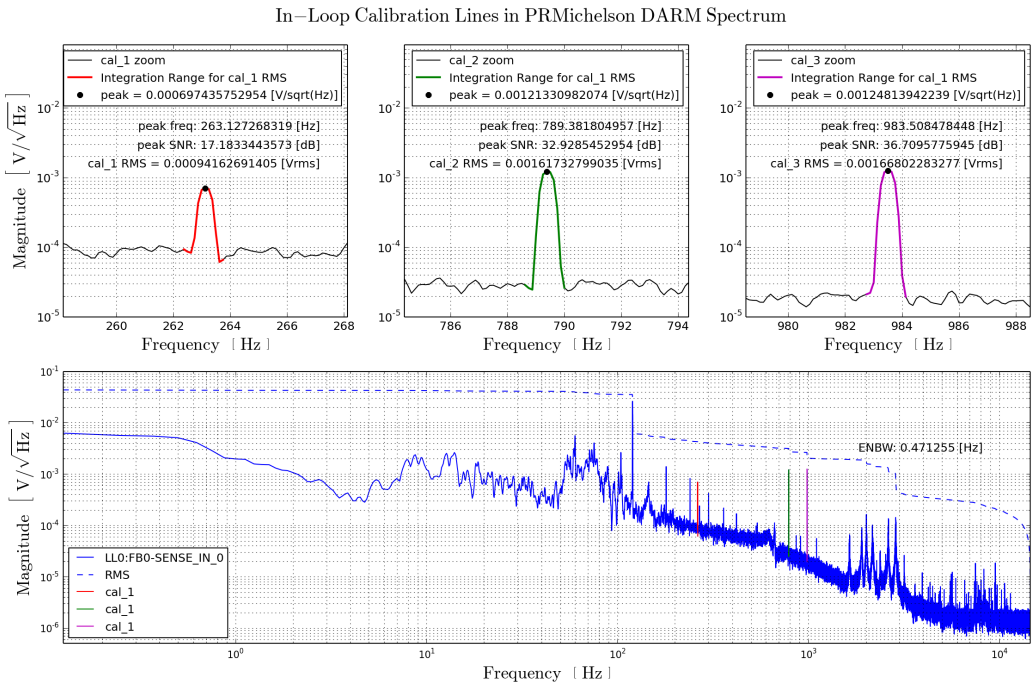

Figure 5.16: Measurement of the 3 calibration lines injected for the L interferometer calibration suite.

For simplicity we refer to a "calibration suite" to mean a set of calibration measurements, together with the high frequency DAQ data recorded in a particular power-recycled state of the interferometer, to which the calibration applies. Altogether, the end product of a calibration suite is a high frequency DARM spectrum calibrated in $\mathrm{m}/\sqrt{\mathrm{Hz}}$ units.

The shot noise limited DARM sensitivity estimate which includes the effects of contrast defect is given in Equation 5.20, and it can be used to transfer the calibration between two suites of measurements I and II:

$$\mathrm{ASD}^{\mathrm{I}}_{m/\sqrt{\mathrm{Hz}}} = \mathrm{ASD}^{\mathrm{I}}_{V/\sqrt{\mathrm{Hz}}} \cdot C^{\mathrm{II}} \cdot \sqrt{\frac{P^{\mathrm{II}}_{\mathrm{BS,eff}}}{P^{\mathrm{I}}_{\mathrm{BS,eff}}}} \cdot \sqrt{\frac{1+\beta^{\mathrm{I}}}{1+\beta^{\mathrm{II}}}} \tag{5.12}$$

where $P_{\mathrm{BS,eff}} \equiv P_{\mathrm{BS}} \cdot \sum_i \eta_i$, $\beta \equiv P_{\mathrm{Junk}}/P_{\mathrm{Fringe}}$ is the ratio of contrast defect light to signal light in the TEM_{00} mode at the AS-port (see section 5.3.1), and C^{II} is the meters/Volt calibration constant for measurement suite II, with

$$C^{\mathrm{I}} = C^{\mathrm{II}} \cdot \sqrt{\frac{P^{\mathrm{II}}_{\mathrm{BS,eff}}}{P^{\mathrm{I}}_{\mathrm{BS,eff}}}} \cdot \sqrt{\frac{1+\beta^{\mathrm{I}}}{1+\beta^{\mathrm{II}}}}. \tag{5.13}$$

Equation 5.12 is strictly true under the assumptions that:

1. The AS-port efficiency terms $\sum_i \eta_i$ are the same between calibration suites,
2. The North transmission optical and electronics chain also remained the same,
3. An estimate for the contrast defect is attainable for each interferometer configuration I and II.

With these requirements satisfied, it is also true that the ratio of effective beamsplitter powers can be simplified to the ratio of voltages on the North transmission photodetector, and this is what was done in practice to transfer the L interferometer calibration to the science data set reported in this work.

β in each set of the calibration suites I and II was estimated to be 1, and the ratio of North transmission voltages was $V^{\mathrm{II}}/V^{\mathrm{I}} = 0.882$, giving a final calibration constant for the L interferometer science data set in this work (suite I) of:

$$C^{\mathrm{I}} = (2.27 \pm 0.18) \times 10^{-12} \left[\frac{\mathrm{m}}{V}\right] \tag{5.14}$$

which is ±8%.

5.2.2 Exclusion of 1 Signal Photodetector in L interferometer Data

Subsequent measurements of one of the signal photodetectors on the L interferometer showed varied and unreliable results, leading to the conclusion that it was ultimately unfit for science data, and so it was excluded from all results in this work. The impact of this is in actuality not all that large, reducing the L interferometer's effective shot noise limited sensitivity by a factor of $\sqrt{2}$.

5.3 Comparison with Shot Noise Limited Sensitivity Estimate from Stored Cavity Power

The shot noise limited sensitivity of the power recycled Michelson in the ideal case of no contrast defect and no losses in the AS-port optics chain is:

$$\mathrm{ASD}_{\mathrm{shot,m}/\sqrt{\mathrm{Hz}}} = \frac{1}{k}\sqrt{\frac{E_\gamma}{P_{\mathrm{BS}}}} = \sqrt{\frac{hc\lambda}{4\pi^2 P_{\mathrm{BS}}}} \tag{5.15}$$

where $k = 2\pi/\lambda$ and E_γ is the energy per photon. Multiplying equation 5.15 by k gives units of radians/$\sqrt{\mathrm{Hz}}$. When losses are considered on the asymmetric port path between the beamsplitter and photodetector, the sensitivity is given by

$$\mathrm{ASD}_{\mathrm{shot},m/\sqrt{\mathrm{Hz}}} = \sqrt{\frac{hc\lambda}{4\pi^2 \cdot P_{\mathrm{BS}} \cdot \sum_i \eta_i}} \tag{5.16}$$

where η_i are optical and electronic efficiencies along the AS-port beam path (i.e. $0 < \eta < 1$, and $\eta = 1$ when there are no losses). For example η_{QE} is the quantum efficiency of the photodetectors.

5.3.1 Contrast Defect

Light exiting the AS-port that is not in the TEM_{00} mode and/or does not interfere between the two arms is dubbed junk light, because it contains no useful DARM phase information. The total AS-port power is the sum of junk and useful fringe light:

$$P_{\mathrm{AS,Total}} = P_{\mathrm{Fringe}} + P_{\mathrm{Junk}} \tag{5.17}$$

and the noise spectral densities add in quadrature:

$$\mathrm{ASD}_{\mathrm{AS,Total}} = \sqrt{(\mathrm{ASD}_{\mathrm{Fringe}})^2 + (\mathrm{ASD}_{\mathrm{Junk}})^2} \tag{5.18}$$

Junk light reduces the overall DARM sensitivity by adding more noise (decreasing the SNR). If, for example, $\mathrm{ASD}_{\mathrm{Junk}} = \mathrm{ASD}_{\mathrm{Fringe}}$, the total AS-port noise $\mathrm{ASD}_{\mathrm{AS,Total}}$ is increased by $\sqrt{2}$ compared to the case with no junk light, and correspondingly the DARM sensitivity is reduced by $\sqrt{2}$.

Letting $\beta \equiv P_{\mathrm{Junk}}/P_{\mathrm{Fringe}}$ we have

$$\mathrm{ASD}_{\mathrm{AS,Total}} = \mathrm{ASD}_{\mathrm{Fringe}}\sqrt{1+\beta}, \tag{5.19}$$

which provides a correction to the shot noise limited DARM sensitivity estimate in Equation 5.16, now including the effects of contrast defect:

$$\mathrm{ASD}_{\mathrm{shot},m/\sqrt{\mathrm{Hz}}} = \sqrt{\frac{hc\lambda}{4\pi^2 \cdot P_{\mathrm{BS}} \cdot \sum_i \eta_i}} \cdot \sqrt{1+\beta}. \tag{5.20}$$

Equation 5.20 shows how the shot noise limited sensitivity scales with the beamsplitter power and various loss terms. The contrast defect for the T interferometer was roughly measured to be ∼50ppm. Estimates from CCD image data of the AS-port beam during lock indicate that the total AS-port power was comprised of approximately equal parts junk and fringe (TEM_{00}) light, meaning $\beta \sim 1$. With the AS-port power split equally onto two detectors, values of $\eta_{\mathrm{QE}} = 0.7$, $\eta_{\mathrm{split}} = 0.5$ (splitting power to two detectors), and P_{BS} =1.92kW give a single detector shot noise limited sensitivity estimate of $\mathrm{ASD}_{\mathrm{shot},m/\sqrt{\mathrm{Hz}}} = 3.99 \times 10^{-18}\mathrm{m}/\sqrt{\mathrm{Hz}}$. Importantly, this agrees with the end-to-end calibration to 5% for a single signal photodetector in the T interferometer.

As a consistency check, P_{BS} was measured to be 1.92kW. A ratio of $P_{\mathrm{Junk}}/P_{\mathrm{BS}} = 50$ppm, and equal parts junk and fringe light would then give

$$
\begin{aligned}
P_{\mathrm{AS,Total}} &= P_{\mathrm{Fringe}} + P_{\mathrm{Junk}} \\
&\sim 2P_{\mathrm{Junk}} \\
&= 2P_{\mathrm{BS}} \cdot \mathrm{CD} \\
&= 2 \cdot 1920\mathrm{watts} \cdot 50\mathrm{ppm} \\
&= 0.192\mathrm{watts}
\end{aligned}
\tag{5.21}
$$

half of which (96mW) is incident on each signal detector. The total AS-port power measured for the data runs was $P_{\mathrm{AS,Total}}$ ∼177mW[1], which is in good agreement with expectation.

1. The control photodector's voltage was directly calibrated to total AS-power with a Thorlabs S310C power meter, and the photodetector voltage was recorded during the data taking runs.

CHAPTER 6

ANALYSIS AND RESULTS

This chapter presents an overview of the data analysis and results. Much of the statistical machinery used in this chapter is developed in Appendix A.

6.1 Data Acquisition and Methodology

As mentioned in section 3.10.2, each of the four signal photodetector channels (two for each interferometer), together with the 4 auxiliary channels for laser intensity monitors and loop antennas, is digitized in the fast DAQ at 100MHz sampling rate. Each 1 second long timeseries data segment from each of the 8 channels is then Fourier transformed, and cross-spectra are computed between all 8 channels in the frequency domain. The FFT sample size used is 65536, resulting in a frequency resolution of 763Hz.

The resulting (real-valued) auto-spectra and (complex-valued) cross-spectra, in power spectral density units (V^2/Hz), are then averaged in the frequency domain for each successive 1 second long batch of data. The cross-coherence is then computed as the square root of Equation (B.2), which normalizes the cross-spectrum by the individual auto-spectra. After all the spectra from all the data segments have been averaged together, the cross-interferometer spectra are then averaged together, giving the final spectrum to be calibrated and used in the final analysis.

The differential arm (DARM) sensitivity calibration in meters/Volt is then applied to the auto- and cross-spectra as described in Chapter 5, where the geometric mean of the two individual T and L interferometer calibration constants is used for the cross-spectrum calibration in meters/$\sqrt{\text{Hz}}$.

6.2 Systematic and Statistical Errors

The dominant source of error in the results presented in this work is systematic error in the overall calibration of the detector response, which is 7% for the T interferometer (c.f. Equation 5.11) and 8% for the L interferometer (c.f. Equation 5.14).

These systematic errors are in turn dominated by the variations in operating point for the two interferometers between the seven individual data runs that were combined to give the total integration time of 1 hour. Each of the seven data runs was terminated because one or both of the interferometers lost lock (due to seismic impulses, for example), and upon reacquiring lock, there were small variations in operating point between data runs, which are quantified by the variability in the measured calibration line magnitude between runs. One possible data analysis procedure could be to weight the data in each run by the relative change in magnitude of the calibration line, however, because the variations are fairly small, a simpler approach is used in this work, whereby the variation in calibration line magnitude contributes to the systematic error in the overall result.

6.3 Test for Correlations

An important consequence of Equation (A.12) is that the ratio of the standard deviation to the mean for the coherence is constant, independent of the number of averages m_{avgs}:

$$\left.\frac{\sqrt{\text{Var}[\text{Coh}]}}{\text{E}[\text{Coh}]}\right|_{c=0} = \sqrt{\frac{4}{\pi} - 1} \sim 0.523 \tag{6.1}$$

This will hold true so long as there is no underlying correlated signal ($c = 0$). Once the number of averages becomes large enough to begin to resolve a correlated signal (if there is one), then terms involving c in Equation (A.8) begin to become important. This can also be seen in the real part of the cross-coherence in Equation (A.7), where the variance integrates

down by m_{avgs} until the mean value c can finally be resolved.

This property of the coherence spectrum was exploited to very clearly expose frequency components with statistically significant correlations. Figure (6.1) shows a sliding window method for computing the ratio in equation (6.1) for a variety of window sizes, to very easily reveal correlations. Each data point in the figure is the result of centering a window of bandwidth ΔB at that frequency, and computing the ratio of the standard deviation to the mean over that bandwidth. The window is then shifted one frequency bin to the right, and the ratio is computed again, and so on. This method can help to expose correlations not so easily detected by eye in the coherence spectrum.

Figure 6.1 shows that there are only two fairly narrow bandwidth correlations (at 1.35MHz and 1.97MHz) over the entire bandwidth from 1.1MHz-11MHz. These same correlations were also present in the cross-coherence spectra between ALL of the signal photodetectors and the large loop antenna (c.f. figures 6.2 and 6.3), meaning that the source of the correlations is(are) electromagnetic in nature, and they can safely be ignored as possible gravitational wave signals. The figure legend lists the window bandwidths used for each trace.

6.4 Differential Arm (DARM) Motion Sensitivity

Figure 6.4 shows the final high frequency DARM sensitivity in units of meters/$\sqrt{\text{Hz}}$ for the combined 1hr of integration time, after applying the full end-to-end calibration described in chapter 5.

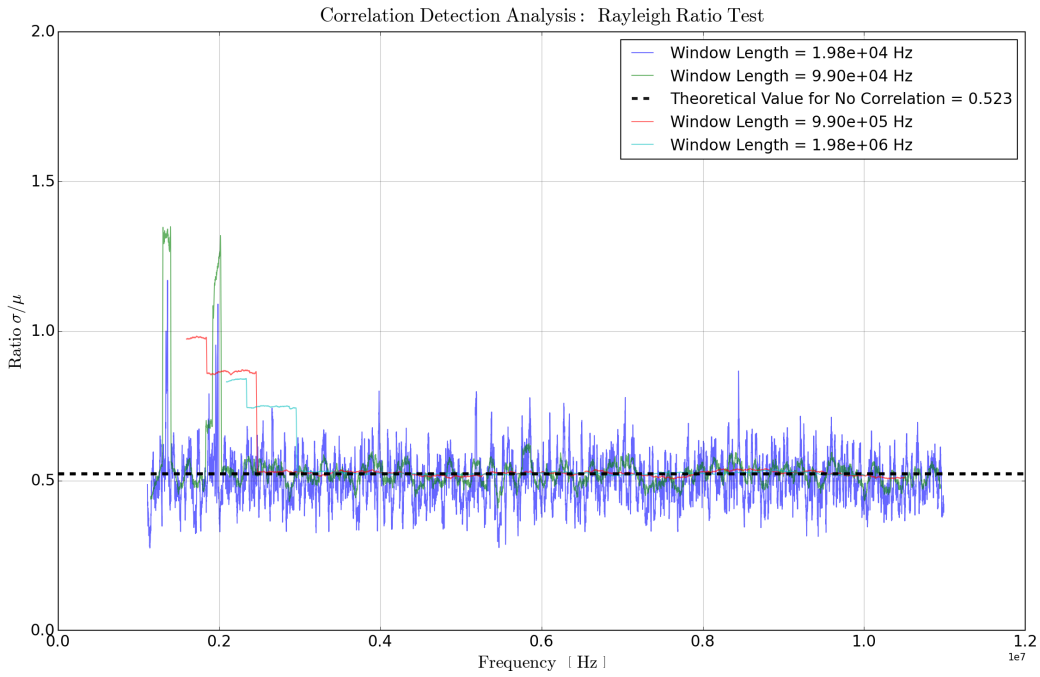

Figure 6.1: The correlation test described in section 6.3, applied to the cross-coherence spectrum between interferometers. The two visible correlations were also present in the cross-coherence spectra between ALL of the signal photodetectors and the large loop antenna, meaning that the source of the correlations is(are) electromagnetic in nature, and they can safely be ignored as possible gravitational wave signals.

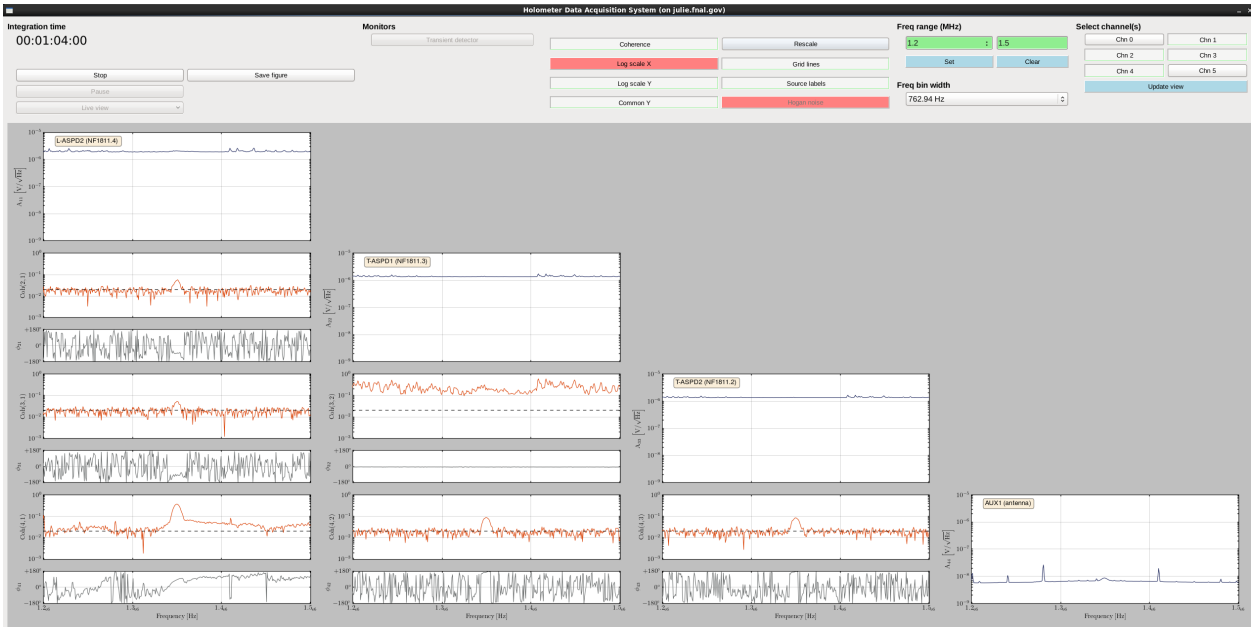

Figure 6.2: Matrix of coherence plots for the three signal photodetectors included in the analysis, and the loop antenna, showing correlation between the signal photodetectors and the loop antenna at 1.35MHz. Plots on the diagonal are the auto-spectra (blue traces), and the off-diagonal plots are the cross-coherences (red is magnitude, grey is phase). The loop antenna auto-spectrum is the bottom right. From these plots, one can see that around 1.35MHz there is correlation between the two interferometers, but there is also correlation with the loop antenna, so these correlations can safely be ignored as not possibly being due to gravitational waves. Details are discussed in section 6.3.

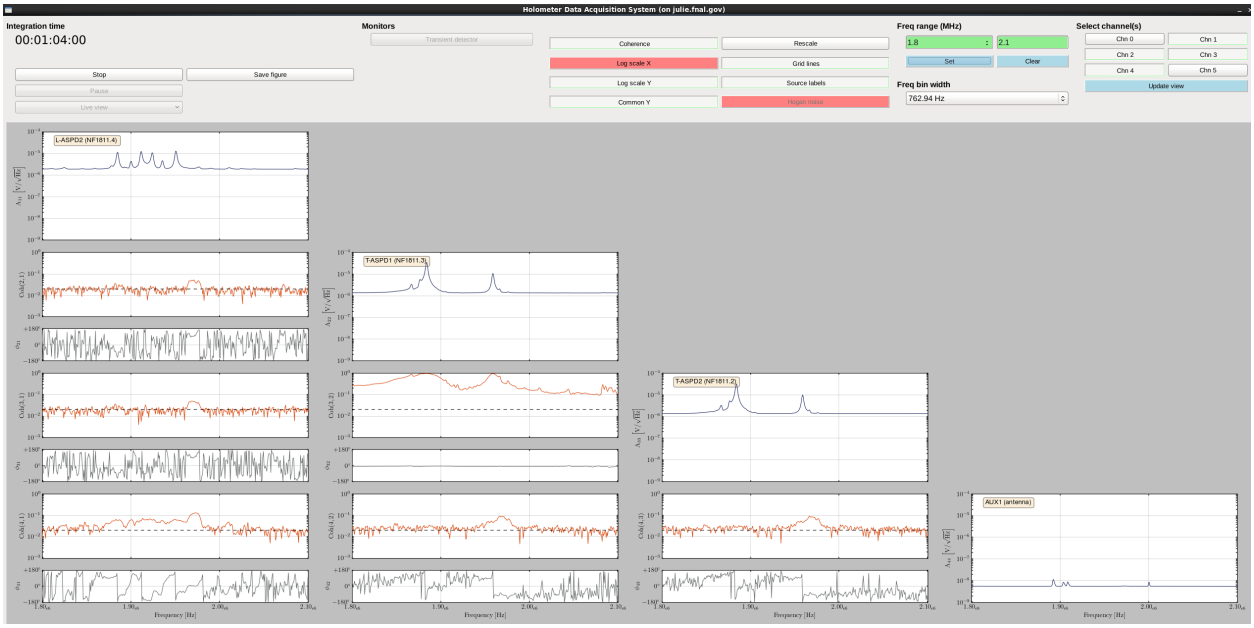

Figure 6.3: The same as figure 6.2 (see for description of plot), but now highlighting a correlation around 1.97MHz, and again showing correlation with the loop antenna.

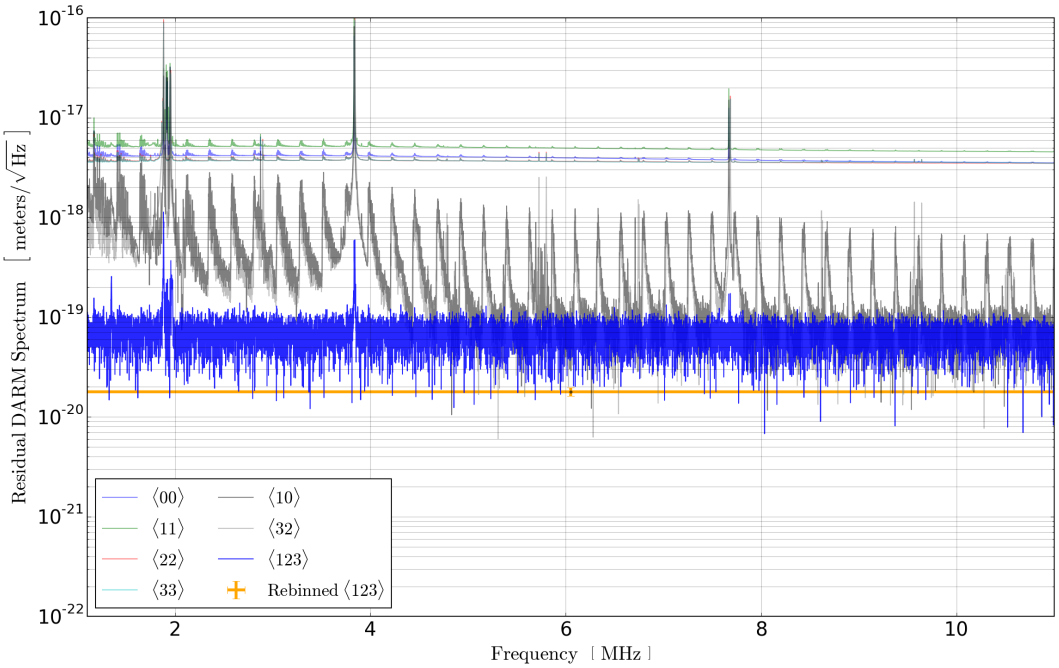

Figure 6.4: High frequency residual DARM spectra, with the direct end-to-end calibration results applied to both interferometers, giving units of meters/$\sqrt{\text{Hz}}$. Traces ⟨00⟩ and ⟨11⟩ are the auto-spectra of the two L interferometer signal photodetectors, and the L-L cross-spectrum is trace ⟨10⟩. Similarly, the T interferometer data is in traces ⟨22⟩, ⟨33⟩, and ⟨32⟩. The two interferometer cross-spectrum is shown in thick blue (trace ⟨123⟩. See section 5.2.2 for why detector "0" was excluded), and its frequency-rebinned value is in orange (all data points over the visible range were averaged into a single bin. The vertical error bar is from the systematic error in the end-to-end calibration).

6.5 Detector Response to Gravitational Waves

In this work, the sensitivity to gravitational waves incident from directly above the apparatus, traveling orthogonal to the interferometer plane, with polarization aligned with the arms (+ polarization) is considered. In this case, a gravitational wave at frequency f_{gw} and amplitude $h(t) = h\exp(i2\pi f_{gw}t)$ causes a differential arm phase change of [21]:

$$\Delta\phi = h(t)\frac{4\pi L}{\lambda}\frac{\sin x}{x}e^{ix} \tag{6.2}$$

where $x \equiv 2\pi f_{gw}L/c$ and $\lambda = 1064$nm is the laser wavelength. Equation (6.2) is then normalized to give a transfer function magnitude which has a DC limit that goes to one, given by:

$$|\Delta\phi_{\text{norm}}| \equiv \frac{\sin \pi x}{\pi x} \tag{6.3}$$

The DARM signal data (blue trace in Figure 6.4) is then divided by Equation (6.3) to give the final data in units of equivalent gravitational wave strain. The result of this process is the dark grey data trace in Figure 6.6. The normalized gravitational wave transfer function in Equation (6.3) is plotted in figure 6.5.

It should be noted that if one were interested in using the data reported here to analyze the sensitivity to gravitational waves incident in another orientation, one would simply have to apply the new gravitational wave transfer function to the DARM signal data in Figure 6.4.

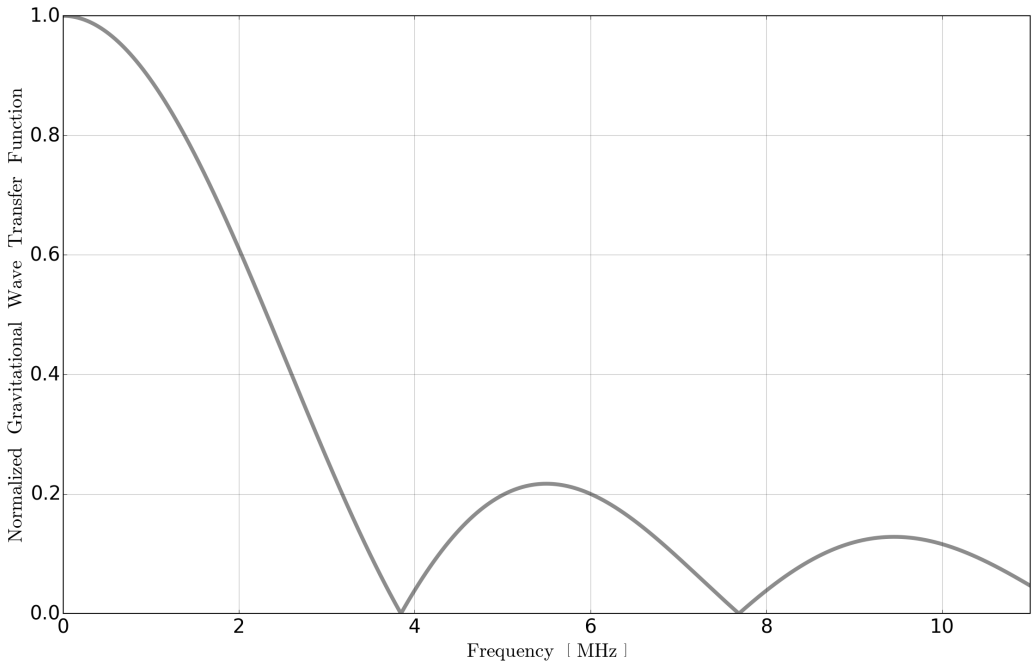

Figure 6.5: Normalized gravitational wave transfer function in Equation (6.3).

6.6 Upper Limits on Gravitational Wave Strain Amplitudes in the 1-11MHz Frequency Range

The general form of the coherence sampling distribution in equation (A.8) was used to generate 95% confidence upper limits (one-sided confidence intervals) for the strain amplitude of possible gravitational waves passing through the detector. The method used to compute the upper limits was the standard Neyman construction for frequentist confidence intervals (c.f. chapter 9 of [11], and the "statistics" review in [19]). The upper limits were computed on the coherence data, and then scaled to physical units by multiplying by the constant factor that normalizes the coherence (which does not affect the statistics). The spectrum was first scaled from coherence to meters/$\sqrt{\text{Hz}}$ using the calibration described in section 5. The data was then converted to equivalent gravitational wave strain by dividing by the arm length as well as the antenna response function.

The upper limits were computed by solving the following equation for the value of the correlated fraction c [1]:

$$\beta = \int_0^{r_{\rm obs}} f_{\rm Coh}(r, c, m_{\rm avgs}) dr \tag{6.4}$$

where $f_{\rm Coh}(r, c, m_{\rm avgs})$ is given in Equation (A.8), and $r_{\rm obs}$ is the measured value of r (i.e. the measured coherence). The probability threshold β was chosen to be $\beta = 0.05$ (corresponding to a $(1-\beta) \times 100\% = 95\%$ upper limit). Equation 6.4 was then numerically solved for c at each data point $r_{\rm obs}$ over the analysis bandwidth, and the results are the magenta trace in figure 6.6. The scientific python ("SciPy") libraries scipy.integrate.quad and scipy.optimize.fsolve were used for numerical integration and root finding, respectively.

As equation (6.4) shows, confidence intervals are a function of the measured data, and the fluctuations in the upper limits (magenta trace in figure 6.6) across frequency bins reflects this fact. Therefore, to help guide the eye, the thick black curve in Figure 6.6 was computed in the following way: the mean value of all the upper limit values across frequency bins was computed in coherence units, and this mean value was then scaled to strain units in the same way as the data was (described above). All of the spectral shaping of the black curve therefore comes from the auto-spectra of the original data, as well as the gravitational wave transfer function. This spectral shaping from the auto-spectra is also present in the data and upper limit traces of figure 6.6, only with far larger variance between frequency bins.

Another way of interpreting the black curve is that in the limit that the experiment were to be repeated an infinite number of times (producing an infinite number of data sets like the one reported here), the average of all the magenta traces from each repeated experiment would converge to something close to the black trace. This is true because the black curve

1. Equation 6.4 here is the same as Equation (9.9) in [11], but translated into the present notation, and with lower limit of integration equal to zero because $r > 0$.

was produced using a large number of samples— the samples were at different frequencies, but in the limit that there truly is no underlying correlation, averaging along the frequency axis is equivalent to averaging the same number of samples measured in a single bin.

The above results are upper limits on fairly narrow band sources of gravitational waves, on the order of the frequency bin width which is 763Hz. The data over the bandwidth 1-11MHz was also averaged together into a single large bin to test for a broadband source of gravitational wave power. The upper limit was computed in coherence units first, as with the narrow band limit, and then the upper limit on broadband gravitational wave strain was computed by using the average of the gravitational wave transfer function over the entire band. The 95% confidence upper limit for broadband gravitational wave power computed in this way is $2.4 \times 10^{-21}\mathrm{Hz}^{-1/2}$.

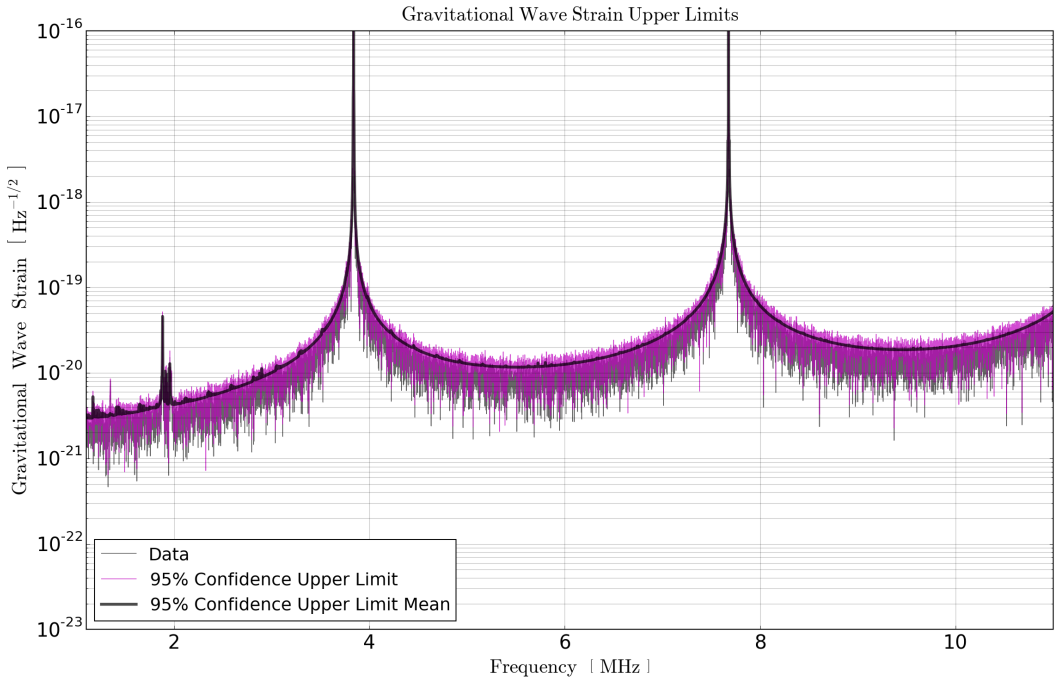

Figure 6.6: 95% confidence level upper limits on the strain amplitude of gravitational waves incident on the apparatus. The results are to be interpreted as the sensitivity to gravitational waves incident from directly above the interferometers, traveling orthogonal to the interferometer plane, with polarization aligned with the arms ("+" polarization). The grey trace is the original data (the blue trace in Figure 6.4) with the gravitational wave antenna sensitivity transfer function applied. The magenta trace is the 95% confidence level upper limit, and the thick black curve is the mean value of the magenta, to better guide the eye (the mean is computed in coherence units before scaling to strain. See section 6.6 for details).

CHAPTER 7

CONCLUSIONS AND FUTURE WORK

In conclusion, the work presented in this thesis places new limits on the strain amplitude of gravitational waves in the 1-11MHz frequency range. By cross-correlating the output of two identical power-recycled Michaelson laser interferometers, an unprecedented level of sensitivity is achieved, which is better than two orders of magnitude below the quantum shot-noise limit in a single interferometer. 95% confidence level upper limits are placed on the strain amplitude of narrow band ($\sim$ 760Hz) gravitational wave sources at the 10^{-21} Hz$^{-1/2}$ level. For gravitational wave power distributed over this frequency range, a broadband upper limit of 2.4×10^{-21}Hz$^{-1/2}$ at 95% confidence level is also obtained

In the near term future, with the techniques developed in this thesis, more data will be taken, for longer integration times, resulting in even further sensitivity to gravitational waves. The improvement in sensitivity scales as the fourth root of the integration time, so for example with only sixteen more hours of data, the present limits can be improved by a factor of two.

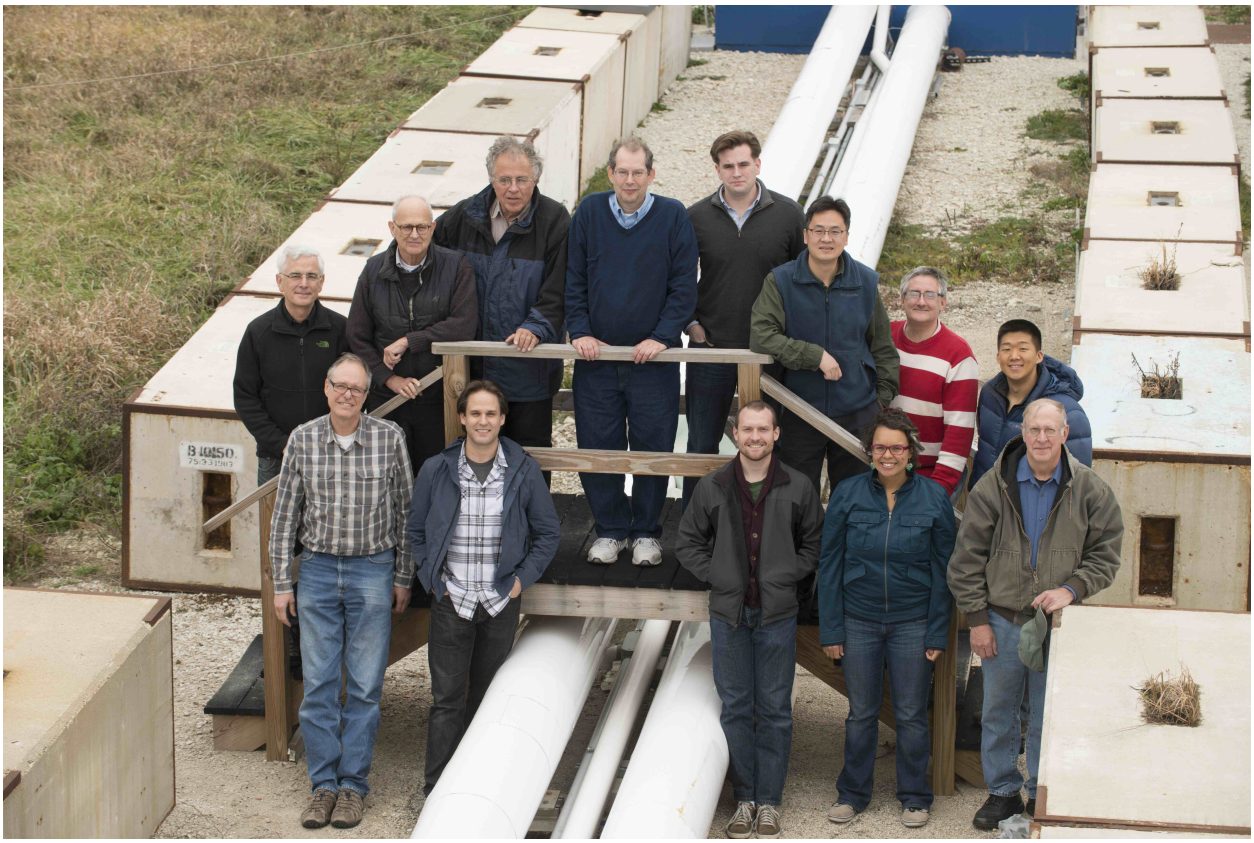

Figure 7.1: The Holometer Team, pictured over the East Holometer arms. From left to right: C. Hogan, S. Meyer, R. Weiss, R. Lanza, D. Gustafson, H. Glass, J. Richardson, L. McCuller, A. Chou, B. Kamai, C. Stoughton, O. Kwon, R. Tomlin

APPENDIX A

THE CROSS-SPECTRUM SAMPLING DISTRIBUTION

A.1 The General Form

The cross-spectrum G_{xy} expressed in Cartesian coordinates has the form (dropping the explicit frequency dependence)

$$G_{xy} = X_1 + iX_2 \tag{A.1}$$

where $X_1 = \mathrm{Re}\left[G_{xy}\right]$, and $X_2 = \mathrm{Im}\left[G_{xy}\right]$. X_1 is also referred to as the "co-spectrum", and X_2 the "quadrature spectrum". In polar coordinates G_{xy} has the form:

$$G_{xy} = Re^{i\theta} \tag{A.2}$$

where the magnitude and phase of the cross-spectrum are related to the co- and quadrature spectra as:

$$\begin{aligned} R &\equiv \left|G_{xy}\right| = \sqrt{X_1^2 + X_2^2}, \\ \theta &\equiv \mathrm{Arg}\left(G_{xy}\right) = \tan^{-1}\frac{X_2}{X_1} \end{aligned} \tag{A.3}$$

In general, X_1 and X_2 are two NON-identically distributed gaussian random variables:

$$
\begin{aligned}
X_1 &\sim \mathcal{N}\left(\mu_1,\, \sigma_1^2\right) \\
X_2 &\sim \mathcal{N}\left(\mu_2,\, \sigma_2^2\right)
\end{aligned}
\tag{A.4}
$$

where it is generally the case that $\mu_1 \neq \mu_2$, and $\sigma_1 \neq \sigma_2$. The fact that X_1 and X_2 can have different means and variances results in the sampling distribution for $R = \sqrt{X_1^2 + X_2^2}$ being rather nontrivial to compute.[1] It can be shown that the sampling distribution for the magnitude of the cross-spectrum R is given by [1]:

$$
\begin{aligned}
f_R(r, \mu_i, \sigma_i) =& \frac{r}{\sigma_1 \sigma_2} \exp\left[-\frac{1}{2}\left(\frac{\mu_1^2}{\sigma_1^2} + \frac{r^2}{2\sigma_1^2} + \frac{r^2}{2\sigma_2^2}\right)\right] \\
&\times \sum_{n=0}^{\infty} \varepsilon_n I_n\left(\frac{r^2}{4}\left(\frac{1}{\sigma_2^2} - \frac{1}{\sigma_1^2}\right)\right) \cdot I_{2n}\left(\frac{r\mu_1}{\sigma_1^2}\right)
\end{aligned}
\tag{A.5}
$$

where I_n are modified Bessel functions of the first kind, $\varepsilon_0 = 1$, and $\varepsilon_n = 2$ for $n > 0$. The Bessel function sum in (A.5) converges rather quickly, and in practice the inclusion of terms up to $n \sim 15$ is more than sufficient for most computations and error requirements. Figure A.1 shows an example of the relatively quick convergence of Bessel function terms.

A.2 Normalization for Coherence Measurements with Averaged Samples

The analysis can be simplified considerably by transforming the cross-spectrum into coherence, by applying the appropriate normalization. Coherence is defined as [6]:

1. For example, if $\mu_1 \neq \mu_2$, but $\sigma_1 = \sigma_2 = 1$, then R would have a noncentral chi distribution. However, we will be concerned principally with the case when both the means and variances are different, which requires a little more work to solve for the distribution of R.

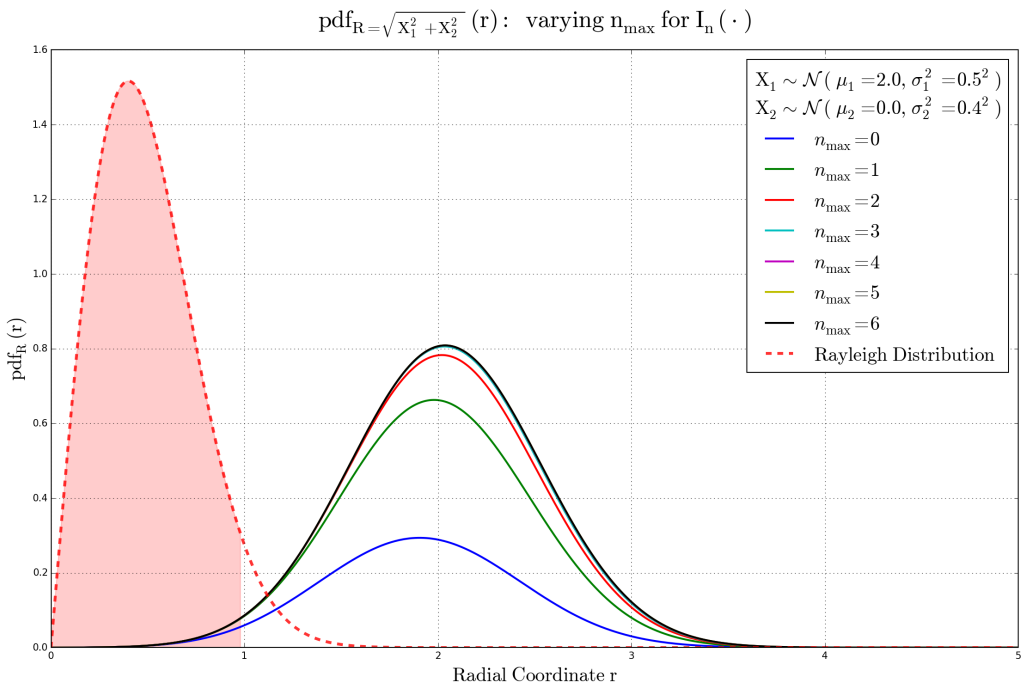

Figure A.1: Demonstration of the relatively quick convergence of the Bessel function sum in equation (A.5). A high level of convergence can be seen after only including up to $n = 3$ in this example. For reference, a Rayleigh distribution is also plotted, corresponding to the case where $\mu_1 = \mu_2 = 0$ and $\sigma_1 = \sigma_2$. The shaded region uncludes 95% of the area under the curve.

$$\gamma_{xy}(f) \equiv \frac{\left|G_{xy}(f)\right|}{\sqrt{G_{xx}(f)G_{yy}(f)}} \tag{A.6}$$

where $G_{xx}(f)$, $G_{xy}(f)$ are the auto- and cross-POWER spectral densities, respectively, both in units of V^2/Hz. Note that equation (A.6) is the square root of equation (B.2).

We now define c to be the fraction of correlated noise power between the two channels, and m_{avgs} the number of averaged samples, in which case the distributions for X_1 and X_2 in coherence units become[2]:

2. Also note that this form assumes that the correlated signal appears only in the real part of the cross-spectrum. If this is not the case in a particular application, it is simple to rotate the coordinates so that

$$
\begin{aligned}
X_1 &\sim \mathcal{N}\left(c,\ \frac{1+2c+2c^2}{2m_{\text{avgs}}}\right) \\
X_2 &\sim \mathcal{N}\left(0,\ \frac{1+2c}{2m_{\text{avgs}}}\right).
\end{aligned}
\tag{A.7}
$$

Note that the correlated component of the signal c appears in both the real and imaginary quadratures, X_1 and X_2, but in different ways. In the imaginary part of G_{xy} (X_2), c appears only in the variance, whereas in the real part of G_{xy} (X_1), c is also the mean. (A.7) also shows that the standard deviations of X_1 and X_2 scale as $1/\sqrt{m_{\text{avgs}}}$, as expected. Plugging (A.7) into (A.5) gives the general form of the sampling distribution for the magnitude of the coherence spectrum:

$$
\begin{aligned}
f_{\text{Coh}}(r, c, m_{\text{avgs}}) = &\frac{2\ r\ m_{\text{avgs}}}{\sqrt{(1+2c+2c^2)(1+2c)}} \\
&\times \exp\left[-\frac{m_{\text{avgs}}}{2}\left(\frac{r^2+2c^2}{1+2c+2c^2}+\frac{r^2}{1+2c}\right)\right] \\
&\times \sum_{n=0}^{\infty} \varepsilon_n I_n\left(\frac{r^2c^2m_{\text{avgs}}}{(1+2c)(1+2c+2c^2)}\right)\cdot I_{2n}\left(\frac{2rcm_{\text{avgs}}}{1+2c+2c^2}\right)
\end{aligned}
\tag{A.8}
$$

A.3 The Special Case of No Correlation: The Rayleigh Distribution

Setting the correlated fraction $c = 0$ in (A.8) gives a Rayleigh distribution[3]

any correlated component indeed appears only in the real part. That case is the same as a bivariate normal distribution with correlated quadratures. In that case, a transformation (rotation) can be applied so that the new coordinates are uncorrelated.

3. Another way of seeing this is that the Euclidean norm of two i.i.d. zero-mean normal random variables has a Rayleigh distribution. Also note that Equation (A.5) gives a Rayleigh distribution when $\mu_1 = \mu_2 = 0$, and $\sigma_1 = \sigma_2$.

$$f_{\mathrm{Coh}}(r, c = 0, m_{\mathrm{avgs}}) = 2rm_{\mathrm{avgs}}e^{-r^2 m_{\mathrm{avgs}}} \tag{A.9}$$

$$= \mathrm{Rayleigh(r, m_{avgs})} \tag{A.10}$$

A more frequently encountered expression for the Rayleigh distribution is

$$f(r, \sigma) = \frac{r}{\sigma^2} e^{-r^2/2\sigma^2} \tag{A.11}$$

where σ is the scale parameter of the distribution, and for Rayleigh it corresponds to the mode. By making the identification $\sigma^2 = 1/(2m_{\mathrm{avgs}})$ between equations (A.11) and (A.9), we see that when $c = 0$ the coherence sampling distribution tends indefinitely to smaller r with more averaged samples. Similarly, the mean and variance of the Rayleigh distribution after m_{avgs} averaged samples are

$$\begin{aligned} \mu &= \sigma\sqrt{\frac{\pi}{2}} = \sqrt{\frac{\pi}{4m_{\mathrm{avgs}}}} \\ \mathrm{Var} &= \sigma^2 \frac{4-\pi}{2} = \frac{1-\pi/2}{m_{\mathrm{avgs}}} \end{aligned} \tag{A.12}$$

which now gives insight into why the trace of a cross-spectrum measurement on a spectrum analyzer behaves the way it does: when there is no underlying correlated signal between the two channels, the mean and standard deviation of the measurements are BOTH reduced by m_{avgs}, and the cross-spectrum trace drifts further and further down the y-axis (smaller r), with more averaged samples. This behavior is illustrated by the red Rayleigh distribution traces in figure A.2.

A.4 Verification of the Coherence Sampling Distribution with Simulated Data

Simulated coherence data was generated and fits to the histogrammed data were performed using the coherence sampling distribution in Equation (A.8), for cases with and without an underlying correlated signal. Figures A.3, A.4, A.5, and A.6 show the spectra of the simulated data and fits to the histogrammed data, for two distinct sets of data. In each of the two simulated data sets, two Gaussian white noise time series s_i were generated:

$$s_i = n_i + n_c \tag{A.13}$$

where $i \in \{1, 2\}$, n_i is uncorrelated between the two time series, and n_c is the correlated component common to both time series. The two data sets differ by changing the correlated component n_c such that the correlated fraction "c" in the coherence is 0.02 in the first data set (Figures A.3 and A.4), and $c = 0.01$ in the second data set (Figures A.5 and A.6). The Welch method with 50% overlapped data segments was used to compute the FFTs of the time series data, with $m_{\text{avgs}} = 12,799$ data segments averaged.

An important point to make is that the histograms are composed of all the data along the frequency axis in the coherence plots. This is equivalent to generating many different samples in a single frequency bin and histogramming those values, but the advantage here is that it is much quicker computationally. The plots show that the coherence sampling distribution in Equation (A.8) describes the data well.

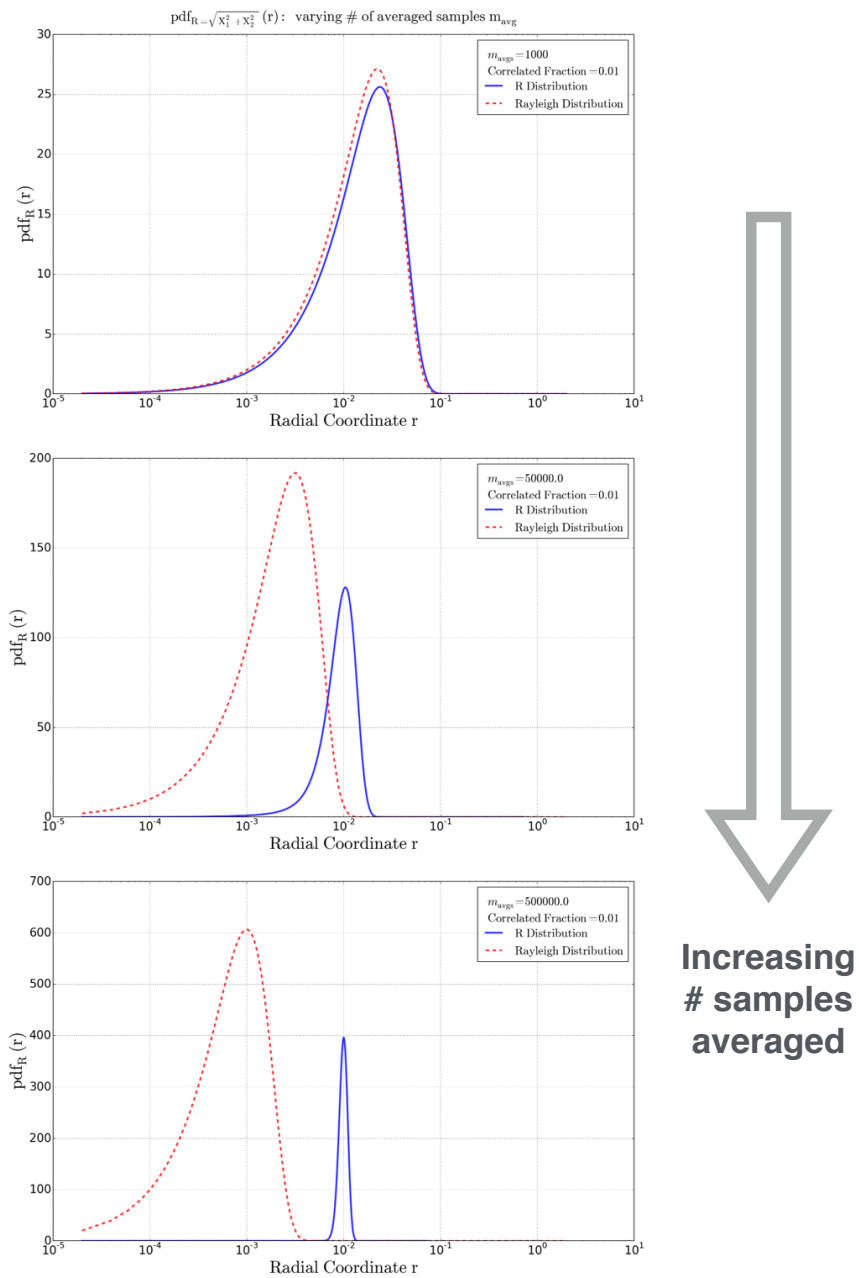

Figure A.2: Resolving correlated components by averaging samples. Each plot shows the coherence sampling distribution in equation (A.8), for the case of no correlation (red) and the case with correlated fraction $c = 0.01$ (blue). The 3 plots have an increasing number of averaged samples m_{avgs}, going from top to bottom. This illustrates the important and useful property of the cross-spectrum to resolve very small signals burried in noise. As the number of samples is increased, eventually it becomes statistically very likely that measured coherence values will be concentrated near the mean value of the underlying correlated signal. This statistical framework describes what occurrs in each and every frequency bin of a cross-spectrum measurement.

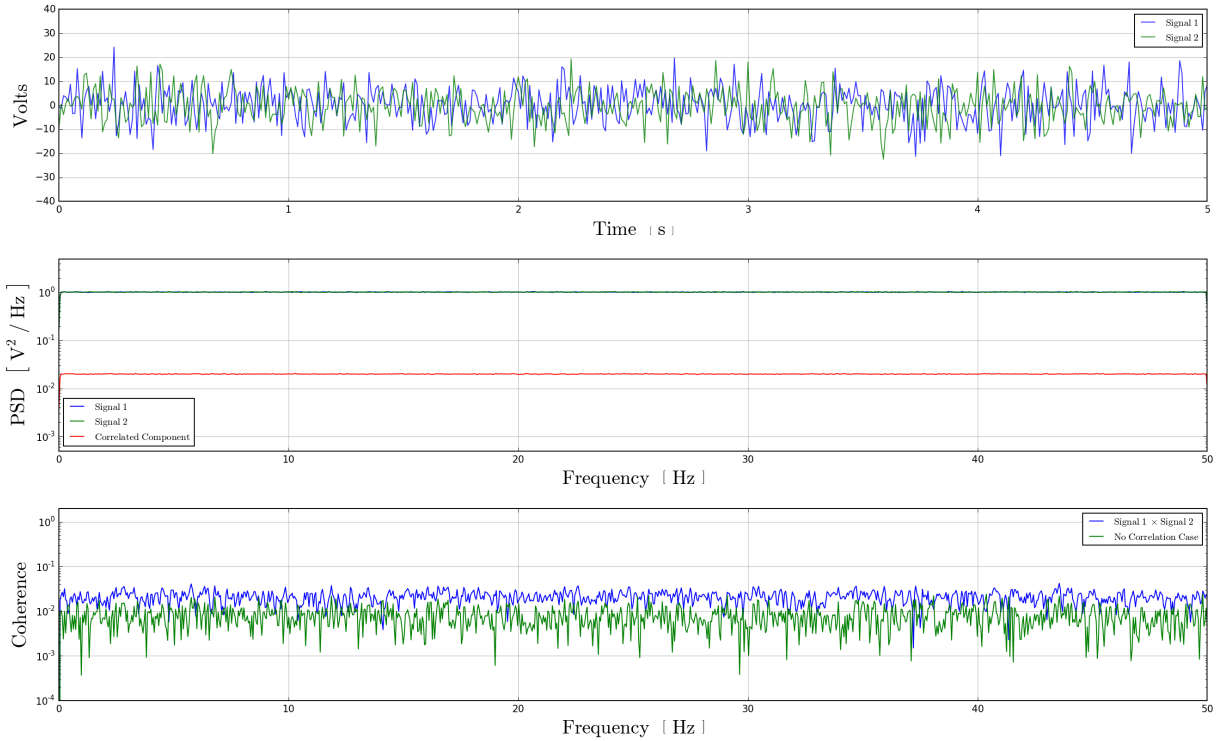

Figure A.3: Simulated data set #1 used to verify the validity of the coherence sampling distribution in Equation (A.8). The correlated fraction is $c = 0.02$. The power spectrum of the correlated component n_c is in red. The case of no correlation ($c = 0$) is shown for reference (green trace in the coherence plot). The analysis results are in Figure A.4.

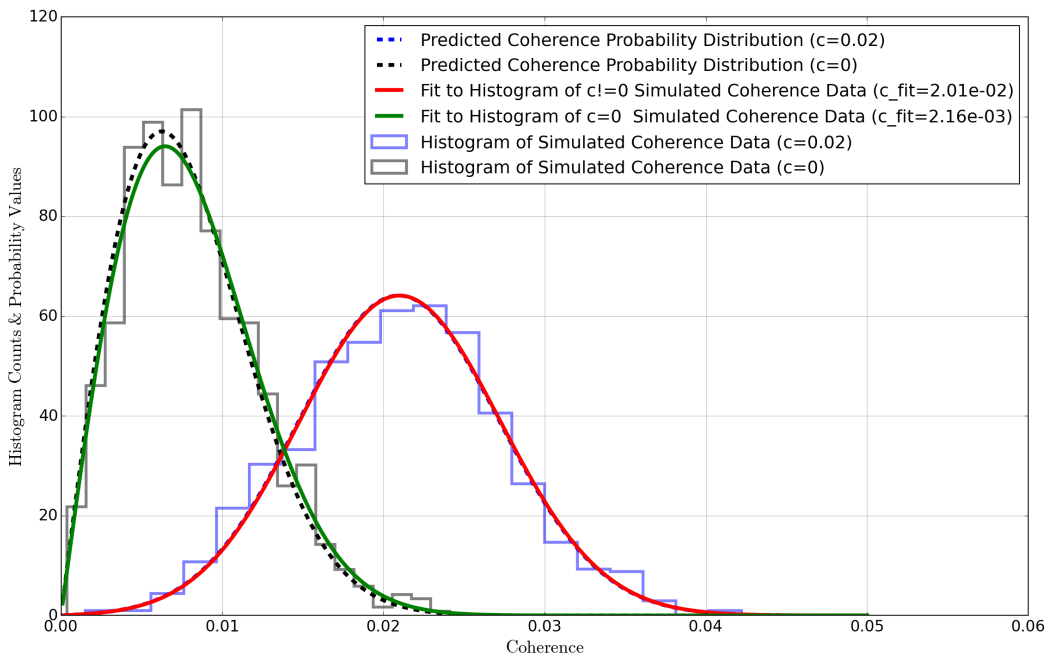

Figure A.4: Fits to simulated data set #1 shown in Figure A.3 using the coherence sampling distribution in Equation (A.8). For the case of correlated fraction $c = 0$, $\chi^2/\text{d.o.f} = 0.943$, and for the case of $c = 0.02$, $\chi^2/\text{d.o.f} = 0.612$.

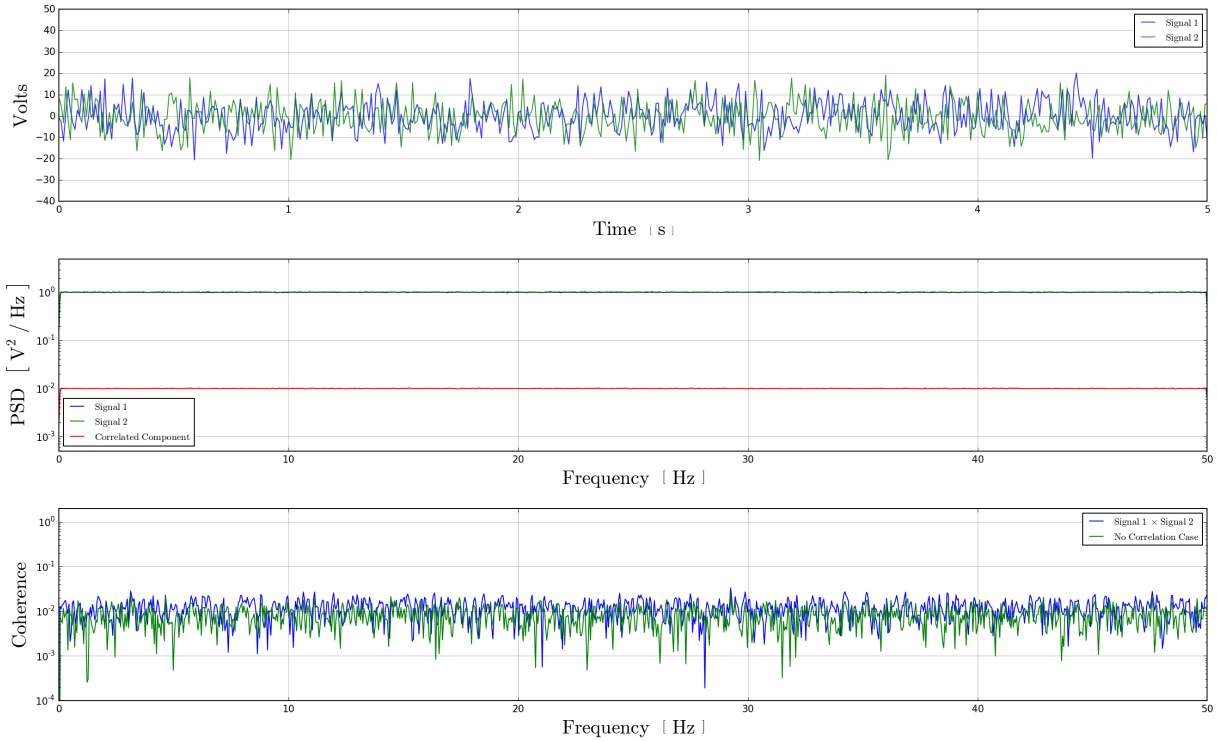

Figure A.5: Simulated data set #2 used to verify the validity of the coherence sampling distribution in Equation (A.8). The correlated fraction is $c = 0.01$. The power spectrum of the correlated component n_c is in red. The case of no correlation ($c = 0$) is shown for reference (green trace in the coherence plot). The analysis results are in Figure A.6.

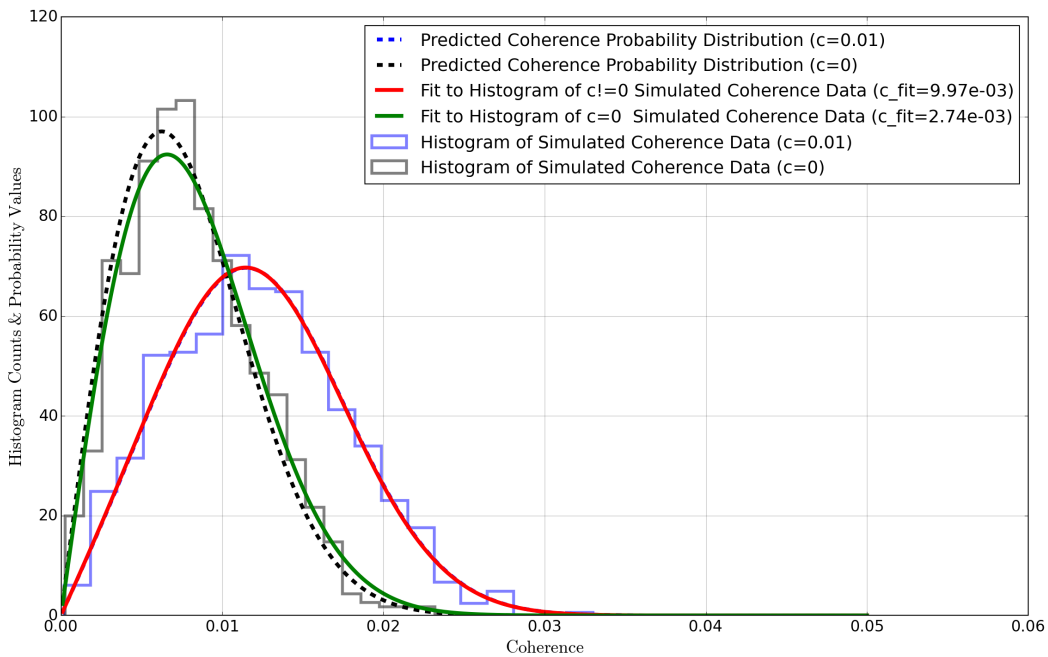

Figure A.6: Fits to simulated data set #2 shown in Figure A.5 using the coherence sampling distribution in Equation (A.8). For the case of correlated fraction $c = 0$, χ^2/d.o.f $= 0.871$, and for the case of $c = 0.01$, χ^2/d.o.f $= 0.655$.

APPENDIX B

STATISTICAL ERRORS IN TRANSFER FUNCTION MEASUREMENTS

B.1 General Formulae

The normalized random error in the transfer function magnitude $\left|H_{xy}(f)\right|$ due to non-perfect coherence and limited number of averages n_{avg} is given by the standard deviation of the estimated magnitude divided by the estimate of the transfer function magnitude itself [6]:

$$\varepsilon_{\text{r}}(f) \equiv \frac{\sigma_{\text{r}}(f)}{\left|H_{xy}(f)\right|} = \frac{\sqrt{1-\gamma_{xy}^2(f)}}{\left|\gamma_{xy}(f)\right|\sqrt{2n_{\text{avg}}}} \tag{B.1}$$

where $\gamma_{xy}^2(f)$ is the Magnitude-Squared Coherence (MSC)

$$\gamma_{xy}^2(f) \equiv \frac{\left|G_{xy}(f)\right|^2}{G_{xx}(f)G_{yy}(f)} \tag{B.2}$$

and $G_{xx}(f)$, $\left|G_{xy}(f)\right|$ are the auto- and cross-POWER spectral densities, respectively, both in units of V^2/Hz. Note that equation B.1 tends to zero as $\gamma_{xy} \to 1$ or n_{avg} becomes large, as one would expect.

B.2 Effects of Overlapping and Windowing

Equation B.1 above was derived in [6] for distinct non-overlapping data segments, averaged together. This section addresses the effects of using the Welch method with 50% overlapped data segments and the use of a Hanning window.

It is shown in [14] that a 50% overlapped Hanning window procedure only modifies $1/\sqrt{N}$

scalings in spectral estimates (for standard deviations and mean values) by 2.8%– **a small effect**. This modification is due to the fact the the overlapped portions of data segments are inherently correlated. This 2.8% correction to the cross-spectrum sampling distribution was verified using simulated data in python (which ultimately uses FFTW to compute Fourier transforms). For example, the standard deviation of the cross-spectrum estimator with no overlap scales as $1/\sqrt{N}$, whereas it scales as $1.028/\sqrt{N}$ when a 50% overlapped Hanning window procedure is used. This same correction factor is true for the mean value of the cross-spectrum when there is no underlying correlated signal (or equivalently when not enough averages have been recorded to resolve an underlying correlated signal)

There is also the question of whether the Welch method introduces bias to the cross-spectrum estimator. [25] finds that, "The introduction of overlap [eg with a Hanning window] does not affect the bias of the estimate."

It should also be noted that the equations for transfer function error as well as coherence which are presented in [6], are only valid in the limit when the coherence is rather large. However, when the coherence is very small, for example in the cases in this work when there is no statistically significant correlation, the equations in [6] are not applicable, and the methods in Appendix A are needed.

APPENDIX C

SPECIFICATIONS AND PARAMETERS

Stored Cavity Power	1.9kW
Injected Laser Power	0.56W
Finesse	$\sim$ 5785
Cavity Pole	$\sim$ 332Hz
Storage Time	239μsec
Contrast Defect	$\sim$ 50ppm
FSR	3.8422 MHz $\pm$ 100 Hz
Inferred PRM to End Mirror Length	39.013 meters $\pm$ 1mm
AS-port Power Attenuation with ND Filter	None

Table C.1: T interferometer operating point parameters during the data runs in this work.

Stored Cavity Power	2.7kW
Injected Laser Power	1.2W
Finesse	$\sim$ 4710
Cavity Pole	$\sim$ 408Hz
Storage Time	195μsec
Contrast Defect	$\sim$ 50ppm
FSR	3.8347 MHz $\pm$ 100 Hz
Inferred PRM to End Mirror Length	39.089 meters $\pm$ 1mm
AS-port Power Attenuation with ND Filter	30% Attenuation

Table C.2: L interferometer operating point parameters during the data runs in this work.

Substrate material	Low inclusion fused silica
Dimensions	50.4 mm diameter, 12.7 mm thickness
Substrate wedge	5 arc minutes
Surface figure	Nominally flat. Greater than 10 km radius of curvature, both surfaces. Astigmatism: $< 8\ nm$ Amplitude of the Zernike coefficient $Z_{2,2}$, as defined in Born and Wolf.
Surface error	$< 0.6\ nm$, best effort for $< 0.3\ nm$ for spatial frequencies $< 1\ mm^{-1}$; $< 0.2\ nm$ frequencies $1 - 50\, mm^{-1}$, over central 45 mm.
Coating deposition method	Ion beam sputtering
Surface 1	Normal incidence partial reflector, $T = 1000 \pm 100\ ppm$. Best effort absorption at 1064 nm $< 1\ ppm$.
Surface 2	Anti-reflection coating, designed for normal incidence. $R < 50\ ppm$ reflection, best effort for $R < 10\ ppm$.

Table C.3: Power recycling mirror specifications

Substrate material	Heraeus 3001, low inclusion fused silica
Dimensions	76.2 mm diameter, 12.7 mm thickness
Substrate wedged	30 arc minutes
Surface figure	Nominally flat. Greater than 10 km radius of curvature, both surfaces. Astigmatism: $< 8\ nm$ Amplitude of the Zernike coefficient $Z_{2,2}$, as defined in Born and Wolf.
Surface error	$< 0.6\ nm$, best effort for $< 0.3\ nm$ for spatial frequencies $< 1\ mm^{-1}$; $< 0.2\ nm$ frequencies $1 - 750 mm^{-1}$, over central 65 mm.
Coating deposition method	Ion beam sputtering
Surface 1	P-polarization beam splitter, 45 degrees angle of incidence on the air side. Transmission $T = 0.5 \pm 0.01$. Absorption at 1064 nm $< 1\ ppm$.
Surface 2	P-polarization anti-reflection coating, designed for 45 degrees angle of incidence on the air side. $R < 50\ ppm$ reflection, best effort for $R < 10\ ppm$. Absorption at 1064 nm $< 1\ ppm$.

Table C.4: Beamsplitter specifications

Substrate material	Fused silica
Dimensions	50.8 mm diameter, 6.35 mm thickness
Side 1 (cavity side)	Radius of curvature: 75 $meters$; Surface Roughness: <1 Å RMS; Transmission: $T = 0.5\ ppm$ (T interferometer), $T = 1.5\ ppm$ (L interferometer)
Side 2 (transmission side)	Surface Flatness: Within 0.25 wave @ 6328 Å; AR coating @1064nm.

Table C.5: End mirror specifications. Transmission values were measured by us.

length	g-factor	R_{PRM}	R_{EM}	z_R	ω_0	ω_{PRM}	ω_{EM}
40 m	0.70	inf	78 m	39.2 m	3.6 mm	3.6 mm	5.2 mm

Table C.6: Nominal power-recycling cavity design configuration.

APPENDIX D

LASER BEAMS AND INTERFEROMETERS: SUPPLEMENTAL

D.1 Gaussian Beams

As a laser beam propagates along a direction z, the transverse size of the beam will grow due to the uncertainty principle, as in Fig. [D.1].

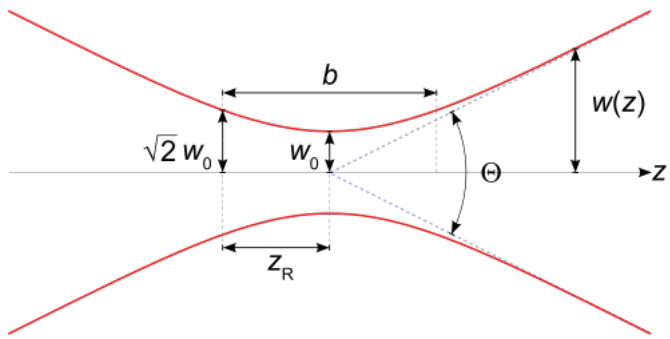

Figure D.1: Gaussian laser beam parameters: z is the distance along the direction of propagation, w is the radius at distance z, w_0 is the smallest radius (the "waist"), z_0 is the waist position, Θ is the divergence angle of the beam, Z_{R} is the "Rayleigh range," the distance away from the beam waist where the transverse beam size increases by a factor of $\sqrt{2}$. Figure from wikipedia/Gaussian_beam.

In Fig. [D.1], the beam is focused to a radius w_0 (the "waist"), and as the transverse size of the beam grows smaller, there is a corresponding increase in uncertainty of the transverse momentum, causing the beam to diverge, asymptotically approaching an angle Θ with respect to the beam axis. When Θ is sufficiently small ("weak focusing condition"), as is the case in our experiment and many laser applications, the transverse spatial profile of the beam is described by solutions to the paraxial wave equation. In rectangular coordinates and one transverse dimension these solutions take the form of what are called Hermite-Gauss TEM_{nm} modes, given by [22],

$$u_n(x,z) = \left(\frac{2}{\pi}\right)^{1/4} \left(\frac{1}{2^n n! w(z)}\right)^{1/2} H_n\left(\frac{\sqrt{2}x}{w(z)}\right) \times \exp\left[i(2n+1)\psi(z) - ikz - i\frac{kx^2}{2R(z)} - \frac{x^2}{w^2(z)}\right] \tag{D.1}$$

where the H_n's are the Hermite polynomials of order n, $R(z) \equiv z - z_0$ is the wavefront radius of curvature at position z, $\psi(x)$ is the "Gouy phase" (explained in section (D.4)), and $k = 2\pi/\lambda$ is the wavenumber. The solutions for two transverse dimensions are given by:

$$u_{nm}(x,y,z) = u_n(x,z) \times u_m(y,z). \tag{D.2}$$

D.2 Pound-Drever-Hall Locking Technique

The Pound-Drever-Hall (PDH) locking technique is a method for maintaining resonance in an optical cavity with the injected laser beam. Very thorough treatments of the PDH method can be found in [8, 12]. This section gives only a brief overview of the concepts necessary for understanding the implementation of PDH in this experiment.

A feedback loop is created between the laser and the resonator cavity (in our case the power-recycling cavity of the interferometer). The length L of the cavity provides a reference distance against which the laser wavelength is compared. The PDH feedback loop continuously monitors and adjusts the laser's output frequency so that a half-integer number of wavelengths fits in a length L, thereby maintaining resonance in the cavity.

The laser beam is first phase modulated in an electro-optic modulator (EOM). The EOM consists of a Mg:$LiNbO_3$ crystal which becomes birefringent in response to an applied voltage ("Pockels effect"). This changes the index of refraction along a single axis, and the polarization of the beam is prepared to be aligned with this axis, so that the beam

acquires a phase shift from the change in refractive index. The EOM voltage is modulated at a specified RF frequency (f_{RF}) corresponding to the combined resonant response of the crystal's capacitance and an external inductor[1]. This places RF sidebands f_s on either side of the central ("carrier") laser frequency f_c, at frequencies $f_s = f_c \pm f_{RF}$.

After the EOM, the beam is then fed through a Faraday isolator (FI), which acts as an optical diode: the FI prevents scattered light traveling up stream toward the laser from damaging the laser, as well as redirecting the light reflected back from the interferometer to photodetectors, for use in the remaining steps of the PDH feedback scheme. In the FI, the beam propagates through a >1 Tesla longitudinal magnetic field and a terbium gallium garnet crystal, which rotates the beam polarization by 45° via the Faraday effect. Reflected components of the beam, returning in the opposite direction through the FI, receive an additional 45° of rotation, resulting in a polarization angle of 90° w.r.t. the initial beam. These 90° rotated beams are then diverted away from the original beam axis with a polarizing beam splitter, and focused onto an RF photodiode. As discussed later, the signal in the photodiode from the returning beam is used to produce the error signal for the PDH feedback loop.

After passing through the FI, the beam (now composed of carrier and sidebands) is directed into the resonator cavity. Focusing lenses prior to the cavity are arranged so that the beam waist is placed at the cavity input mirror, with the appropriate size as determined by the cavity properties (c.f. section 3.3.2).

The electric field of the beam after being phase modulated in the EOM has the form:

1. The second EOM used in this experiment (which is not used for PDH, c.f. figures 3.2 and 3.3) does not have this inductor, and so can be operated in broadband for diagnostic and calibration purposes, as described in the main text.

$$
\begin{aligned}
E_{\text{inc}} &= E_0 e^{i(\omega t + \beta \sin \Omega t)} \\
&\approx E_0 e^{i\omega t} \left(1 + i\beta \sin \Omega t\right) \\
&= E_0 \left(e^{i\omega t} + \frac{\beta}{2} e^{i(\omega+\Omega)t} - \frac{\beta}{2} e^{i(\omega-\Omega)t} \right)
\end{aligned} \tag{D.3}
$$

where the "modulation depth" β is typically very small, allowing for the approximation in the second line. Here, the carrier frequency is $f_c = \omega/2\pi$, and the sideband frequencies are $f_s = (\omega \pm \Omega)/2\pi = f_c \pm f_{\text{RF}}$. If we were to instead apply amplitude modulation to the beam, the electric field would have the form:

$$
\begin{aligned}
E_{\text{inc}} &= E_0 e^{i\omega t} \left(1 + \beta \sin \Omega t\right) \\
&= E_0 \left(e^{i\omega t} + i\frac{\beta}{2} e^{i(\omega+\Omega)t} - i\frac{\beta}{2} e^{i(\omega-\Omega)t} \right)
\end{aligned} \tag{D.4}
$$

Equations (D.3) and (D.4) show that a pure phase modulation can be turned into a pure amplitude modulation by changing the relative phase between carrier and sidebands by $\pi/2$. In the PDH scheme, the sidebands lie outside of the cavity resonance bandwidth when the carrier is close to resonance. The sidebands are therefore reflected off the cavity input mirror (the power-recycling mirror, PRM, in this case) back through the FI toward the photodetector ("REFL" port in figures 3.2 and 3.3). The carrier, being within the cavity bandwidth, enters the cavity and bounces around between the mirrors. Some of the carrier light leaks out the far end mirrors, some is dissipated within the cavity by scattering off of impurities on the mirrors (e.g. dust specs), and some is transmitted back through the PRM and recombines with the modulation sidebands. If the carrier satisfies the resonance condition of the cavity, it will have acquired a net phase that is an integer multiple of π when it exits the cavity through the PRM and recombines with the sidebands. From Eq. (D.3),

the recombined beam will still be equivalent to a phase modulated beam. However, if the carrier is not on resonance, then when it leaves the cavity it will have acquired a net phase different from $n\pi$. When it recombines with the sidebands, there will then be an amplitude modulation as well. The photodetector is a "square-law detector", meaning it measures the square of the electric field EE^*, and as such it is impervious to phase modulations. However it is sensitive to amplitude modulations, and this is how the PDH loop is able to sense when the laser is off resonance from the cavity.

There are two equivalent ways to view the PDH locking technique. One can either treat the cavity length L as being fixed and the laser wavelength λ as changing, or the reverse (of course in reality both are occurring simultaneously). When the laser frequency is very close to resonance, the power in the beam reflected back from the cavity can be approximated in the following simple form that is linear in the cavity length fluctuations δL [8]:

$$P_{\text{ref}} \approx 2P_s - 16\sqrt{P_c P_s}\frac{\mathcal{F}}{\lambda}\delta L \sin \Omega t. \tag{D.5}$$

where P_s is the power in the sidebands, P_c the carrier power, and $\mathcal{F}$ is the cavity finesse, described in section (D.3). The reflected power is detected by the RF photodetector which has a transimpedance amplifier that converts the induced photocurrent into a voltage. The voltage signal is then multiplied with the original modulation signal from the RF signal generator in a mixer (c.f. "mixer" in figures 3.2 and 3.3). The mixer picks out the component proportional to $\sin \Omega t$, producing the error signal ϵ:

$$\epsilon \equiv -16\sqrt{P_c P_s}\frac{\mathcal{F}}{\lambda}\delta L \tag{D.6}$$

The error signal in equation D.6 has the right properties necessary to create a negative

feedback loop; it is negative in magnitude when the carrier is on the high frequency side of resonance, positive when the carrier is on the low frequency side of resonance, and zero on resonance. To see this, note that an increase in L means that to maintain resonance, the laser wavelength must increase, i.e. the frequency must decrease.

The error signal is then split into high and low frequencies and sent to the laser for controlling the output frequency. The laser has two input controls for adjusting the output frequency. The "fast" or "PZT" channel controls a piezo actuator that is coupled to the lasing crystal. The piezo applies a pressure to the lasing crystal, changing it's length, thereby changing the wavelength of the light. The piezo has resonances beginning around 100kHz, so the error signal must be attenuated below this– in practice we actuate up to 20kHz or so. The "slow" channel controls the temperature of the lasing crystal, with the same effects as the piezo, but on a much slower time scale (sub Hz) and with much larger gain (small temperature changes produce very large frequency changes). In practice, we found it unnecessary to actuate the frequency using the thermal controls, because the relative drift between the cavity and laser stays within the dynamic range of all the feedback components for sufficiently long periods of time, and so the relatively small gain of the PZT channel is adequate [2].

D.3 Finesse, Cavity Pole, & Free Spectral Range

As laser light reflects back and forth between the cavity end mirrors and PRM, the circulating intensity experiences resonant peaks when the round trip phase advance of the electric field ($\omega t = \omega 2L/c$) is an integer multiple of 2π, and hence undergoes constructive interference. The resonant frequencies $f_0 = \omega/2\pi$ of the cavity therefore satisfy the condition:

2. For example, the natural drift of the laser is $\sim$ 1MHz/minute, while the gain of the PZT channel is $\sim$ 1.5MHz/V with an actuation range of $\pm 100V$. Similar arguments and measurements show that other components in the PDH loop have enough dynamic range to operate without clipping or saturating for long enough periods of time as to not be a concern.

$$f_0 = n\frac{c}{2L} \quad \text{(resonance condition)} \tag{D.7}$$

where n is an integer. The quantity $c/2L$ is called the Free Spectral Range (FSR), or axial mode spacing, and represents the frequency spacing between cavity resonances. It should be noted that the FSR represents the frequency spacing between resonances for the transverse Gaussian-shaped mode (i.e. TEM_{00}). As discussed in section (D.4) below, each higher order TEM_{nm} mode experiences an additional phase advance as it propagates along the beam path, and is subject to the modified resonance condition in Eq (D.12).

When the laser frequency satisfies the resonance conditions of the cavity, reflections back toward the error signal photodiode in the PDH loop are minimized, and the cavity acts as an absorber. When monitoring the output voltage from the PDH error signal photodiode (c.f. section D.2 and figures 3.2 and 3.3) as the laser frequency goes through resonance, steep dips in the signal, i.e. absorption lines, are clearly visible (see pink trace in figure 2.4). The full width at half maximum (FWHM) of these resonance peaks is the cavity bandwidth, and along with the FSR it determines a quantity called the cavity finesse ($\mathcal{F}$), which is analogous to the quality factor Q of a mechanical resonator.

The Finesse of an optical cavity is defined as the ratio of the FSR to the cavity bandwidth:

$$\mathcal{F} \equiv \frac{\text{FSR}}{\text{FWHM}} \quad \text{(finesse)} \tag{D.8}$$

It is a measure of the power losses of the beam within the cavity. In the ideal limit that the only power loss in the cavity is due to transmission through the end mirrors, the Finesse takes the form [22]:

$$\mathcal{F} = \frac{\pi\sqrt{r_1 r_2}}{1 - r_1 r_2} \tag{D.9}$$

where r_1 and r_2 are the reflectivities of the cavity end mirrors. The terminology "cavity pole" is often used as well, which is defined as:

$$f_{\text{pole}} = \text{FWHM}/2 \ \ \text{(cavity pole)} \tag{D.10}$$

D.4 Gouy Phase and Higher Order Modes

For a general beam composed of the fundamental gaussian TEM_{00} mode and higher order TEM_{nm} modes, the total phase advance $\phi(L)$ accumulated across the cavity length L is given by [22],

$$\phi(L) = \frac{\omega L}{c} - (n + m + 1)\cos^{-1} \pm\sqrt{g_1 g_2} \tag{D.11}$$

where $g_i \equiv 1 - L/R_i$ are called the cavity g-parameters, and R_i are the radii of curvature of the cavity mirrors. The first term is just the phase shift of a wave traveling at speed c over a distance L, and the second term is the Gouy phase advance. The general condition for cavity resonance is then given by:

$$\frac{\omega L}{c} - (1 + n + m)\cos^{-1} \pm\sqrt{g_1 g_2} = q\pi, \tag{D.12}$$

for some integer q. From (D.12) we see that the Gouy phase advance breaks the frequency degeneracy for resonating Hermite-Gauss modes, forcing the resonant frequencies of higher order TEM_{nm} modes to be offset from each other.

The presence of resonating higher order modes can add excess noise to the signal readout of the interferometers, and in some cases they can cause instabilities in the feedback loops. It is therefore desirable to minimize the occurrence of Gouy phase resonances from higher order modes. This can be achieved by choosing the cavity parameters in equation D.12 such that only modes with very high values of n and m will satisfy condition (D.12).

Higher order modes (HOM) can be generated in many different ways. Particular examples in this experiment are given in section 3.3.1, with HOM resonances clearly visible in the auto-spectrum traces of the antisymmetric port signal photodetectors in Figures 3.7, 3.8, 3.9, 3.10.

D.5 Useful Optical Equations

$H_{\text{ref}}(w) \equiv \frac{E_{ref}}{E_{inc}} = \frac{r_1 - r_2(R_1+T_1)e^{-i\frac{w}{\text{FSR}}}}{1-r_1 r_2 e^{-i\frac{w}{\text{FSR}}}}$	Reflected electric field transfer function
$H_{\text{circ}}(w) \equiv \frac{E_{circ}}{E_{inc}} = \frac{-it_1}{1-r_1 r_2 e^{-i\frac{w}{\text{FSR}}}}$	Circulating electric field transfer function
$H_{\text{trans}}(w) \equiv \frac{E_{trans}}{E_{inc}} = \frac{-t_1 t_2 e^{-i\frac{w}{2\text{FSR}}}}{1-r_1 r_2 e^{-i\frac{w}{\text{FSR}}}}$	Transmitted electric field transfer function
where $\phi \equiv kL = \frac{2\pi}{\lambda}L = \frac{w}{c}L = \frac{w}{2\text{FSR}}$	
and $L =$ cavity length	
$\mathcal{F} \equiv \frac{\text{FSR}}{\text{FWHM}} = \frac{\pi\sqrt{r_1 r_2}}{1-r_1 r_2}$	Finesse
$f_{\text{pole}} \equiv \text{HWHM} = \frac{\text{FSR}}{2\mathcal{F}}$	Cavity Pole
$G_{\text{cav}} \equiv \left(\frac{E_{circ}}{E_{inc}}\right)^2 = \left(\frac{t_1}{1-r_1 r_2}\right)^2$	(Power) Cavity Gain on resonance

Table D.1: A few useful Fabry-Perot cavity relations.

APPENDIX E

GLOSSARY OF SYMBOLS

E	Electric field
r	Amplitude reflectivity of an optic,
	and radial coordinate in coherence sampling distribution
t	Amplitude transmissivity of an optic, and time
w_0	Beam waist size
w	Beam radius, and angular frequency
z_0	Beam waist position
z	Position along beam propagation axis
FSR	Free Spectral Range
$\mathcal{F}$	Cavity Finesse
f_R	Sampling distribution for the magnitude of the cross-spectrum R
f_{Coh}	Sampling distribution for the magnitude of the coherence spectrum
$G(f)$	Complex-valued loop gain. $G(f) = \lvert G(f)\rvert e^{i\theta(f)}$, with phase angle $\theta(f)$
$G_{ii}(f)$	Auto-spectral density function (one-sided)
$G_{ij}(f)$	Cross-spectral density function (one-sided)
$\gamma^2_{ij}(f)$	Magnitude-Squared Coherence (MSC)
h	Gravitational wave strain amplitude
HOM	Higher Order Mode
	(Hermite-Guass TEM_{nm} laser modes with n,m not both 0)
PRM	Power recycling mirror
TF	Transfer Function

See also Table 5.1 for notation used in the calibration in Chapter 5.

REFERENCES

[1] Valentine Aalo, George Efthymoglou, and Chirasil Chayawan. On the envelope and phase distributions for correlated gaussian quadratures. *IEEE Communications Letters*, 11(12):985–987, December 2007.

[2] F Acernese and Et Al. The Virgo status. *Class Quantum Grav*, 23:S635—-S642, 2006.

[3] Tomotada Akutsu, Seiji Kawamura, Atsushi Nishizawa, Koji Arai, Kazuhiro Yamamoto, Daisuke Tatsumi, Shigeo Nagano, Erina Nishida, Takeshi Chiba, Ryuichi Takahashi, Naoshi Sugiyama, Mitsuhiro Fukushima, Toshitaka Yamazaki, and Masa-Katsu Fujimoto. Search for a Stochastic Background of 100-MHz Gravitational Waves with Laser Interferometers. *Physical Review Letters*, 101(10):101101, September 2008.

[4] Asimina Arvanitaki and Andrew Geraci. Detecting High-Frequency Gravitational Waves with Optically Levitated Sensors. *Physical Review Letters*, 110(7):071105, February 2013.

[5] John Bechhoefer. Feedback for physicists: A tutorial essay on control. *Reviews of Modern Physics*, 77(July):783–836, 2005.

[6] Julius Bendat and Allan Piersol. *Random Data: Analysis and Measurement Procedures*. 4th edition, 2010.

[7] Ph. Bernard, G. Gemme, R. Parodi, and E. Picasso. A detector of small harmonic displacements based on two coupled microwave cavities. *Review of Scientific Instruments*, 72:2428–2437, March 2001.

[8] Eric D. Black. An introduction to PoundDreverHall laser frequency stabilization, 2001.

[9] Sean Carroll. *Spacetime and Geometry: An Introduction to General Relativity*. Addison Wesley, 2004.

[10] Aaron Chou, Craig Hogan Spokesperson, Erik Ramberg, Jason Ste, Chris Stoughton, Ray Tomlin, William Wester, Sam Waldman, Rainer Weiss, Stephan Meyer, H Richard Gustafson, and Stanley Whitcomb. The Fermilab Holometer: A program to measure Planck scale indeterminacy - Experiment Proposal. 2009.

[11] Glen Cowan. *Statistical Data Analysis*. Clarendon Press, 1998.

[12] R. W P Drever, J. L. Hall, F. V. Kowalski, J. Hough, G. M. Ford, a. J. Munley, and H. Ward. Laser phase and frequency stabilization using an optical resonator. *Applied Physics B Photophysics and Laser Chemistry*, 31:97–105, 1983.

[13] Maxim Goryachev and Michael E. Tobar. Gravitational Wave Detection with High Frequency Phonon Trapping Acoustic Cavities. pages 1–9, October 2014.

[14] F.J. Harris. On the use of windows for harmonic analysis with the discrete Fourier transform. *Proceedings of the IEEE*, 66(1):51–83, 1978.

[15] Craig J Hogan. Interferometers as probes of Planckian quantum geometry. *Physical Review D - Particles, Fields, Gravitation and Cosmology*, 85:23, February 2012.

[16] Patrick Kwee and Benno Willke. Automatic laser beam characterization of monolithic Nd:YAG nonplanar ring lasers. *Applied optics*, 47:6022–6032, 2008.

[17] C. Misner, K. Thorne, and J. Wheeler. *Gravitation*. Macmillan, 1973.

[18] C J Moore, R H Cole, and C P L Berry. Gravitational-wave sensitivity curves. *Classical and Quantum Gravity*, 32(1):015014, 2015.

[19] K A Olive and Others. Review of Particle Physics. *Chin.Phys.*, C38:90001, 2014.

[20] F. Pegoraro, L.a. Radicati, Ph. Bernard, and E. Picasso. Electromagnetic detector for gravitational waves, 1978.

[21] Peter Saulson. *Fundamentals of Interferometric Gravitational Wave Detectors*. World Scientific, 1994.

[22] A. E. Siegman. *Lasers*. University Science Books, 1986.

[23] The LIGO Scientific Collaboration 2009. LIGO: the Laser Interferometer Gravitational-Wave Observatory. *Rep. Prog. Phys.*, 076901, 2009.

[24] Robert Wald. *General Relativity*. University of Chicago Press, 1984.

[25] W. D. Widanage, J.L. Douce, and K.R. Godfrey. Effects of Overlapping and Windowing on the Estimates of Frequency Response Functions of Linear Systems with Random Input Signals. In *2007 IEEE Instrumentation & Measurement Technology Conference IMTC 2007*, pages 1–6. IEEE, May 2007.